(NASA-CR-169666) COMPUTER SIMULATION OF SURFACE AND FILM PROCESSES Semiannual Status Report, 1 May - 31 Oct. 1982 (Stanford Univ.) 102 p HC A06/MF A01 CSCL 09B G3/61

N83-14971

Unclas 02261

SEMIANNUAL STATUS REPORT

for

COMPUTER SIMULATION OF SURFACE AND FILM PROCESSES

May 1, 1982 - October 31, 1982

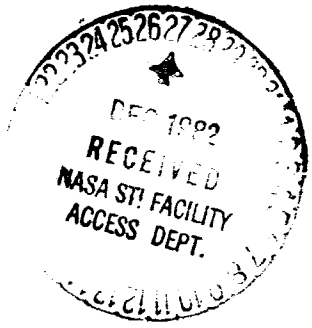

Cooperative Agreement No.: NCC 2-125

Period of Award: May 1, 1982 - April 30, 1983

Principal Investigator: Professor W. A. Tiller

Senior Investigator: Dr. M. T. Halicioglu

SU-DMS-83-R-1

Stanford/NASA Ames Joint Institute for Surface and Microstructure Research
Department of Materials Science and Engineering
Stanford University, Stanford, CA 94305

COMPUTER SIMULATION OF SURFACE AND FILM PROCESSES

This program has three main parts:

I. Film Formation and the Morphology of Solid Surfaces and Overlayers.

II. Diffusion of Atoms and Microclusters at Substrate Surfaces.

III. Crack Formation and Propagation Phenomena.

All three investigations are based on computer simulation techniques and the objective is to analyze various processes at atomic levels. The progress made during the last six-month period is presented in this report in three different self-contained chapters.

I. FILM FORMATION AND THE MORPHOLOGY OF SOLID SURFACES AND OVERLAYERS

Objective

The objective of this study is the analysis of surfaces and interface properties at microscopic levels. Two types of simulations have been initiated. (a) parametric investigations and (b) a specific case study. The parametric investigations are made for the purpose of analyzing the general behavior of different systems, comparatively, and to classify the important factors which influence both the structure and the energy-related properties of surfaces and interfaces for these systems.

In this study, a molecular dynamics technique based upon Lennard-Jones type pair interactions is used to investigate time-dependent as well as equilibrium properties. The specific case study deals with systems containing Si and O atoms. In this case a more involved potential energy function (PEF) is employed and the system is simulated via a Monte-Carlo procedure. This furnishes the equilibrium properties of the system at its interfaces and surfaces as well as in the bulk.

A. Parametric Investigation

The following progress has been made during this period:

1. A utility package has been prepared for the evaluation of the MOLDY results. This package consists of several programs and uses the data generated by the molecular dynamics program as an input. It has the following capabilities:

   (i) The radial distribution function, virial, density and energy profiles across the interface can be obtained.

   (ii) It can perform time series analysis: correlation functions (density or velocity auto-correlation) and vibrational frequency spectra

of the particles in motion can be calculated. The program has the flexibility of calculating components of a vibrational frequency spectrum for any number of particles and for any desired subsection of the system. It uses a fast Fourier transformation routine and accepts velocity components of the particles generated by the molecular dynamics. The program requires a relatively small amount of CPU time.

2. A graphic software package has also been developed which provides visual inspection of the whole system as well as of any local region of the system. It can be employed for generating a single frame for any desired time step or it can be used to produce a movie for the real time simulation of individual atomic motions.

   The package also includes a program which can be used to generate trajectories of individual particles for quick inspection.

At the moment a test case is under investigation for the analysis. The system consists of two different atomic species to represent an interface between a substrate and an adlayer. Figure 1 demonstrates the system schematically. It contains 927 particles (with 381 particles (Cu) in the adlayer and the rest, 546 particles (Ag), in the substrate). The reduced parameters used in the molecular dynamics procedure (representative of a Cu/Ag system) were:

$$\varepsilon^*_{ad} = 1.1872 \qquad \sigma^*_{ad} = 0.8846$$

$$\varepsilon^*_{sub} = 1.0 \qquad \sigma^*_{sub} = 1.0$$

Time step, $dt^* = 0.01$

Temperature, $T^* = 0.3$

No periodic boundary condition has been imposed because of the binary nature of the system. The particles (Ag) within the three bottom layers of the substrate were held fixed during the run; but they were permitted to interact with the rest of the system contributing to the total potential energy. The test system was run up to 1000 time steps. The first 200 steps were used for the temperature rescaling process, and the rest employed in the analysis. All the thermodynamic quantities were calculated considering only the "core" region of the hexagonal slab (to eliminate the surface effect). The core included all the atoms within a radius of $2.8\,\sigma^{*}_{sub}$ from the center. Figure 2 demonstrates mobile atoms during the equilibration; and Fig. 3 is a close-up of the same region around the interface. Figure 4 shows trajectories of the atoms within the top layer of the substrate, and Fig. 5 is a trajectory plot for the bottom layer of the absorbate (which is facing the layer in Fig. 4).

Figure 6 demonstrates the potential energy profile across the interface which is located between the third and the fourth peaks. The difference between these peaks indicates the stronger binding among the adatoms. Figure 7 is the virial profile similar to Fig. 6. Because of its differential character, the virial reflects the mismatch of the sites at the interface. The difference in atomic sizes causes the adlayer side to dilate while the substrate side contracts. The dilation is exhibited by a negative virial while the contraction by an added positive contribution as expected.

B. Simulation of Systems with Si and O Atoms

For a more quantitative representation of systems involving Si and O atoms we considered a general type of potential energy function which is based on two-body and three-body interactions. The most serious difficulty involved

in simulation studies of such systems is, in general, due to the potential energy function and its ability to represent the system adequately. The analytical form of the potential energy function and the evaluation of its parameters that are being used are described briefly.

For a system of N particles the total potential energy Φ may be expressed as:

$$\phi = \frac{1}{2!} \sum_{i \neq j}^{N} \sum^{N} u(\vec{r}_i, \vec{r}_j) + \frac{1}{3!} \sum_{i \neq j \neq k}^{N} \sum^{N} \sum^{N} u(\vec{r}_i, \vec{r}_j, \vec{r}_k) + \ldots$$

$$\ldots + \frac{1}{n!} \sum_{i \neq j \neq \ldots \neq n}^{N} \sum^{N} \ldots \sum^{N} u(\vec{r}_i, \vec{r}_j, \ldots, \vec{r}_n) + \ldots \qquad (1)$$

where, $u(\vec{r}_i, \vec{r}_j)$, $u(\vec{r}_i, \vec{r}_j, \vec{r}_k)$ ..., $u(\vec{r}_i, \vec{r}_j, \ldots, \vec{r}_n)$ are the two-three and n-body potentials respectively; $\vec{r}_j$ denotes the position of the j^{th} particle. Clearly, the most important term in this expansion is the first term involving the two-body potential. Therefore, in the majority of the atomistic calculations to date only pairwise additive potentials have been used. In this investigation not only two-body but also three-body interactions are taken into consideration. Because this expression (Eq. 1) will be used in lengthy machine computations, the functional form of $u(\vec{r}_i, \vec{r}_j)$ and $u(\vec{r}_i, \vec{r}_j, \vec{r}_k)$ must be very simple. The two-body part, therefore, is represented by a Mie-type potential.

$$u(r_{ij}) = \left[\frac{\varepsilon}{m-n}\; n\left(\frac{r^o}{r_{ij}}\right)^m - m\left(\frac{r^o}{r_{ij}}\right)^n\right] \qquad (2)$$

where $r_{ij} = |\vec{r}_i - \vec{r}_j|$, while r^o denotes the equilibrium separation and ε is the energy at $r_{ij} = r^o$. The exponents m and n account for the repulsive and attractive terms, respectively. For the intermediate to large separations the three-body interactions may be expressed as:

$$u(\vec{r}_i,\vec{r}_j,\vec{r}_k) = \sum_{\ell} Z_\ell \cdot G_\ell(\vec{r}_i,\vec{r}_j,\vec{r}_k) \qquad (3)$$

where, the summation includes all triple multiple interactions resulting from the expansion of the third-order interaction energy for three atoms. Each term in the summation is expressed as the product of a geometrical factor $G(\vec{r}_i,\vec{r}_j,\vec{r}_k)$ which depends on the relative positions of the three atomic nuclei and an interaction constant which depends only on the atomic species involved in the interaction. Here, we employ only the triple-dipole interaction which has been shown to be the dominant contribution

$$u(\vec{r}_i,\vec{r}_j,\vec{r}_k) = Z_1 \cdot G_1(\vec{r}_i,\vec{r}_j,\vec{r}_k) \qquad (4)$$

with

$$G(\vec{r}_i,\vec{r}_j,\vec{r}_k) = \frac{1 + 3\mathrm{Cos}\,\theta_i \mathrm{Cos}\,\theta_j \mathrm{Cos}\,\theta_k}{(r_{in} \cdot r_{ik} \cdot r_{jk})^3} \qquad (5)$$

where θ_i, θ_j, θ_k and r_{ij}, r_{ik}, r_{jk} represent the angles and the sides of the triangle formed by the three particles i, j and k.

Now, combining equations 1 through 5 and neglecting the four-body and

higher terms one obtains:

$$\Phi = \psi_2 + \psi_3 \tag{6a}$$

with

$$\psi_2 = \frac{1}{2} \sum_{\substack{i \\ i \neq j}}^{N} \sum_{j}^{N} \frac{\varepsilon}{m-n} \; n \left(\frac{r^o}{r_{ij}}\right)^m - m \left(\frac{r^o}{r_{ij}}\right)^n \tag{6b}$$

and

$$\psi_3 = \frac{1}{6} \sum_{\substack{i \\ i \neq j \neq k}}^{N} \sum_{j}^{N} \sum_{k}^{N} \frac{(1 + 3\cos\theta_i \cos\theta_j \cos\theta_k)}{(r_{ij} \cdot r_{ik} \cdot r_{jk})^3} \tag{6c}$$

In this general form the total potential energy Φ is a function of the parameters, ε, r^o, m, n and Z_1, and the atomic configuration of the system. The parameters are assumed to be independent of the atomic positions and the geometry of the system. They depend only on the atomic properties of species involved.

For a binary system of types 1 and 2 [1 ≡ silicon, and 2 ≡ oxygen] with the corresponding number of particles N_1 and N_2, Eq. (6a) may be rewritten as:

$$\Phi = \psi_2 + \psi_3 \tag{7}$$

with

$$\psi_2 = \sum_{\alpha}^{2} \sum_{\beta}^{2} \frac{N_\alpha \varepsilon_{\alpha\beta}}{2(m-n)} \left[n \, a_{\alpha\beta}^{(m)} R_{\alpha\beta}^{m} - m a_{\alpha\beta}^{(n)} R_{\alpha\beta}^{n} \right] \tag{8}$$

and

$$\Psi_3 = \sum_{\substack{\alpha \\ \beta < \gamma}}^{2} \sum_{\beta}^{2} \sum_{\gamma}^{2} \frac{N_\alpha Z_{\alpha\beta\gamma}}{3d^9} \cdot T_{\alpha\beta\gamma} \qquad \begin{matrix} \alpha = 1,2 \\ \beta = 1,2 \\ \gamma = 1,2 \end{matrix} \qquad (9)$$

where

$$R_{\alpha\beta} = \frac{r^o_{\alpha\beta}}{d} \qquad (10)$$

$$a^{(m)}_{\alpha\beta} = \sum_{j}^{N_\beta} \left(\frac{d}{r_{\alpha j}}\right)^m \qquad r_{\alpha j} \neq 0 \qquad (11)$$

$$a^{(n)}_{\alpha\beta} = \sum_{j}^{N_\beta} \left(\frac{d}{r_{\alpha j}}\right)^n \qquad r_{\alpha j} \neq 0 \qquad (12)$$

and

$$T_{\alpha\beta\gamma} = \sum_{\substack{j \\ j < k}}^{N_\beta} \sum_{k}^{N_\gamma} G(r_{\alpha j}, r_{\alpha k}, r_{jk}) \qquad \begin{matrix} r_{\alpha i} \neq 0 \\ r_{\alpha j} \neq 0 \end{matrix} \qquad (13)$$

$r^o_{\alpha\beta}$ represents the equilibrium separation between the two species α and β for the two-body part ($r^o_{\alpha\beta} \equiv r^o_{\beta\alpha}$); "d" is a critical distance parameter which is used as a normalizing factor. Φ is independent of the value of d. $r_{\alpha j} = |\vec{r}_\alpha - \vec{r}_j|$, where $\vec{r}_\alpha$ denotes the position of an atom of type α taken as the central particle for the summation. The total number of particles in the system is given by $N_{Tot} = N_1 + N_2$.

The parameters (such as $\epsilon_{\alpha\beta}, r^o_{\alpha\beta}, a_{\alpha\beta}, Z_{\alpha\beta\gamma}$ and $\Gamma_{\alpha\beta\gamma}$) were obtained using isolated microclusters and the bulk property data for pure Si and O, as well as data for various SiO_2 crystalline phases. Furthermore, for the evaluation of the parameters, a stability criterion was considered that is given as:

$$\left(\frac{\partial \Phi}{\partial V}\right)_{T_o} = 0 \; . \qquad (14)$$

For a start, exponents m and n in the two-body term were assumed to be equal to 12 and 6, respectively. Values for $a_{\alpha\beta}^{(m)}$, $a_{\alpha\beta}^{(n)}$ and $T_{\alpha\beta\gamma}$ are computed directly from the crystallographic data for the corresponding SiO_2 phases (see Table 1). The parameters ($\epsilon_{\alpha\beta}$, $r_{\alpha\beta}^{o}$, and $Z_{\alpha\beta\gamma}$) for silicon were calculated from experimental bulk and small cluster data, while for oxygen they were obtained from thermodynamic data reported for the O_2 molecules as:

$$\epsilon_{11} = 37745\ (^0K)$$

$$r_{11}^{o} = 2.3516\ (\text{Å})$$

$$Z_{111} = 6.136 \times 10^6 (^0K \cdot \text{Å}^9)$$

$$\epsilon_{22} = 59943\ (^0K)$$

$$r_{22}^{o} = 1.2078\ (\text{Å})$$

$$Z_{222} = \sim 0.2623 \times 10^6 (^0K \cdot \text{Å}^9)\ (*)$$

Next, we used thermodynamic data (namely cohesive energies) for α-quartz and α-cristobalite. Employing Eqs. (6) and (14), the rest of the potential energy parameters were calculated as

*This value is only an approximation at this stage. However, (if needed) it may be perfected using bulk SiO_2 data.

$$\varepsilon_{12} = 42531.7\ (^0K)$$
$$r^o_{12} = 1.6259\ (\text{Å})$$
$$Z_{112} = 5.0086 \times 10^6\ (^0K * \text{Å}^9)$$
$$Z_{122} = 3.9999 \times 10^6\ (^0K * \text{Å}^9)$$

This set of parameters was used in Eq. (7) and correctly reproduced the cohesive energies for the β-cristobalite and β-quartz. These experimental cohesive energies are tabulated in Table 1.

For further investigation of these systems, the following programs have been prepared.

(i) Monte-Carlo Program: This program is written to handle systems containing up to three different atomic species. It uses Eq. (7) and generates appropriate Markov chain configurations of the system in a very efficient way. It stores the list of neighbors using the "large core memory" (in a CDC 7600) that reduces the computation time considerably, in particular, for larger systems.

(ii) A Software Package for Structural Characteristics of SiO_2 Systems:

This package contains basically two different programs. The first is to calculate the radial distribution function of the system. It provides the radial distribution function associated with any portion of the system; and it is able to calculate partial (i.e., $g^{(R)}_{(Si-Si)}$, $g^{(R)}_{(Si-O)}$ or $g^{(R)}_{(O-O)}$) or the total g(R) of any SiO_2 system. The second program is to calculate angular distributions for the whole system or for any subsection of the system. In particular, it is designed to calculate the distributions for angles such as (Si-O-Si) and (O-Si-O)

between the neighboring atoms.

Initial simulations were designed, in particular, to check the adequacy of the computational methods and the potential energy function. First, the bulk and the surface structures of crystalline Si and two SiO_2 forms (namely, α-cristobalite and α-quartz) were taken into consideration. In all cases the very same set of potential parameters were employed.

The results were found to be very encouraging. They indicate that (i) the type of the potential energy function is quite appropriate for these systems, and (ii) despite relatively long three-body interaction calculations, the simulation procedure (Monte-Carlo) is able to produce the equilibration (for systems of reasonable sizes) within manageable computation times.

1. Bulk Silicon

The crystalline structure of silicon was generated in a diamond cubic structure for T = 300°K corresponding to an atomic volume of 20.02 $Å^3$ (experimental data were taken from reference 8). The system contained 216 Si atoms. To mimic an infinite bulk a three-dimensional periodic boundary condition (PBC) was employed in accordance with the experimental density. The result of an equilibrated Monte-Carlo run indicated that the crystalline structure of the system is well maintained and the stability criterion was observed.

For a more stringent test one of the high pressure forms of Si (in the white tin structure) was considered. This allotropic form is much denser than the regular diamond cubic structure of Si. For both forms we investigated the

variation of the potential energy as a function of volume at the static limit. The result is shown in Fig. 8. Curves intercept each other at $V = 14.95\ A^3$ which indicates that, for $V < 14.95$, the white-tin structure would be energetically more favorable than the diamond cubic structure. This outcome agrees quite well with an atomic volume of $14.95\ A^3$ which was measured experimentally for the white-tin structure of Si [8]. Unfortunately, in this experimental report the pressure to which this volume corresponds was not stated.

2. Si(100) Surface:

In this case, we first generated an ideal (1 x 1) surface which was obtained simply from truncating the bulk crystal. The same lattice dimensions were used as above. This surface structure was taken as an initial configuration. The top layer contained 32 Si atoms out of 215 which constituted the system. For the simulation, PBC was employed in two directions (i.e., in X- and Y-directions) leaving the free surface in the Z-direction. In the relaxation process only the top layer Si atoms were considered. The rest of the atoms were held fixed in their original lattice sites but they contributed fully to the interaction energies. Figure 9 displays the surface configuration after the equilibration.* The relaxation produced a (2x2) structure consistent with the recently proposed models [9,10].

*In all cases, iterations were carried out beyond the complete equilibration point which was monitored by the variation of the total energy.

3. Bulk α-Cristobalite and α-Quartz

Bulk α-cristobalite and α-quartz were simulated to 50°K, 300°K and 2500°K. PBC was imposed in three dimensions in accordance with the experimental densities at the corresponding temperatures and species [2]. At T = 50°K and 300°K, the equilibrated systems maintained their crystalline structures quite well. The configuration of these "relaxed" structures was analyzed using the radial distribution function (RDF) and the angular distribution function (ADF) calculated from the final atomic positions. For both species the RDF produced peaks in the correct positions compared to the ideal crystals. Figure 10 displays the RDF for α-cristobalite as an example at T = 300°K for SiO, O-O and Si-Si cases as well as the total RDF. Figure 11 shows the corresponding RDF's for an ideal case. Calculated ADF's for both α-cristobalite and α-quartz produced Si-O-Si and O-Si-O angles consistent with experimental results [2]. The distribution of O-Si-O angles averaged around 109° for both cases confirming the inherent tetrahedral structure of the system. The spread in this distribution at T = 300°K was approximately ± 10°. The distribution of Si-O-Si angles at 300°K for α-cristobalite varies from 139° to 169° with an average of 154°, and, for α-quartz, it varies from 132° to 165° with an average of 147°. Figure 12 displays the ADF's for α-cristobalite at T = 300°K and the corresponding ideal crystal case (i.e., before equilibration) is shown in Fig. 13.

To test the high temperature behaviors of the system a simulation run was carried out at T = 2595°K. The PBC imposed on the system was chosen such that it produced the correct density (1.929 gr/cc) at this temperature. RDF obtained after the complete equilibration produced more diffused peaks than the lower temperature cases which is indicative of a molten state (see Fig.

14). However, the general feature of the total RDF was still preserved. For the ADF case also we obtained peaks somewhat more spread. The distribution for the Si-O-Si angles varies from 145° to 180° averaging around 165 degrees. This indicates a shift to larger angle region with increased temperature, as expected. The distribution of O-Si-O angles, on the other hand, was found well around 109° region (with a spread of ± 15°). This confirms that the stability of the tetrahedral units, even at this high temperature, is still maintained (see Fig. 15).

These results, in particular those for 50°K and 300°K, are very important and indicate that the present semi-empirical potential function is quite adequate and it is able to reproduce stable crystalline structure of α-cristobalite and α-quartz satisfactorily. Of course, the most interesting part is the preservation of the crystalline structures in the Monte-Carlo scheme at finite temperatures. At the present, there is no simple potential function in the literature that can be used in a similar computer study for crystalline SiO_2 forms. The only model potential function which can be found in the literature is for the amorphous SiO_2. It is based on an ionic model and employs a two-body Born-Mayer-Huggins-type potential function [3-6]. This potential, however, fails to reproduce an acceptable crystalline SiO_2 form as a stable state.

These present results are particularly important because they clearly demonstrate the role played by the three-body forces in the stability of crystalline SiO_2 forms.

4. Surfaces of α-Cristobalite and α-Quartz

Surface structures for the (001) plane of α-cristobalite and (0001) plane of α-quartz were taken into consideration. These surfaces were first generated by truncating the corresponding ideal crystals as in the case of Si(100) explained above. Both of these surfaces are O-rich surfaces. Two O atoms from each surface tetrahedron are exposed. Figure 16 demonstates top and side views of the surfaces in their initial configurations. Both systems contained 216 atoms. For α-cristobalite, only the top 54 atoms and, for α-quartz, only the top 72 atoms were included in the relaxation procedure. The rest of the atoms were held fixed in their lattice positions, but they contributed fully in the energy calculations. PBC was applied in two dimensions to provide a continuous surface layer. Satisfactory equilibration was reached after approximately 1500 iterations. Top and side views of the equilibrated surfaces are shown in Fig. 17. Both surfaces exhibited similar patterns. The top layer O atoms of the neighboring tetrahedra were paired and formed so called "peroxide bridges," [11] with an average O-O distance of 1.2 Å. Figure 18 displays the RDF for the relaxed α-cristobalite surface region. The first peak is due to the peroxide bridge which does not exist in the RDF's of bulk structures. All other peaks are approximately in their bulk positions. On these reconstructed surfaces one can distinguish three different types of tetrahedral units (i) with no peroxide-bridge, (ii) with only one peroxide-bridge and (iii) with two peroxide bridges connected to both sides. At the moment the energetics and the exact geometry of the different tetrahedral units are not determined.

This preliminary test clearly indicates that, in the study of surfaces the role played by the three-body interactions is very important, and the

present potential energy function is well suited for such investigations.

TABLE 1

	α-Crist.	α-quartz	β-Crist.	β-quartz
R(Si-Si)	3.0767	3.0579	3.0880	3.0982
R(Si-O)	1.60	1.60	1.55	1.63
R(O-O)	2.60	2.63	2.53	2.60
a^m_{11}	4.0575	4.1148	4.0388	4.1048
a^m_{12}	9722.33	8328.37	9796.98	9870.78
a^m_{22}	41.3494	36.7629	42.0266	48.1561
a^m_{21}	4861.17	4164.88	4898.46	4929.74
a^n_{11}	5.2401	5.6759	5.0999	5.6325
a^n_{12}	202.442	188.962	202.892	204.702
a^n_{22}	19.5795	20.2410	19.3041	21.5124
a^n_{21}	101.221	94.4946	101.444	102.302
T_{111}	5.7840	8.3242	4.94088	8.0688
T_{112}	-191.313	-117.663	-202.276	-175.685
T_{122}	174.512	195.381	167.158	195.231
T_{222}	62.0504	76.5891	57.5318	73.9876
T_{221}	174.555	195.427	167.131	195.237
T_{211}	-47.8405	-29.4278	-50.5788	-43.9041
Cohesive Energy (kcal/mole)	-412.14	-412.540	-417.43	-417.85

REFERENCES

1. Previous Progress Rep. [1 Sept. 1981 - 28 Feb. 1982].

2. K. Hubner , Phys. Stat. Sol. (a) 40, 487 (1977).

3. T.F. Soules, J. Chem. Phys. 71, 4570 (1979).

4. S.K. Mitra, M. Amini, D. Fincham and R.W. Hockney, Phil. Mag. B, 43, 365 (1981).

5. S.H. Garofalini, J. Chem. Phys. 76, 3189 (1982).

6. W.R. Busing, J. Chem. Phys. 54, 3008 (1972).

7. R.L. Mozzi and B.E. Warren, J. Appl. Crystallog. 2, 164 (1969).

8. J. Donohue, "The Structures of the Elements (John Wiley, New York, 1974), p. 262.

9. F. Jona, H.D. Shih, D.W. Jepsen and P.M. Marcus, J. Phys. C: Solid State Phys., 12, L455 (1979).

10. M.J. Cardillo, G.E. Becker, Phys. Rev. B21, 1497 (1980).

11. C.Y. Su, P.R. Skeath, I. Lindau and W.E. Spcier, J. Vac. Sci Technol, 19, 481 (1981).

FIGURE CAPTIONS

1. Schematic representation of atomic system for interaction between copper and silver.

2. Simulation of Cu movement on Ag(111).

3. Close-up view of Fig. 2.

4. Trajectories of the atoms within the top layer of the Ag(111) substrate at the Cu/Ag interface.

5. Trajectories of the atoms within the bottom layer of the Cu adsorbate at the Cu/Ag interface.

6. Potential energy profile across the interface illustrating the stronger binding among the adatoms.

7. Virial profile across the interface reflecting the mismatch of the sites at the interface (adlayer side dilates while the substrate side contracts).

8. Cohesive energy of silicon as a function of its volume. Curve 1 is for diamond cubic structure and curve 2 is for white tin strucutre. Energy values are reduced by the two-body energy parameter, ϵ, and the volume is in A^3.

9. Reconstructed Si(100) surface. Largest symbols represent top layer Si atoms. Smaller symbols are 2nd and 3rd layer atoms. Only top layer Si atoms were relaxed.

10. Radial distribution function for bulk α-cristobalite at T = 300°K, after the equilibration. (a), (b), (c) and (d) display distribution of Si-O, O-D, Si-Si bonds and the total RDF, respectively.

11. Radial distribution function for bulk α-cristobalite, initial state. (a), (b), (c) and (d) are the distribution of Si-O, O-O, Si-Si bonds and the total RDF, respectively.

12. Percentage distribution of bond angles for α-cristobalite at 300°K after equilibration. (a) and (b) exhibit distributions for O-Si-O and Si-O-Si angles respectively.

13. Percentage distribution of bond angles for α-cristobalite at the initial state. (a) and (b) display distributions for O-Si-O and Si-O-Si angles, respectively.

14. The radial distribution function at T = 2595°K. (a), (b), (c) and (d) display distributions for Si-O, O-O, Si-Si bonds and the total RDF, respectively.

15. The distribution of bond angles at T = 2595°K. (a) and (b) are the distribution of O-Si-O and Si-O-Si angles, respectively.

16. α-cristobalite (001) surface structure at the initial state. (a) Top view, (b) and (c) are the side views. α-quartz (0001) surface structure at the initial state, (d) tcp view, (e) and (f) display side views.

17. Equilibrated structure for α-cristobalite at 300°K. (a) Top view (b) and (c) are side views; and equilibrated structure for α-quartz at 300°K (d) top view (e) and (f) are the side views.

18. The total radial distribution function for α-cristobalite at 300°K after equilibration. Only surface region atoms are included.

ORIGINAL PAGE IS
OF POOR QUALITY

FIGURE 4

MULTILAYER
SIMULATION
CU ON AG(111)

TIME ELAPSED- 3.480×10^{-13}

• ATOMS IN VIEW-796

VIEW:	POINT	VECTOR
X	10.0000	-10
Y	22.0000	-22
Z	10.0000	-15

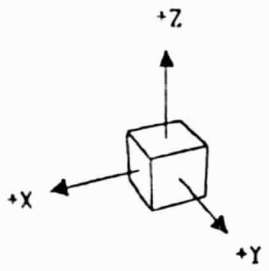

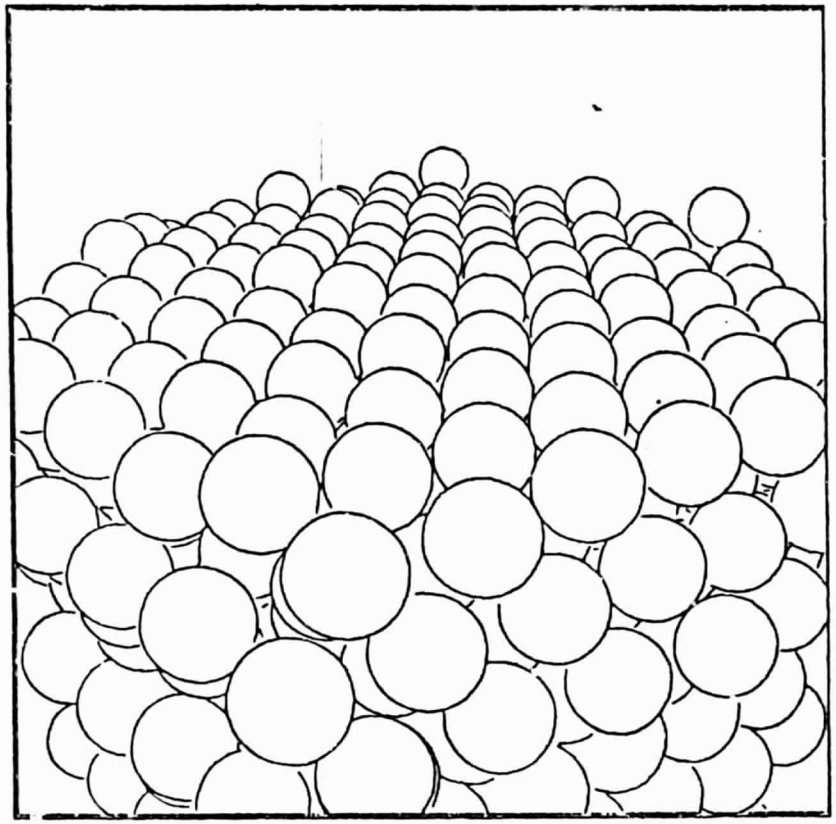

FIGURE 2

FIGURE 3

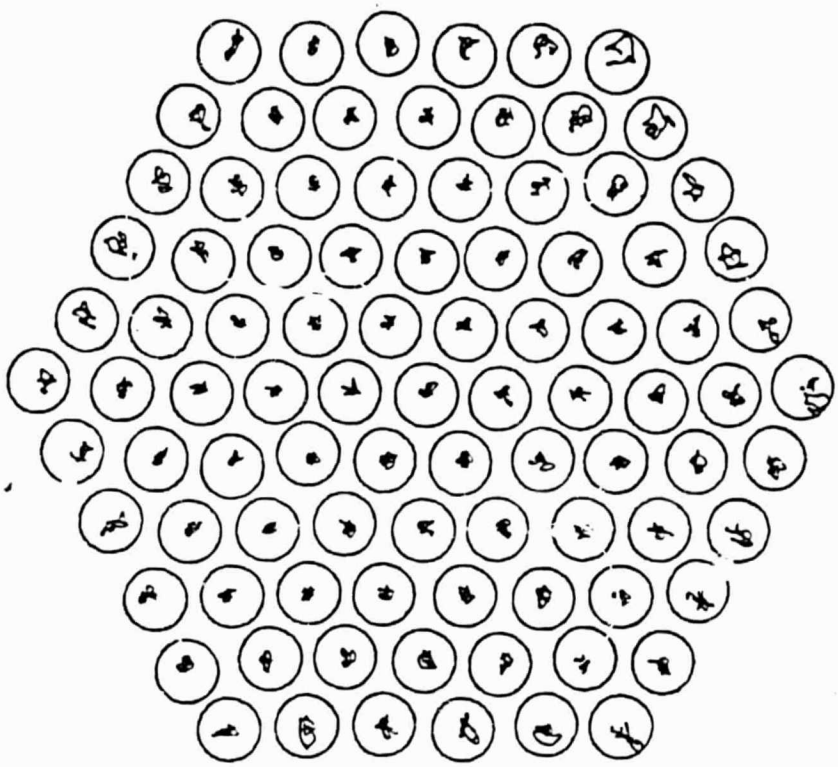

FIGURE 4

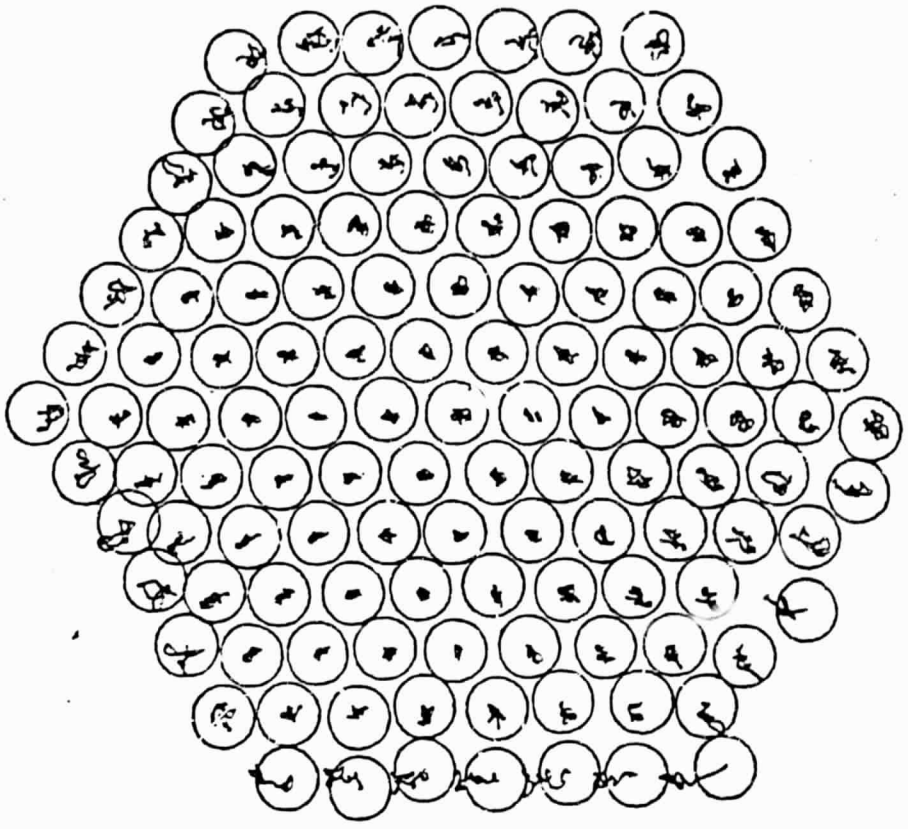

FIGURE 5

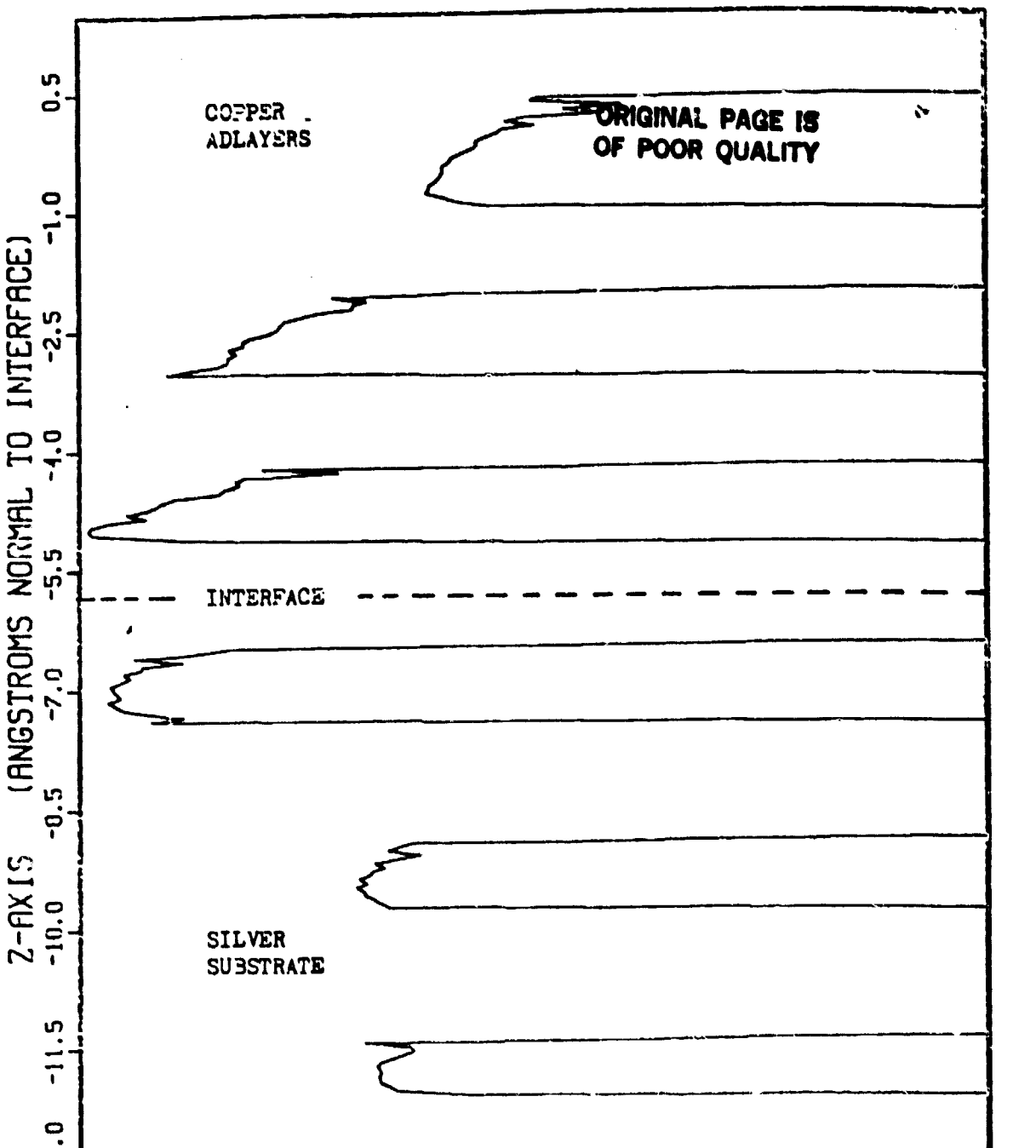
COPPER
ADLAYERS
ORIGINAL PAGE IS
OF POOR QUALITY
INTERFACE
SILVER
SUBSTRATE
Z-AXIS (ANGSTROMS NORMAL TO INTERFACE)
0.5
-1.0
-2.5
-4.0
-5.5
-7.0
-0.5
-10.0
-11.5
-13.0
-3.4700
-2.8316
-2.3133
-1.7350
-1.1567
-0.5783
0.0000
PE (EV/ATOM)

FIGURE 6

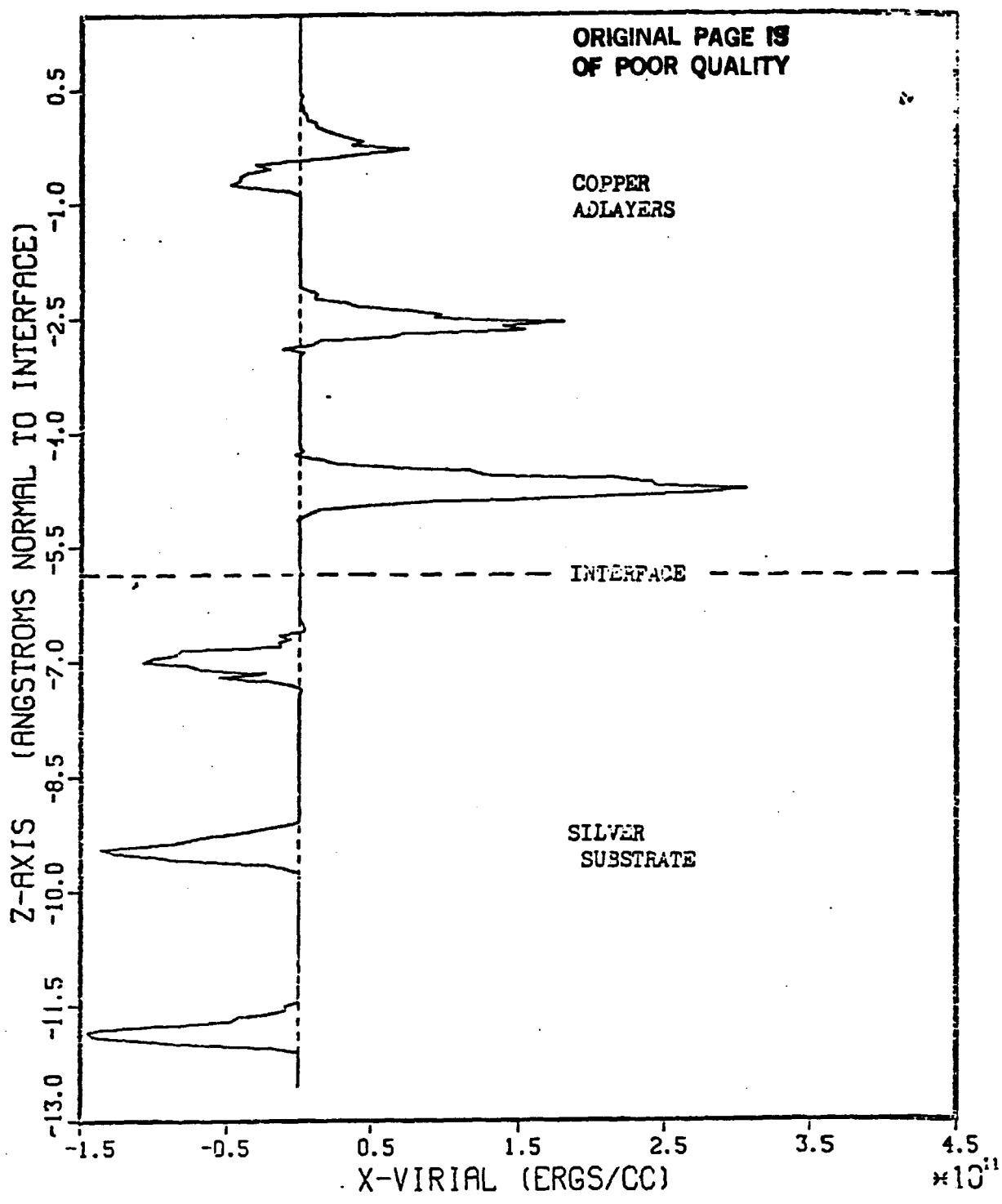
ORIGINAL PAGE IS
OF POOR QUALITY
COPPER
ADLAYERS
INTERFACE
SILVER
SUBSTRATE
Z-AXIS (ANGSTROMS NORMAL TO INTERFACE)
0.5
-1.0
-2.5
-4.0
-5.5
-7.0
-8.5
-10.0
-11.5
-13.0
-1.5
-0.5
0.5
1.5
2.5
3.5
4.5
X-VIRIAL (ERGS/CC)
*10^11

FIGURE 7

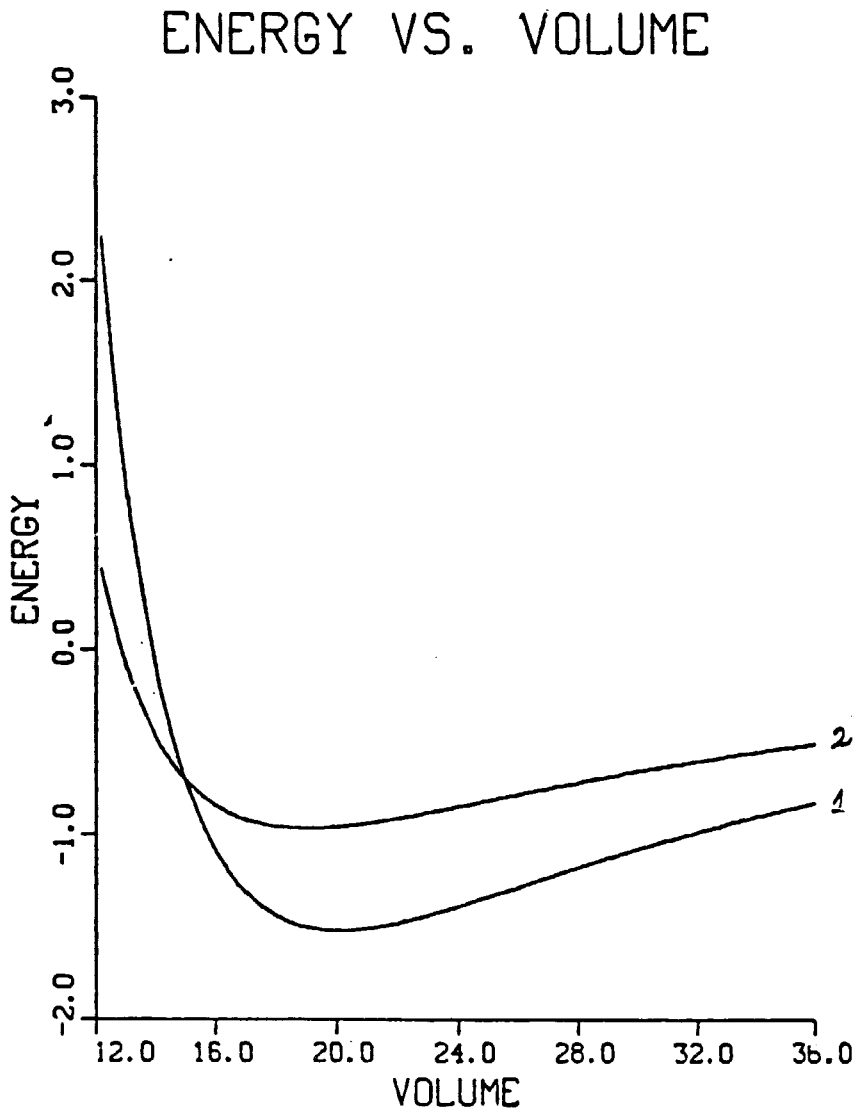

Fig. 8

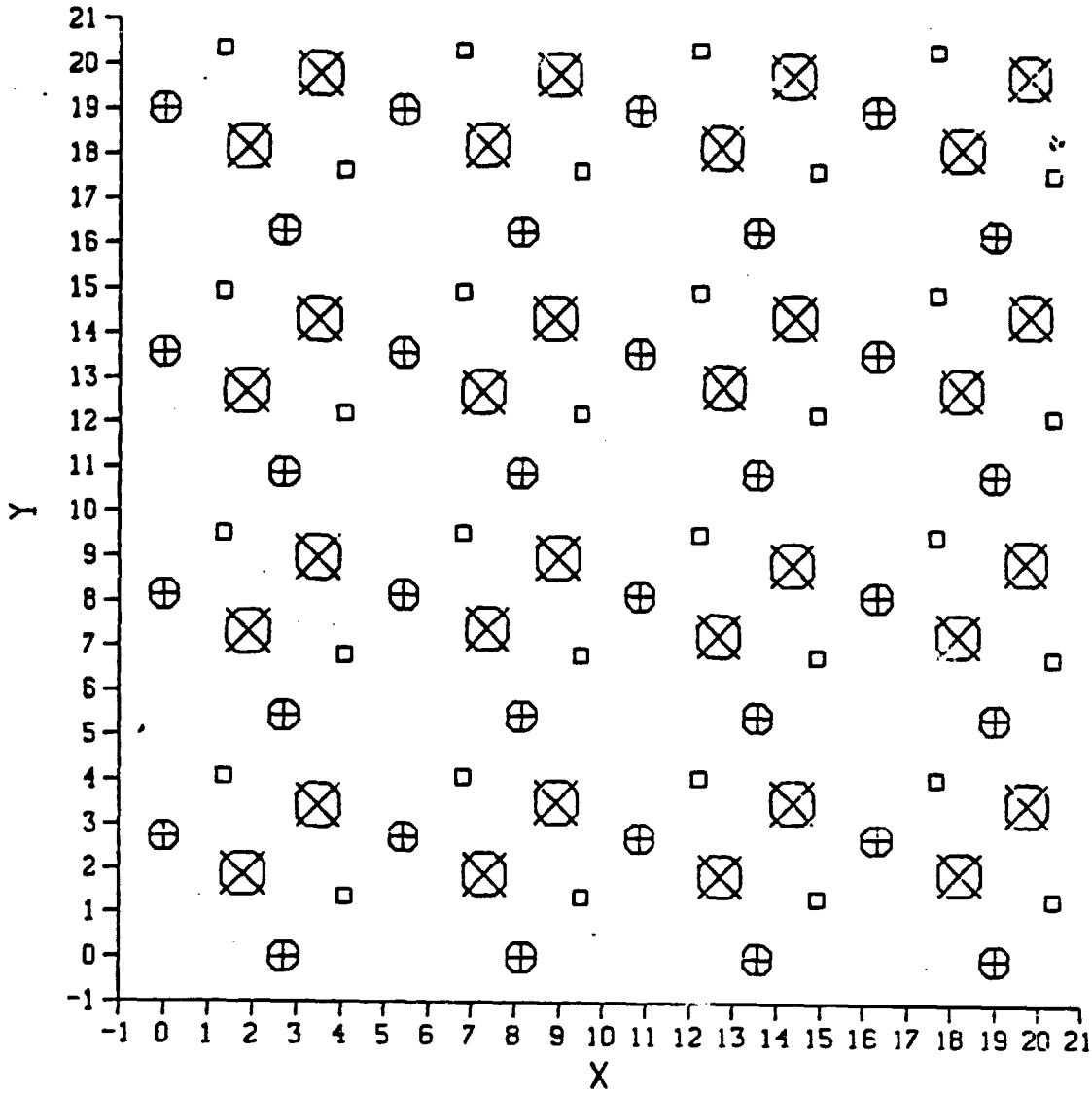

ORIGINAL PAGE IS
OF POOR QUALITY

84

Fig. 9

From D0001A.

RADIAL DISTRIBUTION BOND LENGTH

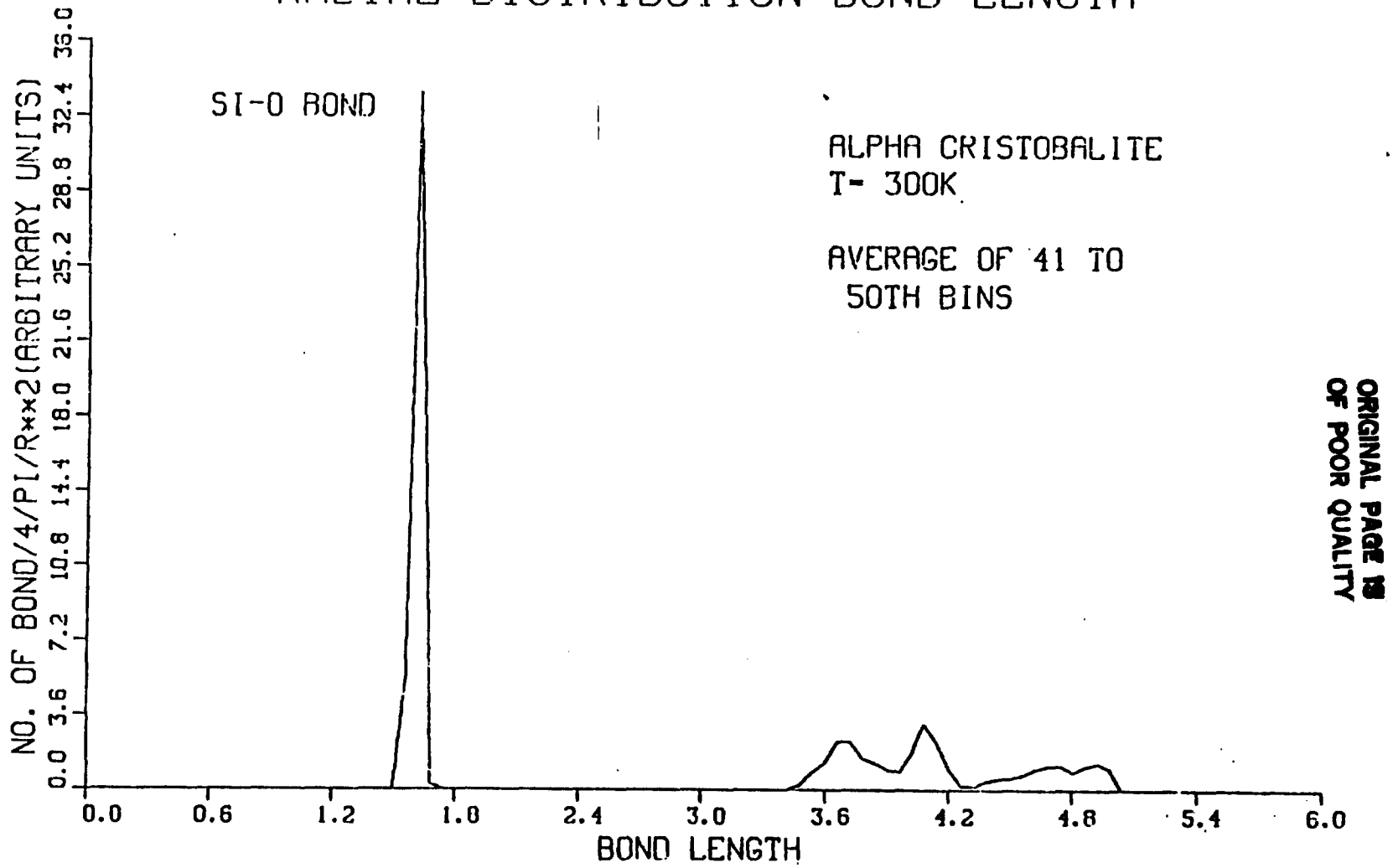

Fig. 11a

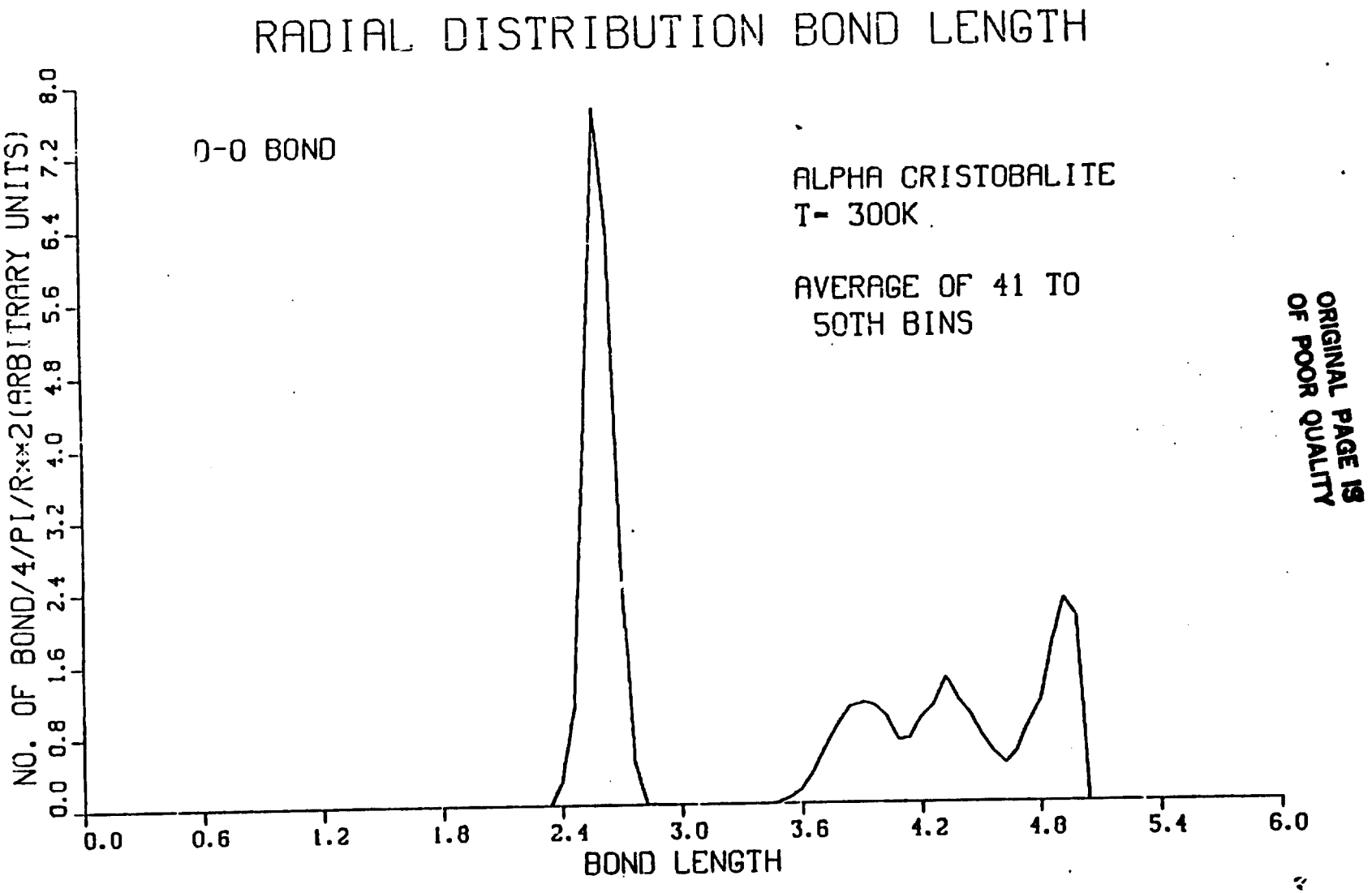

Fig 106

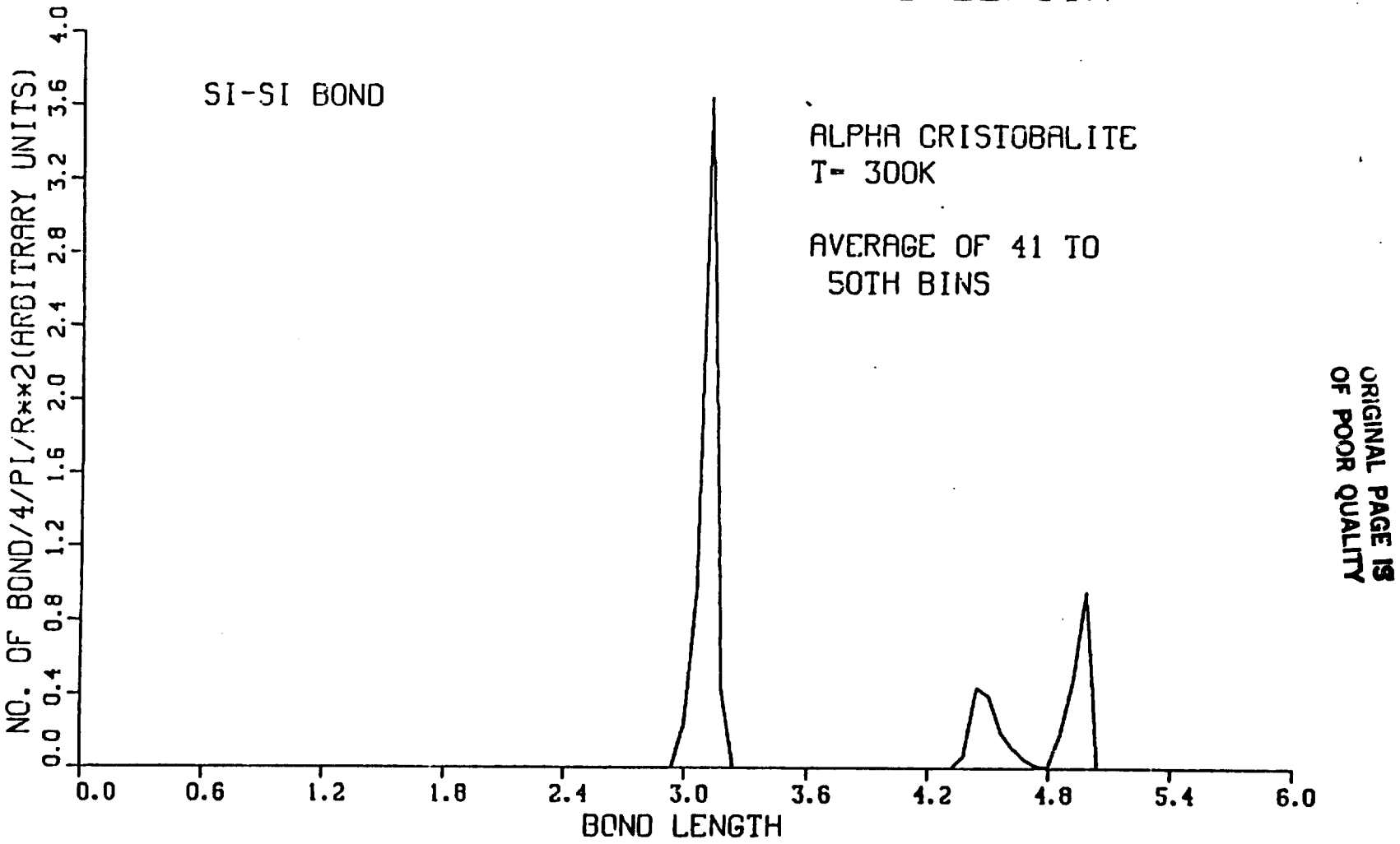

Fig 10c

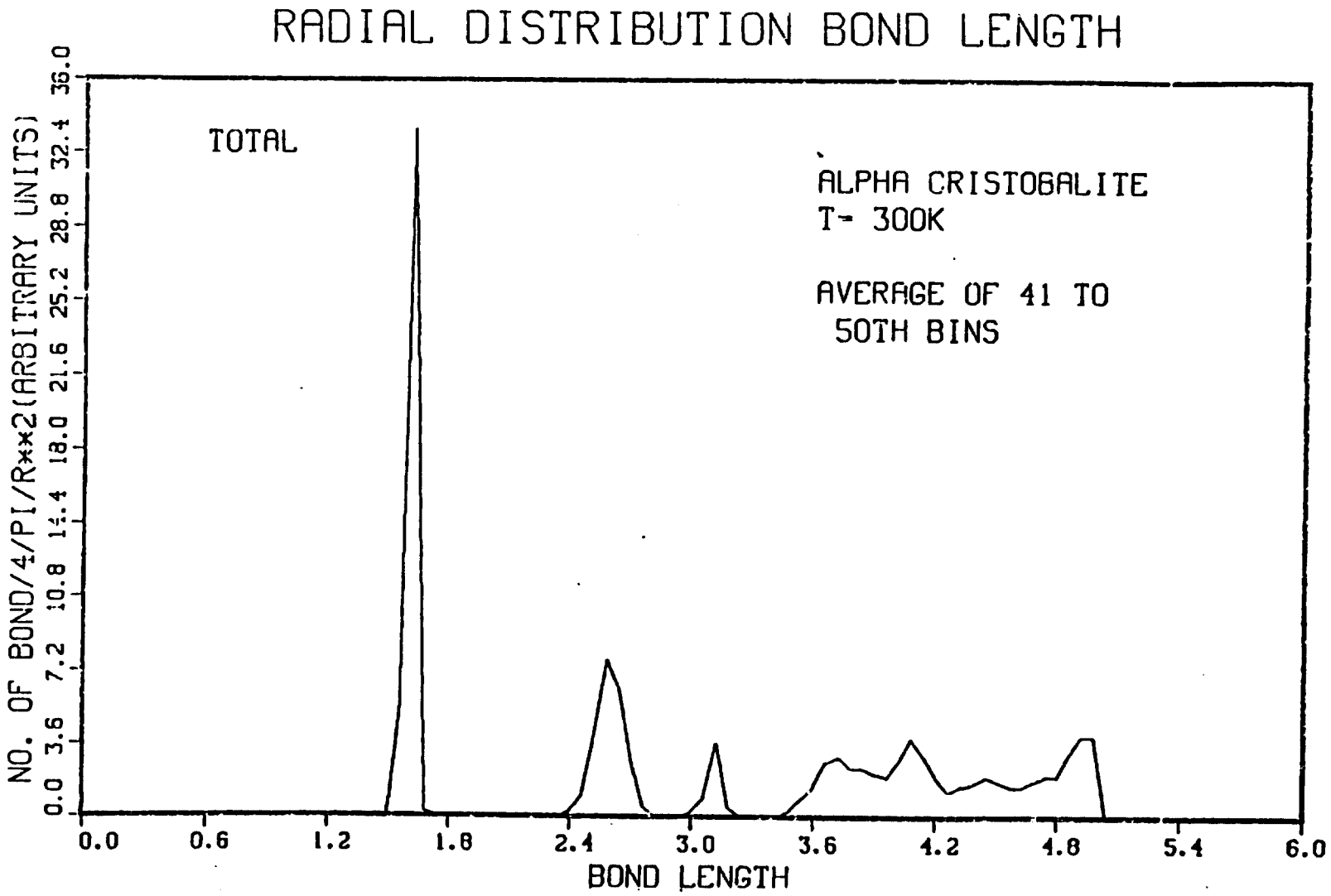

Fig 10 d.

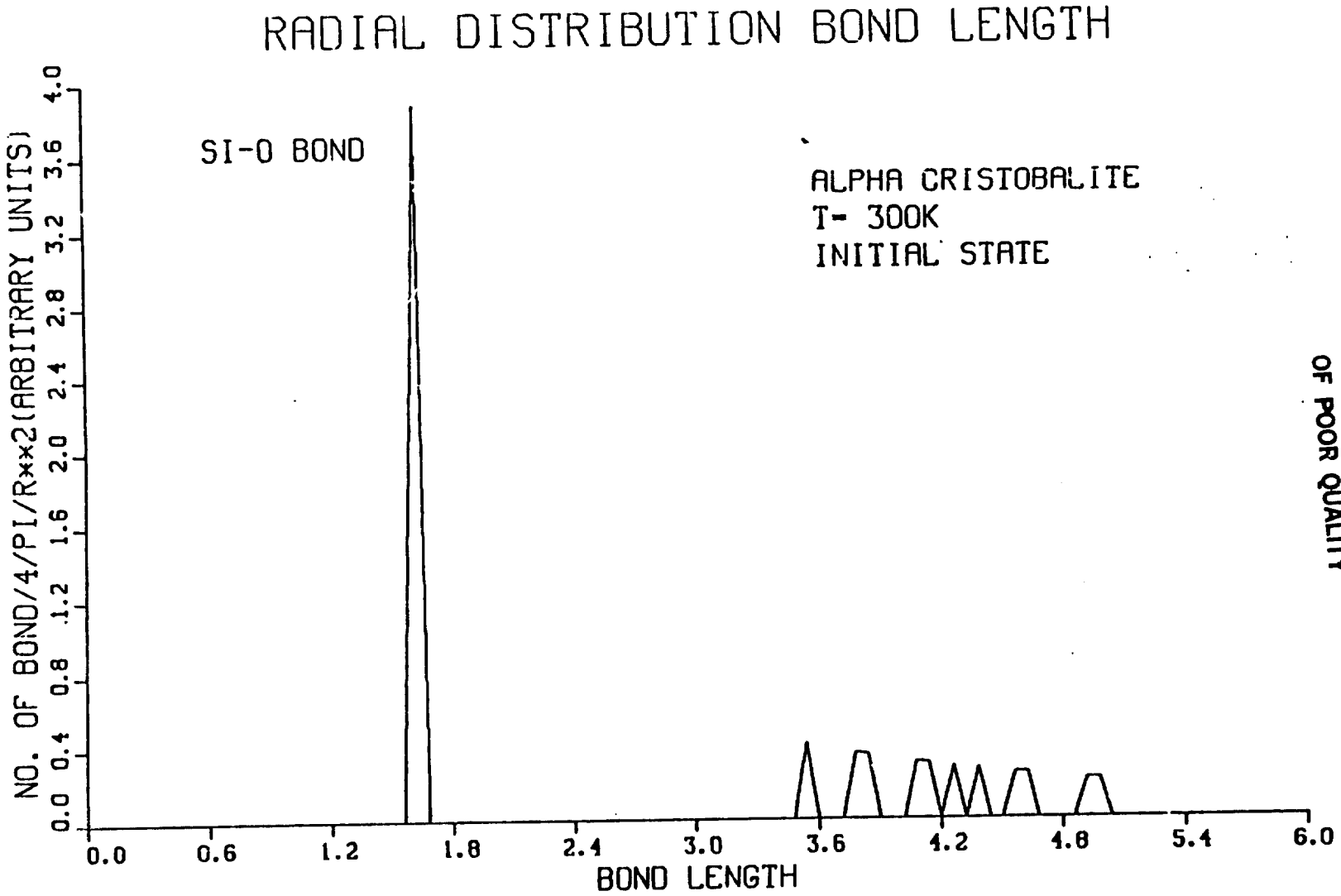

Fig 11a

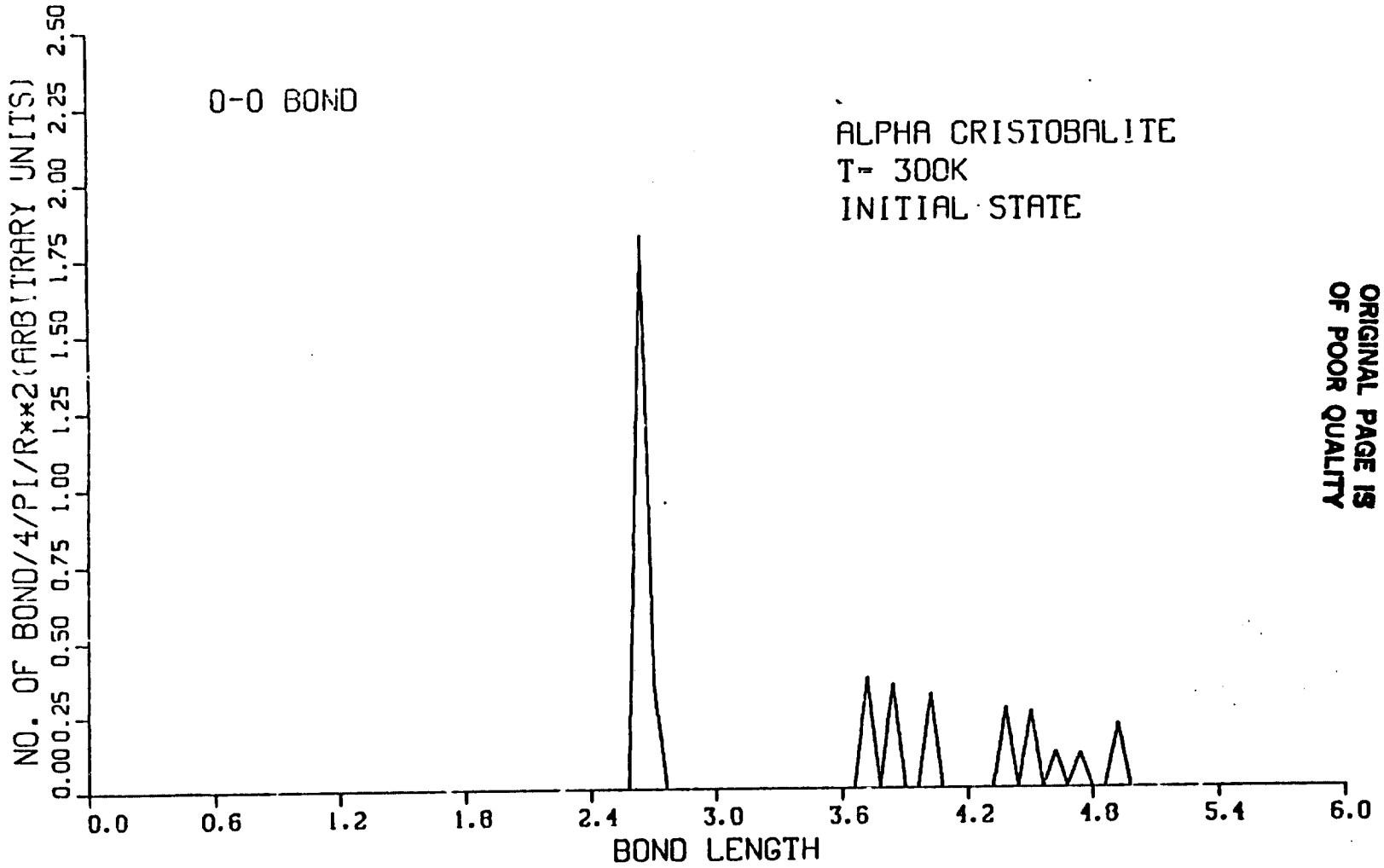

Fig 11.4

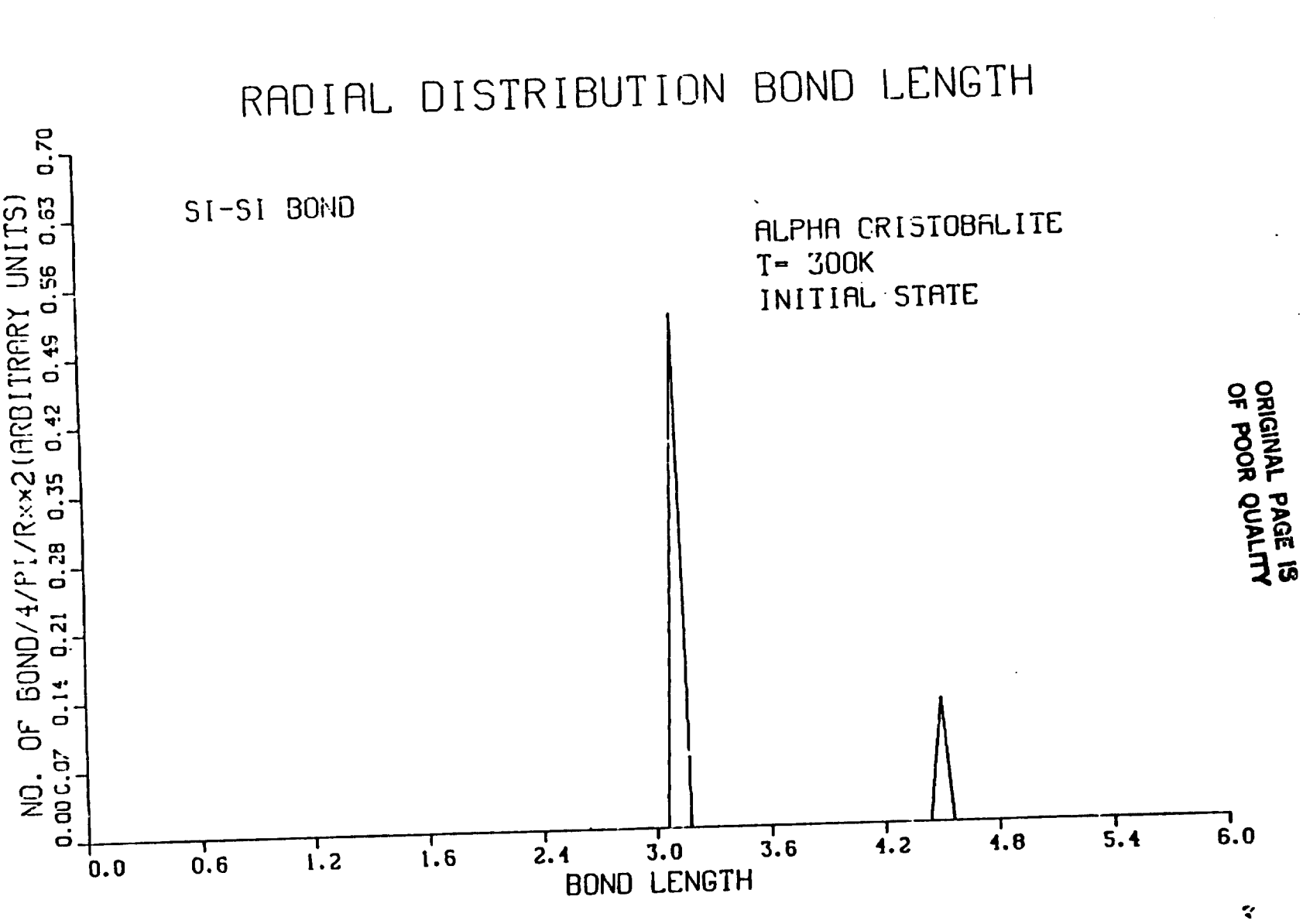

Fig 11 c

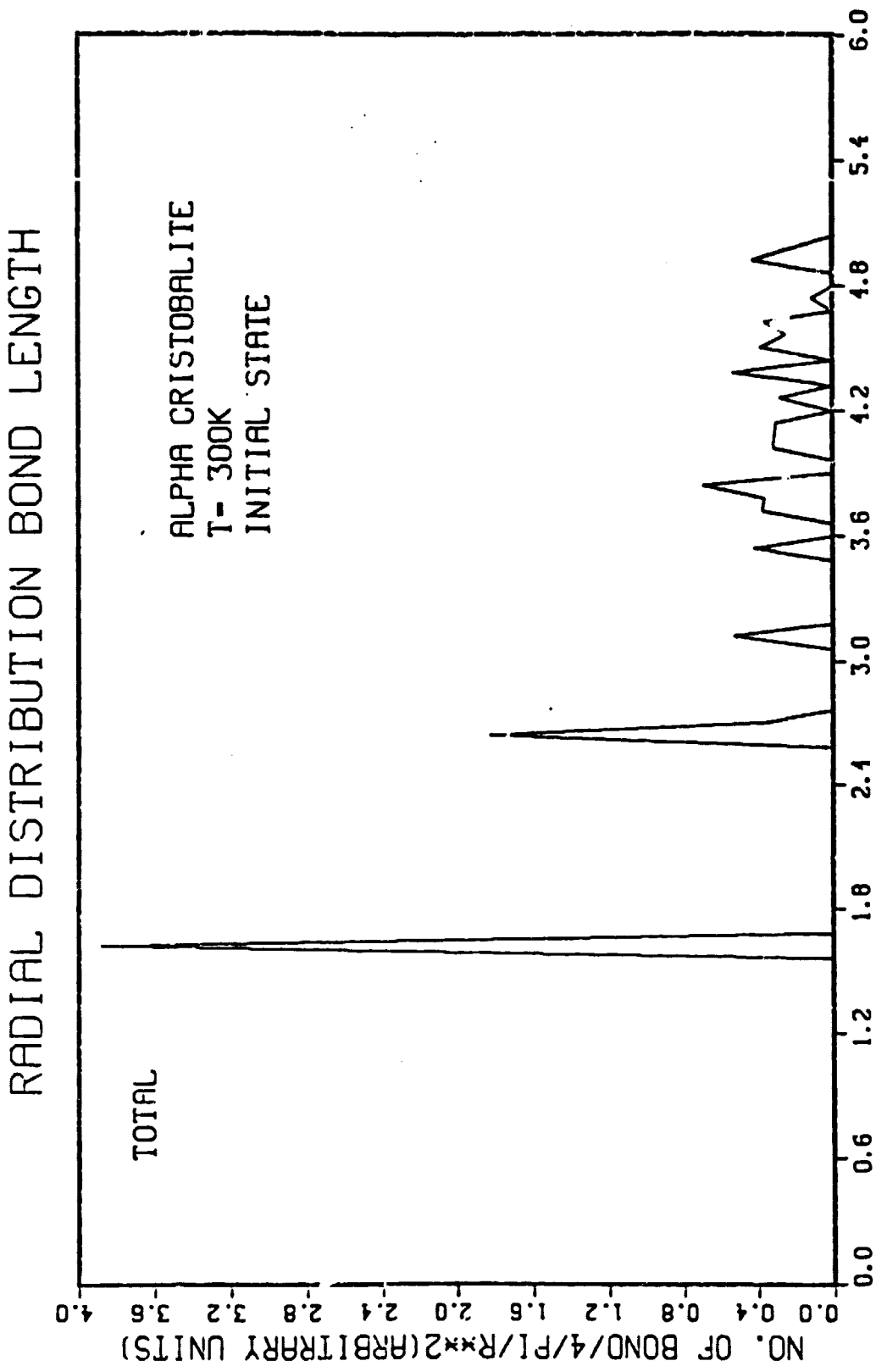

Fig. 11d

PERCENTAGE DISTRIBUTION OF BOND ANGLES

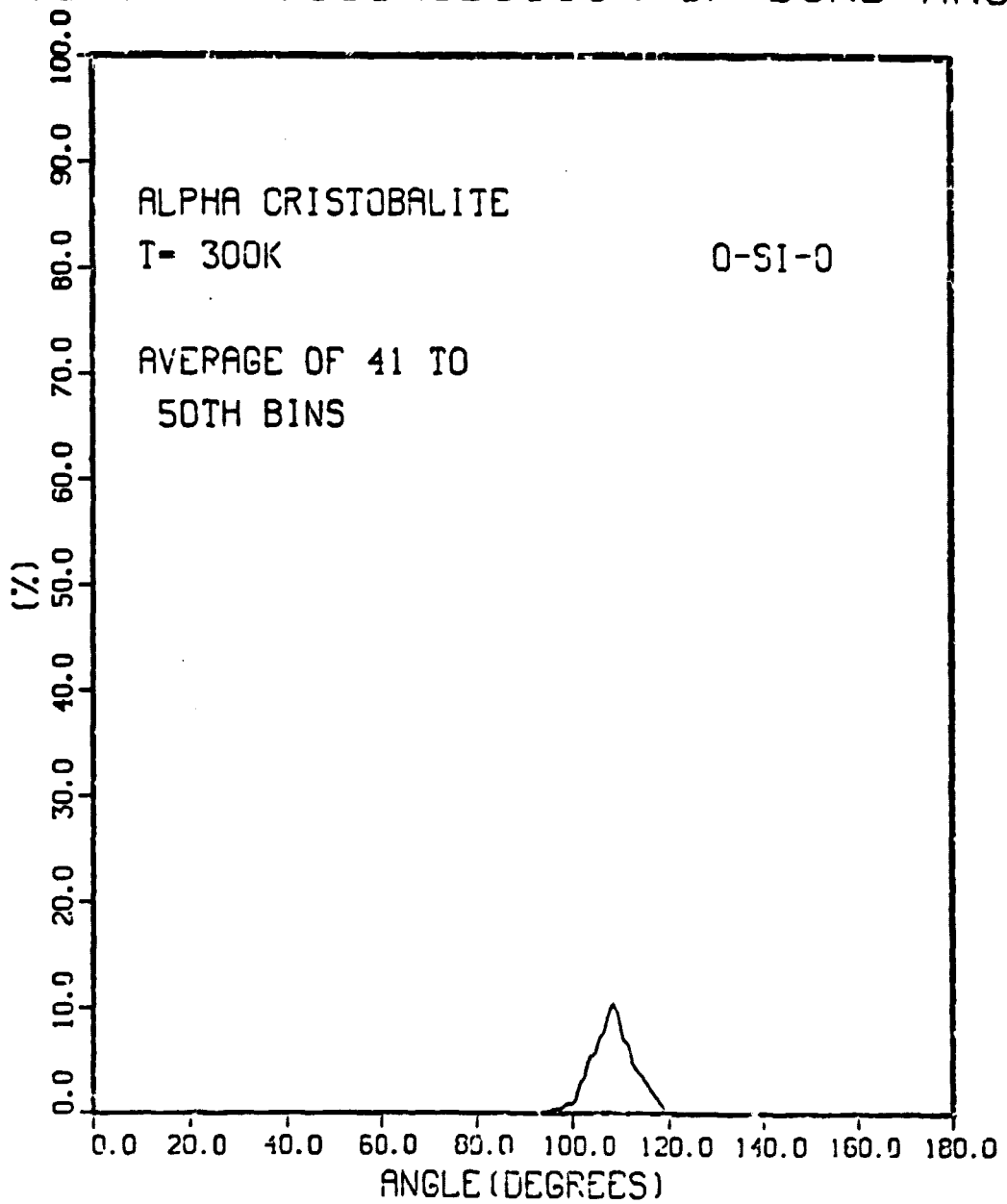

Fig. 12a

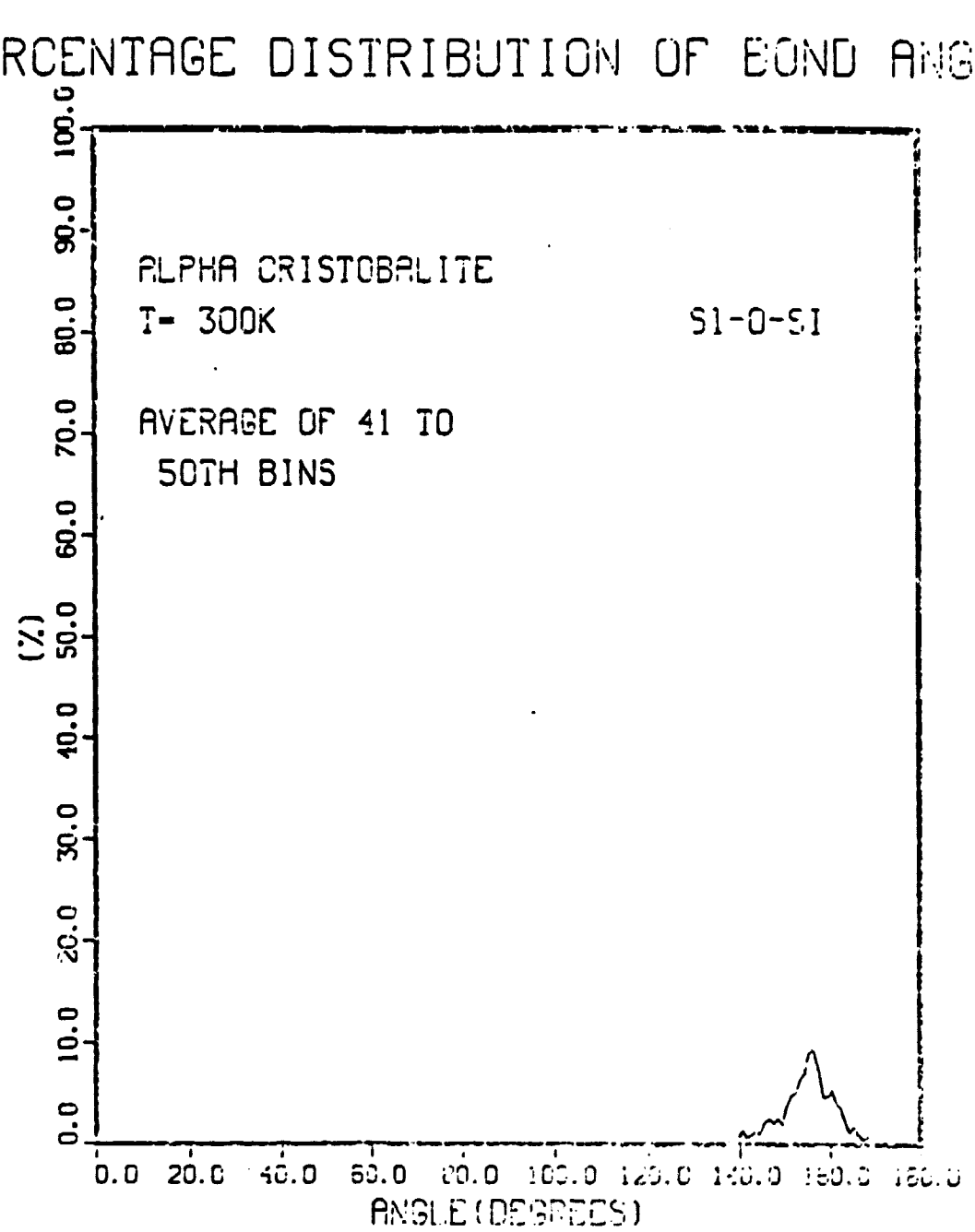

Fig. 12b

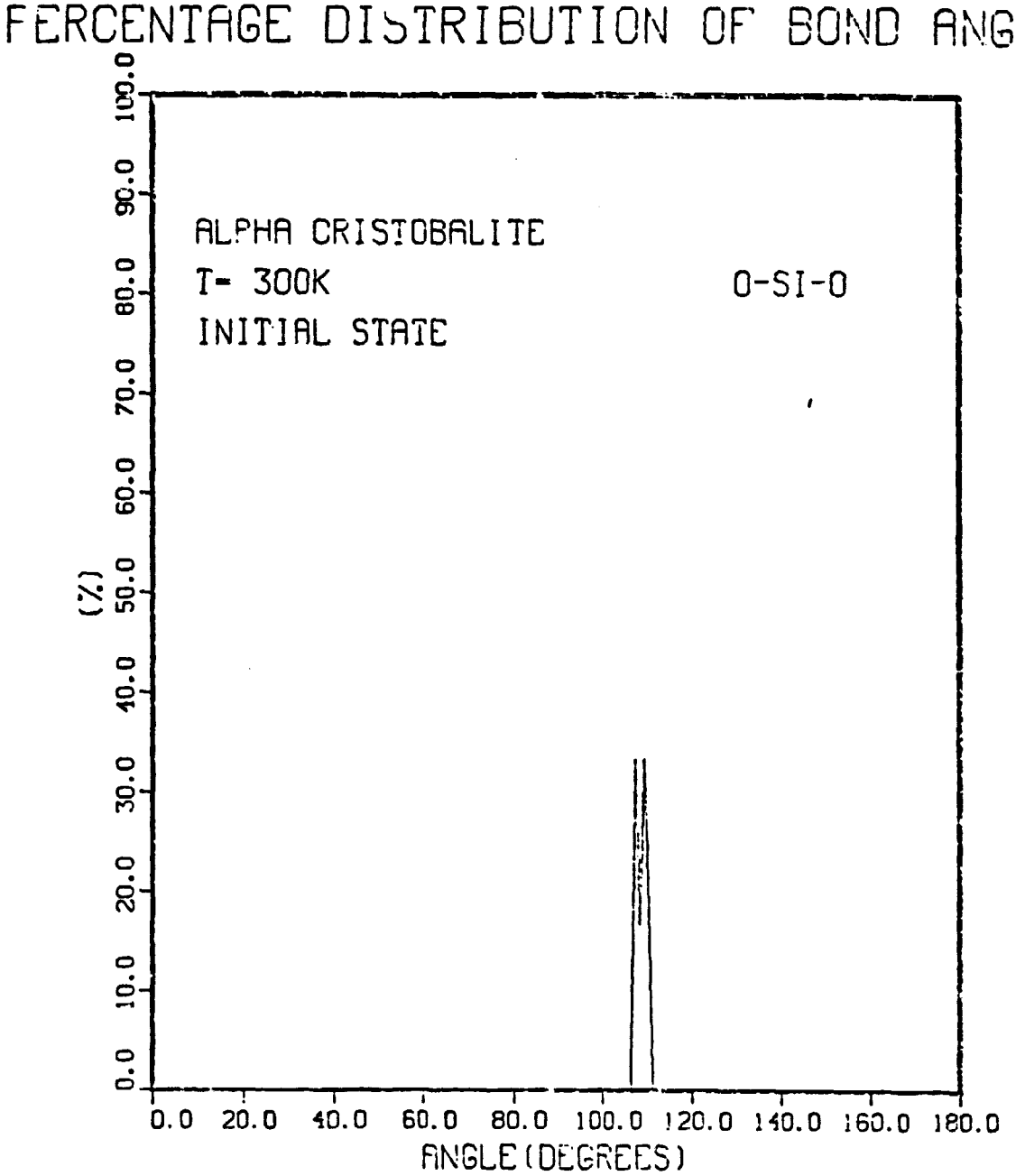

Fig. 13a

PERCENTAGE DISTRIBUTION OF BOND ANGLES

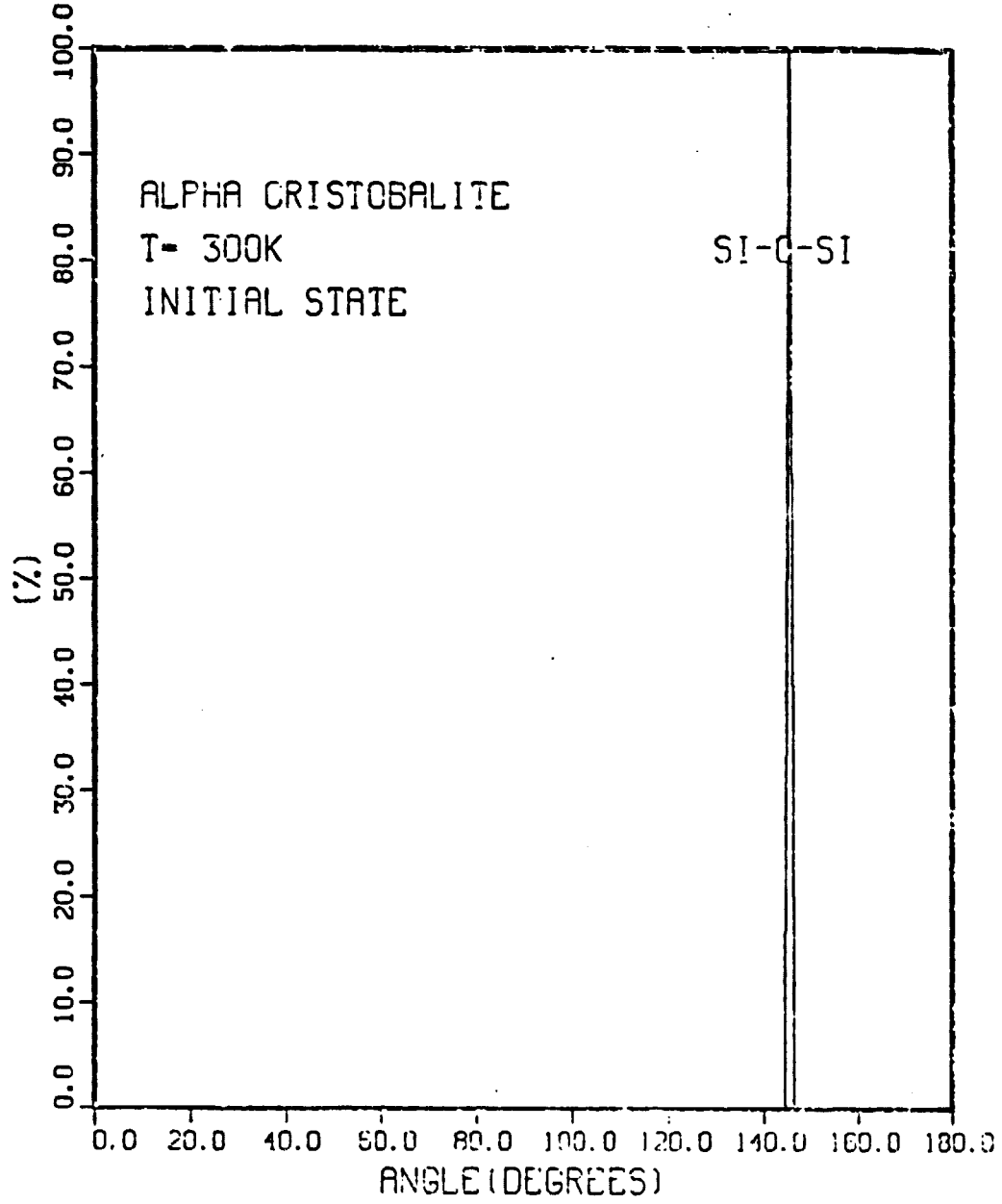

Fig. 136

RADIAL DISTRIBUTION BOND LENGTH

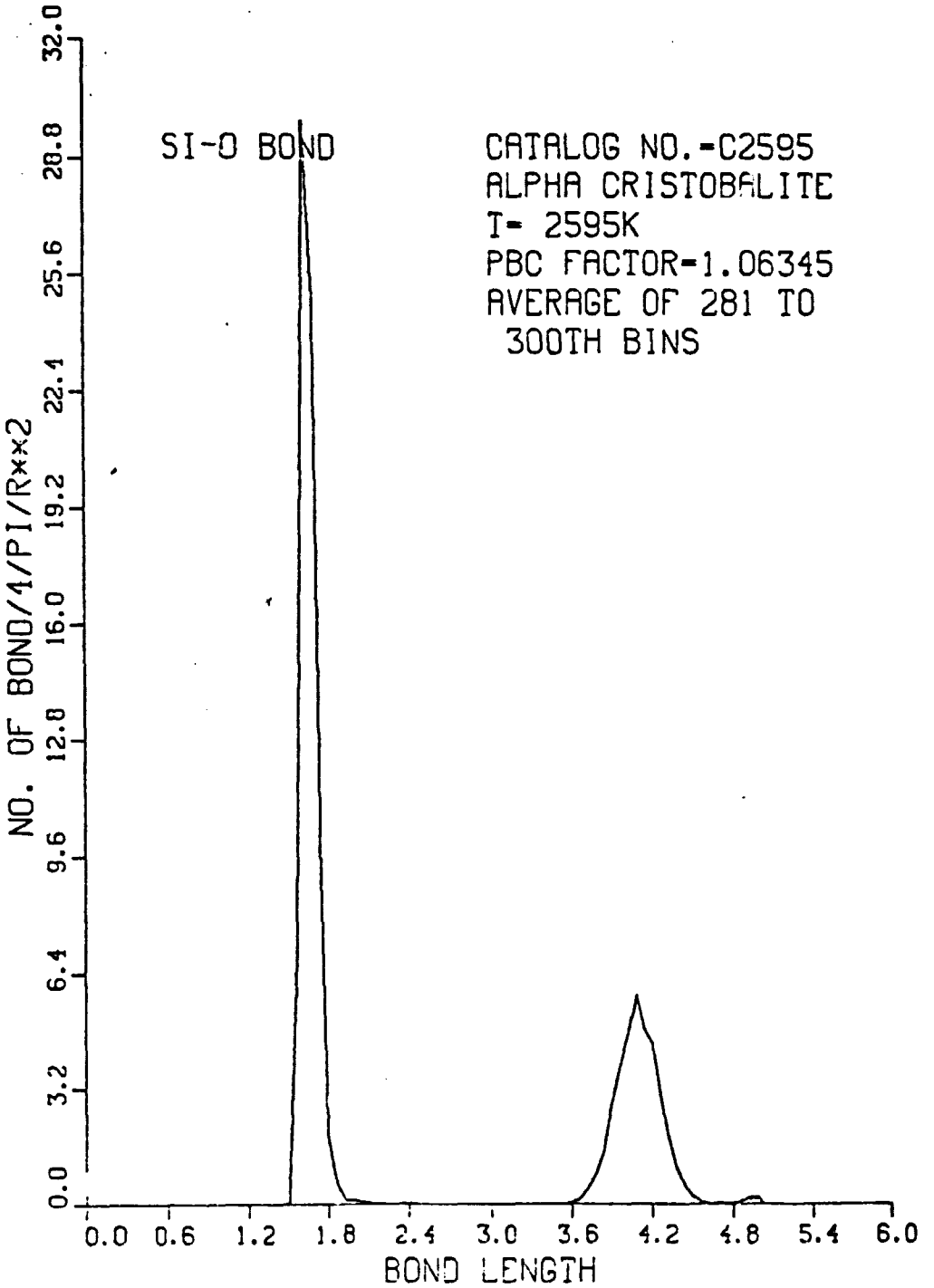

Fig. 14a

RADIAL DISTRIBUTION BOND LENGTH

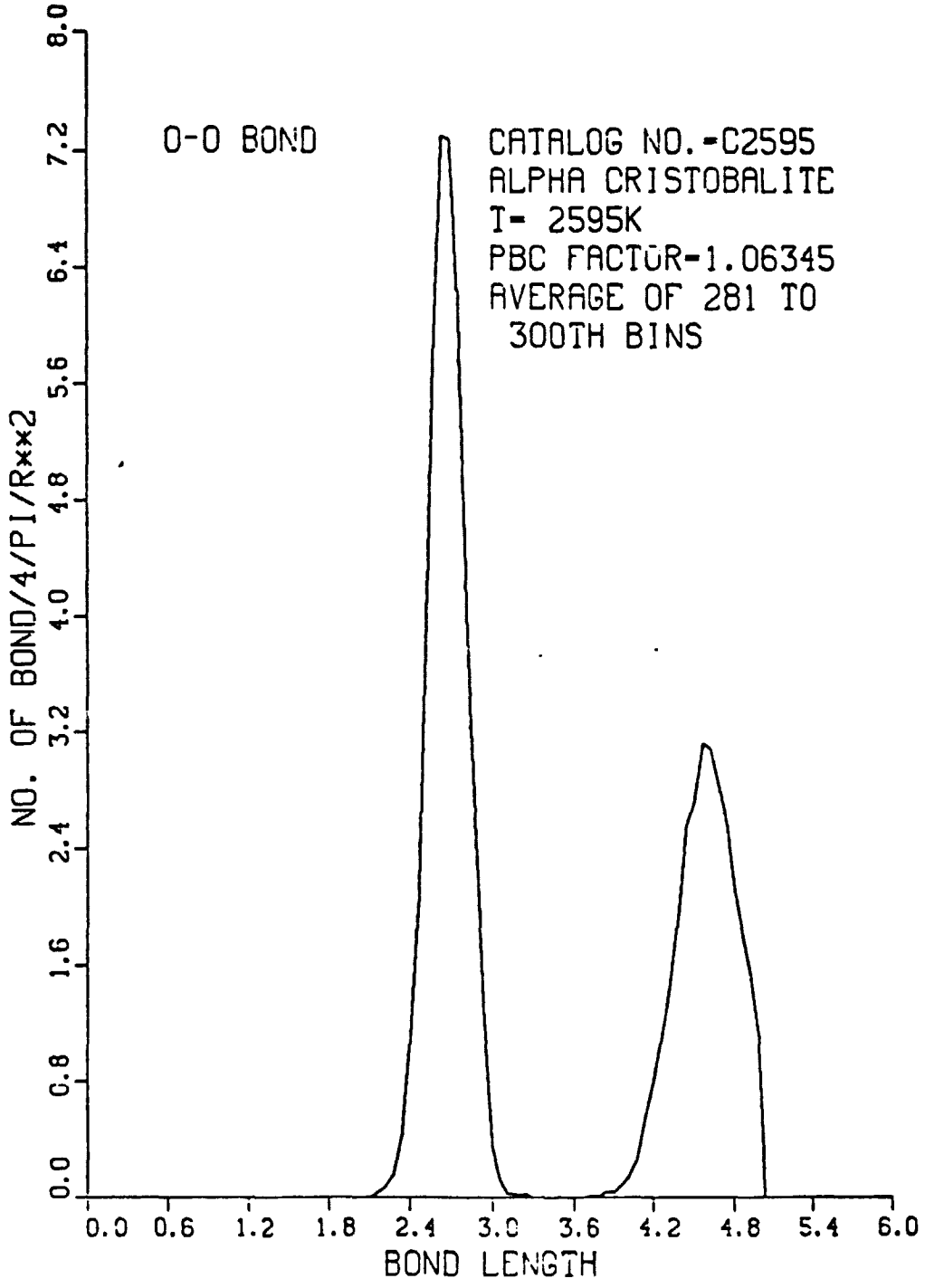

Fig. 146

RADIAL DISTRIBUTION BOND LENGTH

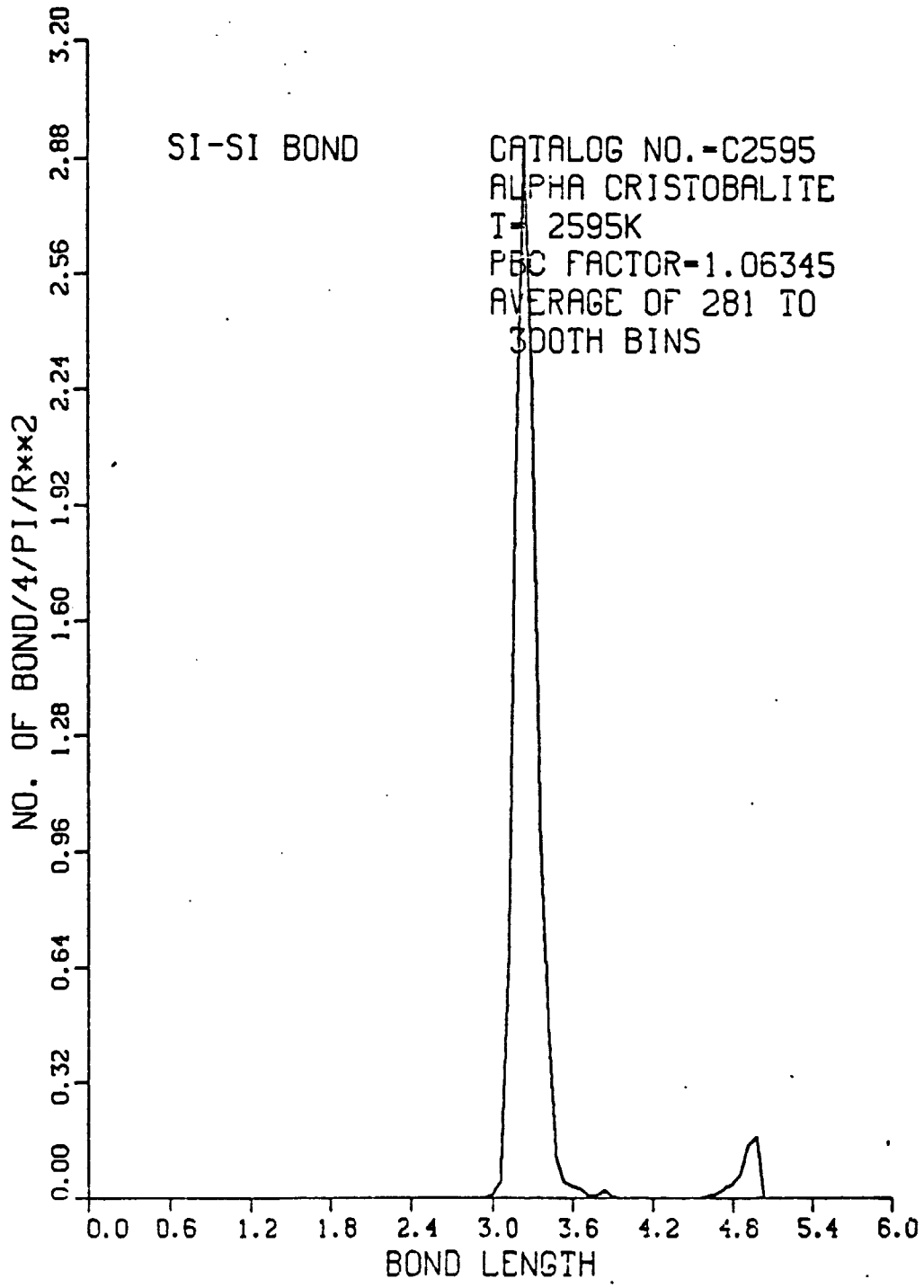

Fig. 14c

RADIAL DISTRIBUTION BOND LENGTH

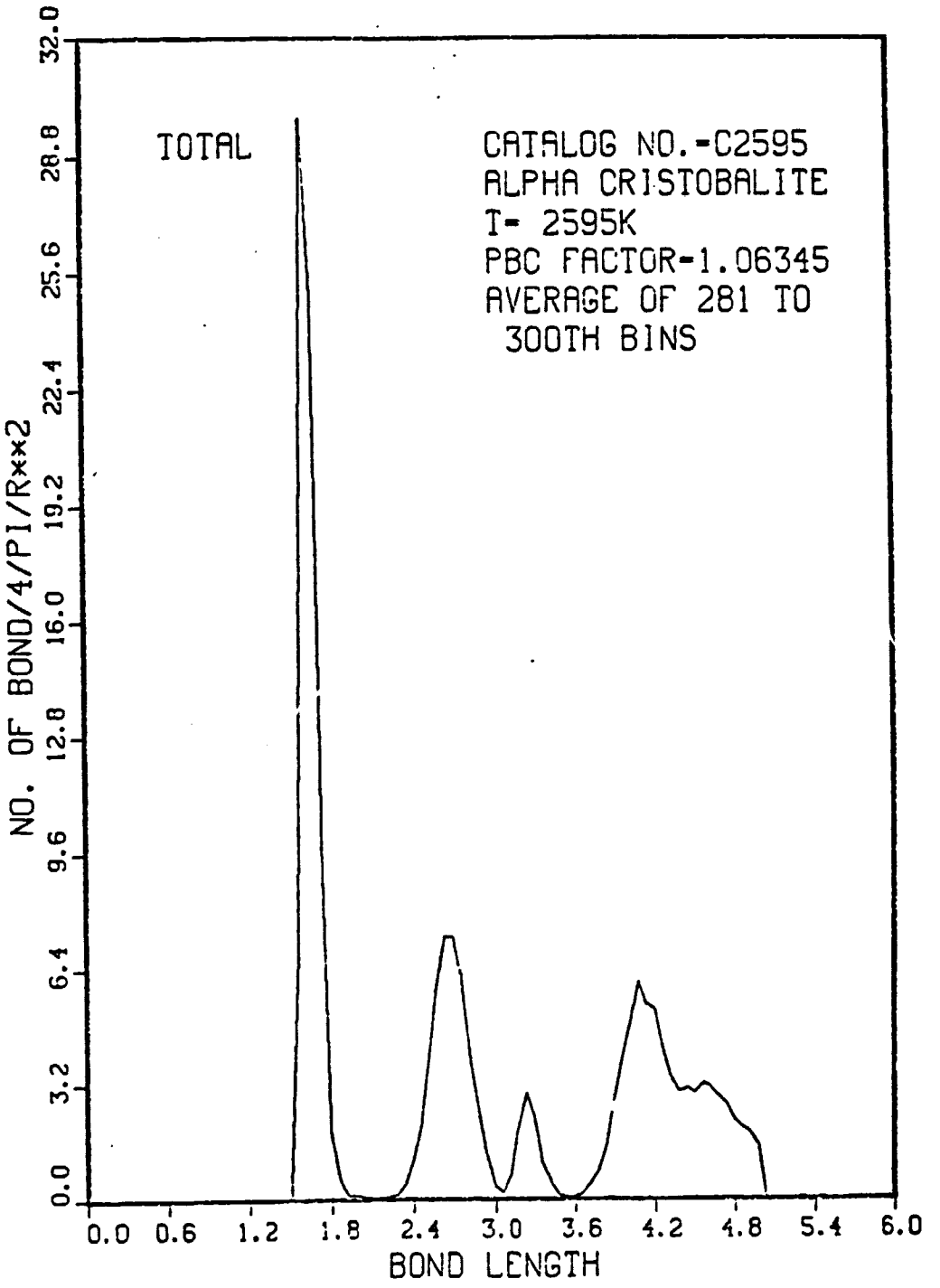

Fig. 14d

PERCENTAGE DISTRIBUTION OF BOND ANGLES

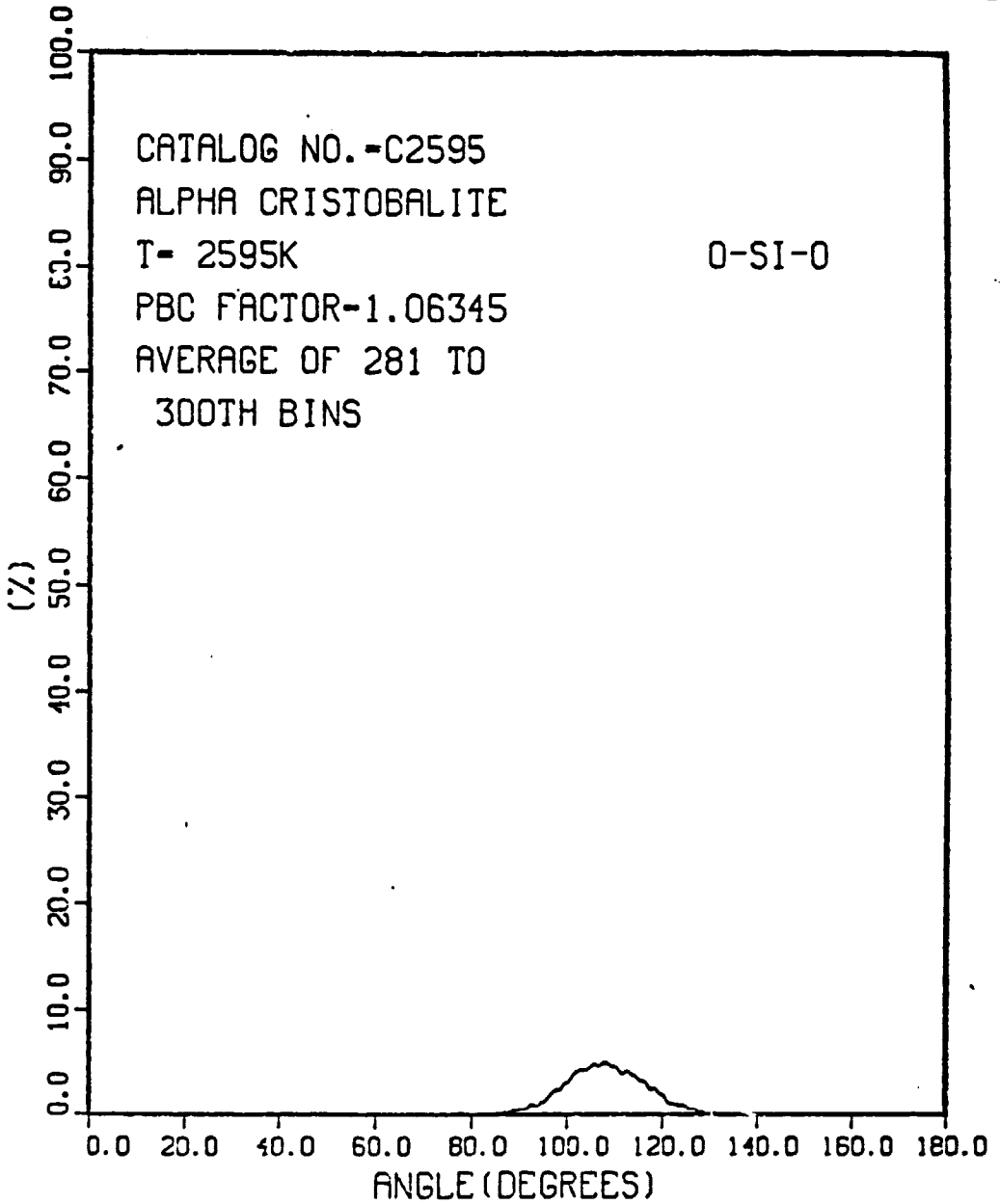

Fig. 15a

(e) PERCENTAGE DISTRIBUTION OF BOND ANGLES

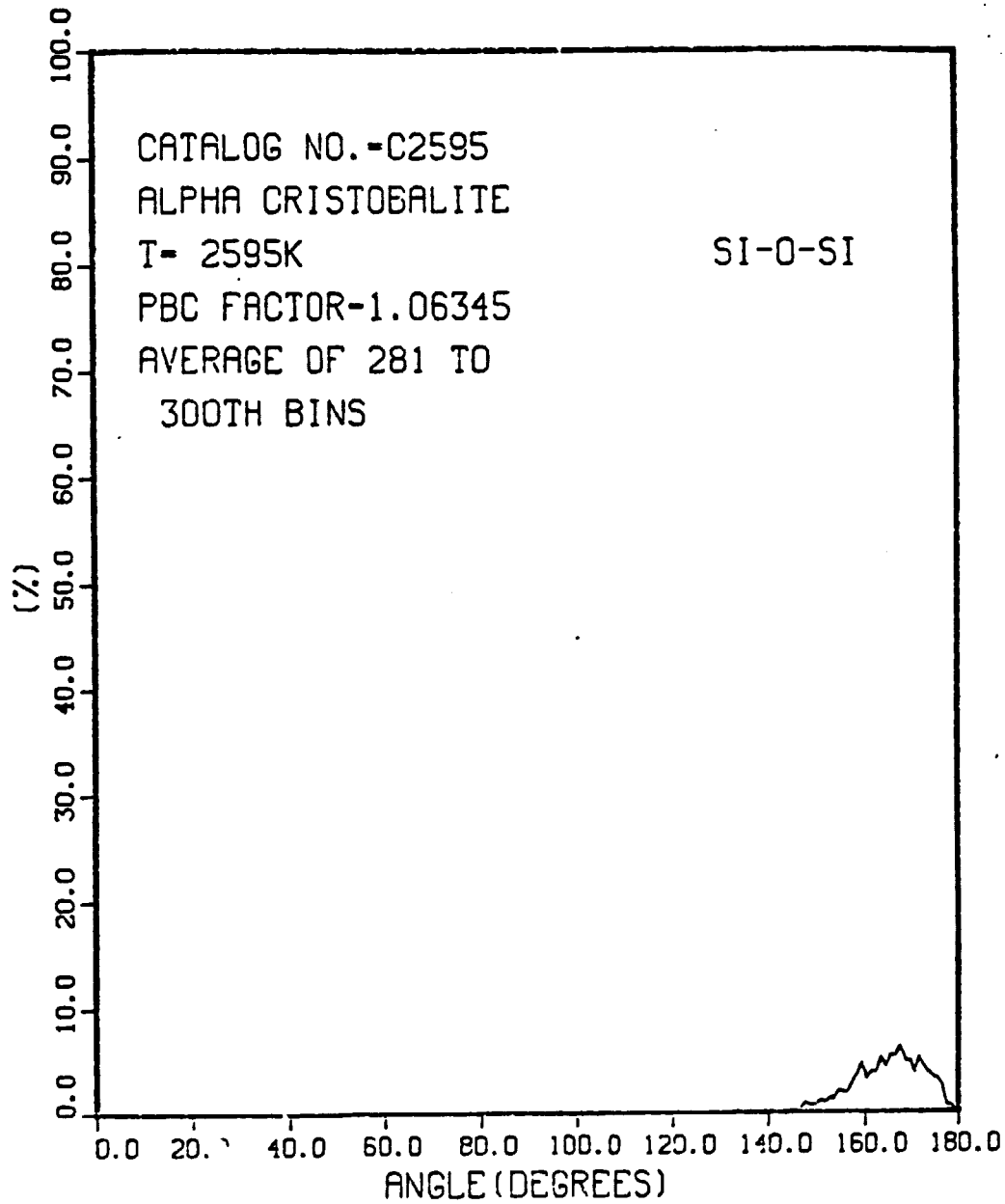

Fig. 15b

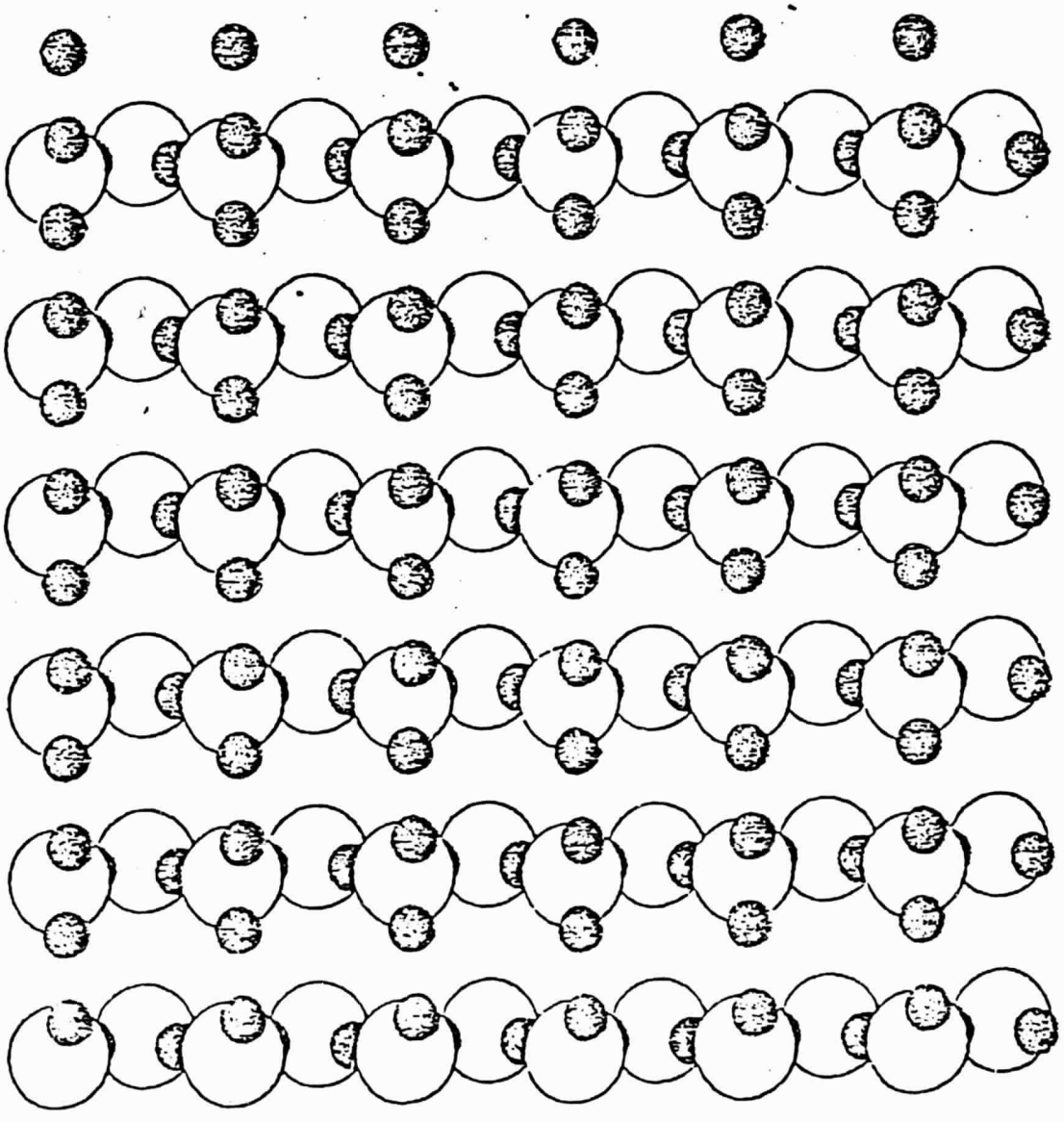

Figure
(100) surface of α-cristobalite (before relaxation)

Fig. 16a

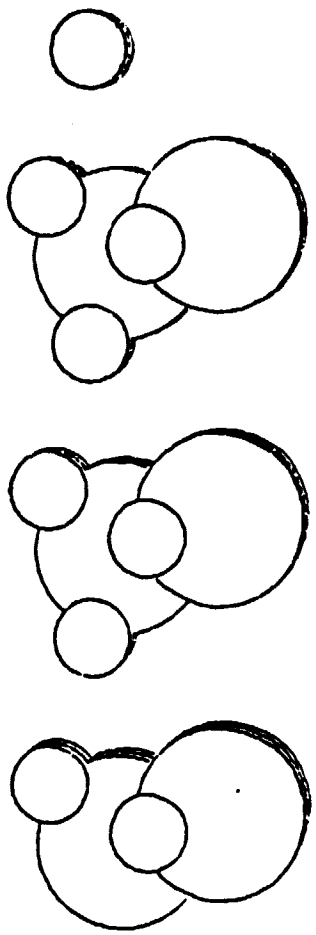

TOTAL NUMBER OF CENTERS=54
α-cristobalite (216)
initial state

Fig. 16b

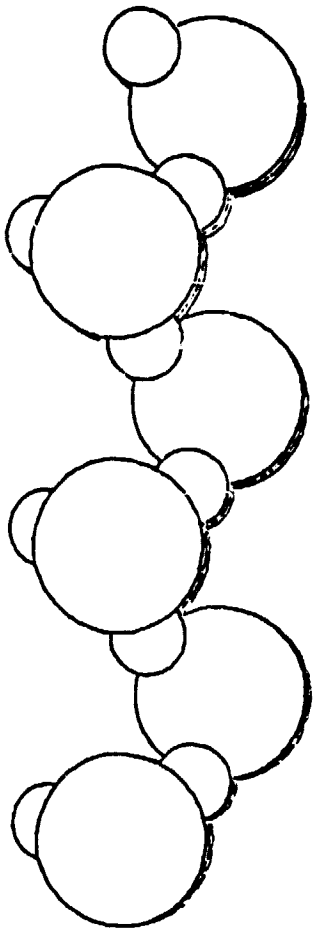

TOTAL NUMBER OF CENTERS-54
α-cristobalite (216)
initial state

Fig. 16c

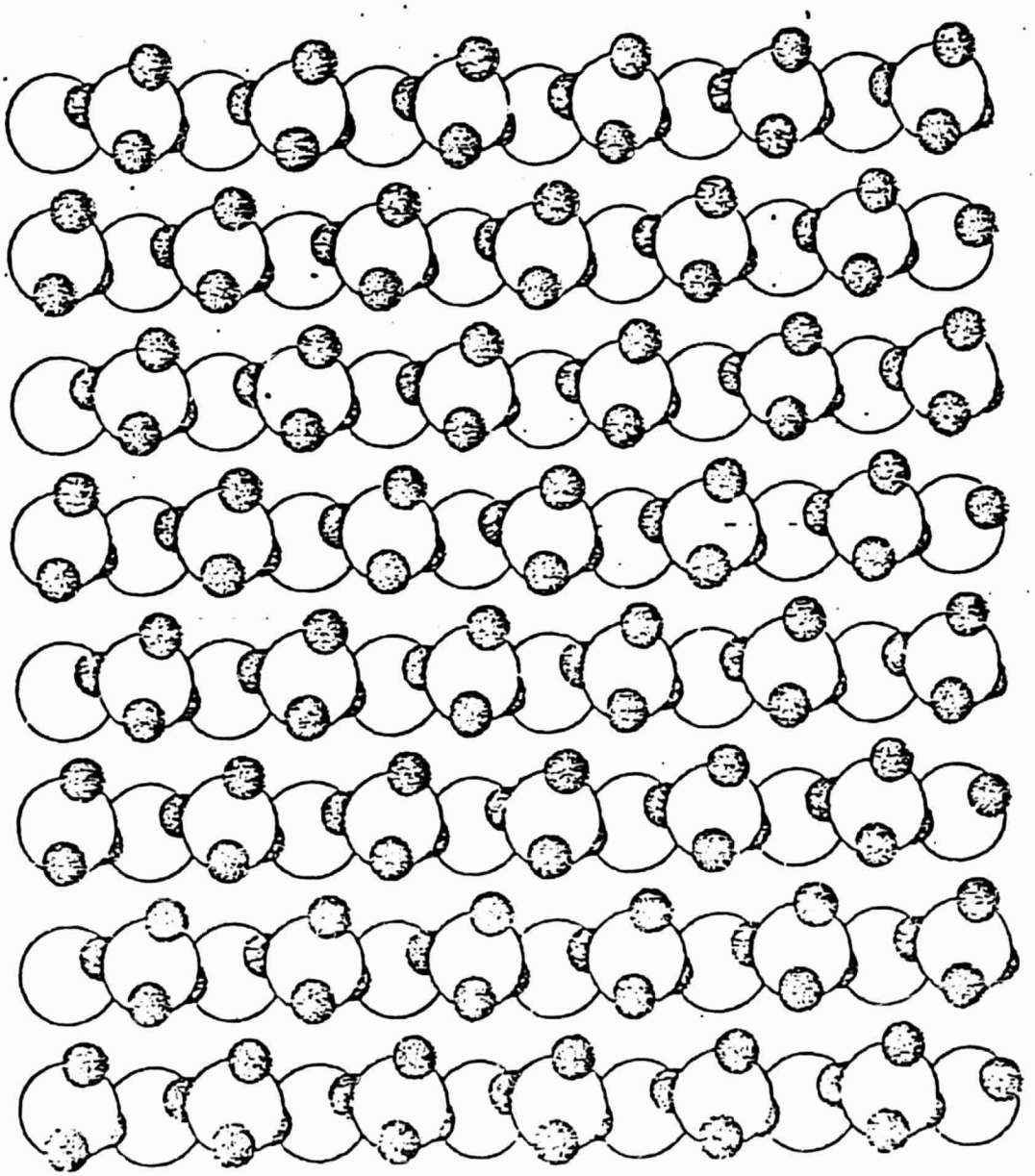

(100) surface, α-quartz (before relaxation)

Fig. 16d

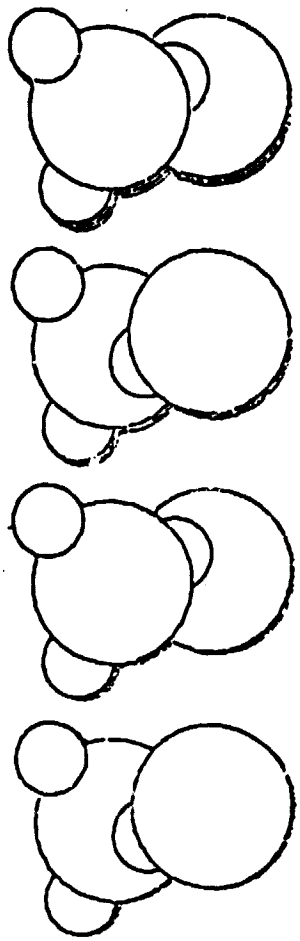

TOTAL NUMBER OF CENTERS=72
α-quartz
initial state
view direction = [100]

Fig. 16 e

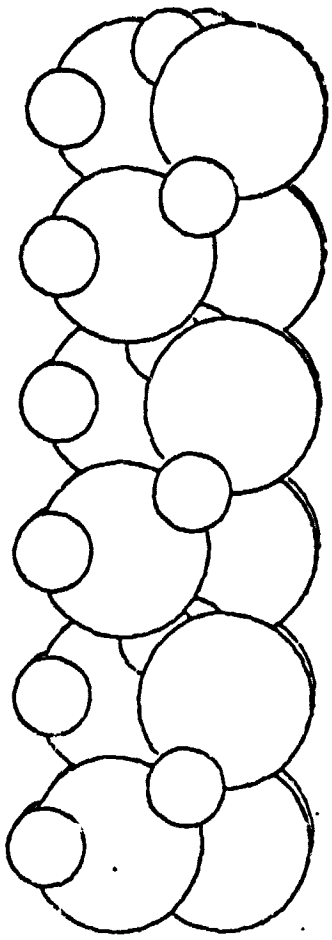

TOTAL NUMBER OF CENTERS-72
α-quartz
initial state
view direction=[010]

Fig. 16 f

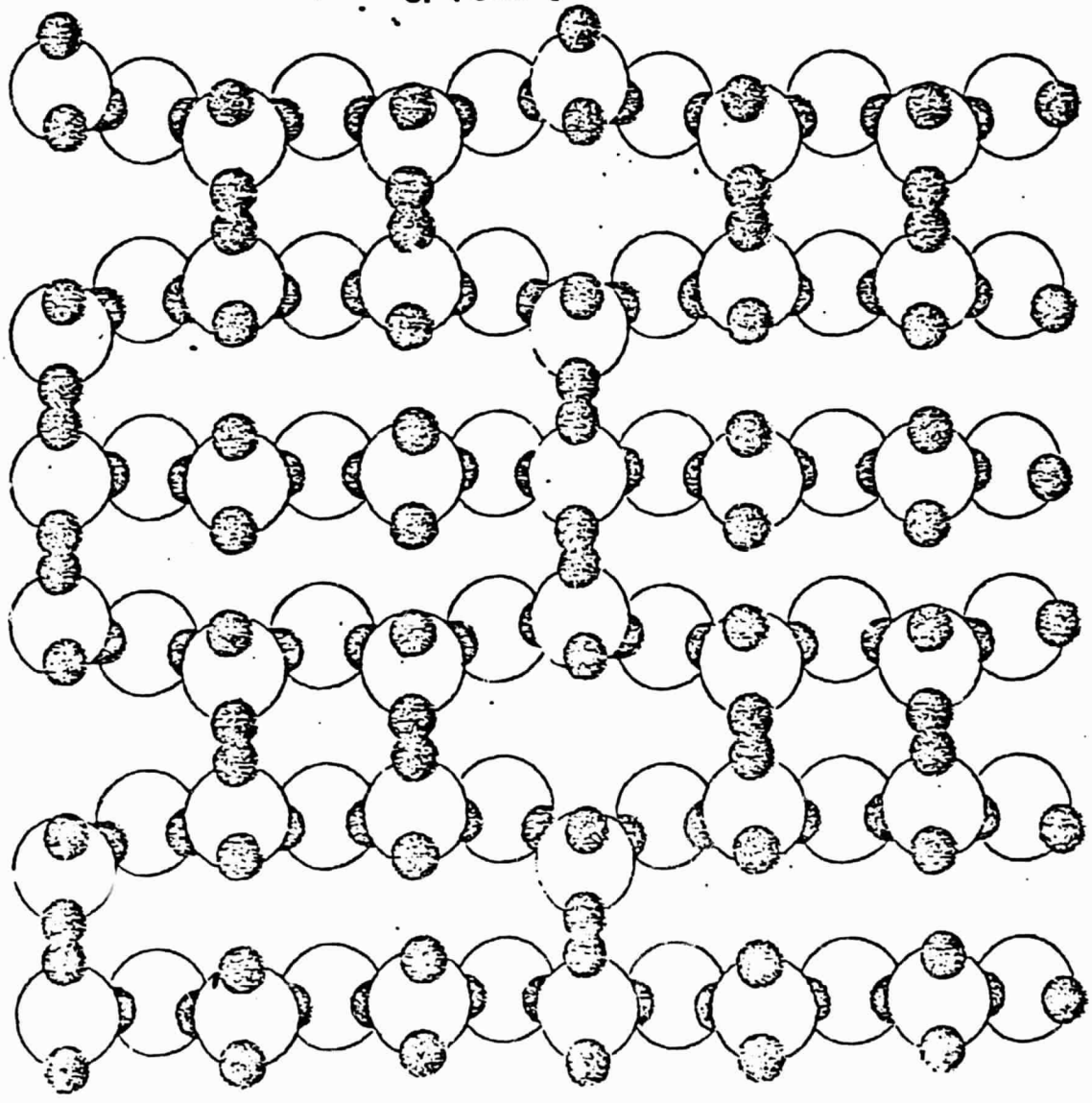

Fig. 2(b)

(100) surface of α-cristobalite (after relaxation)

Fig. 17a

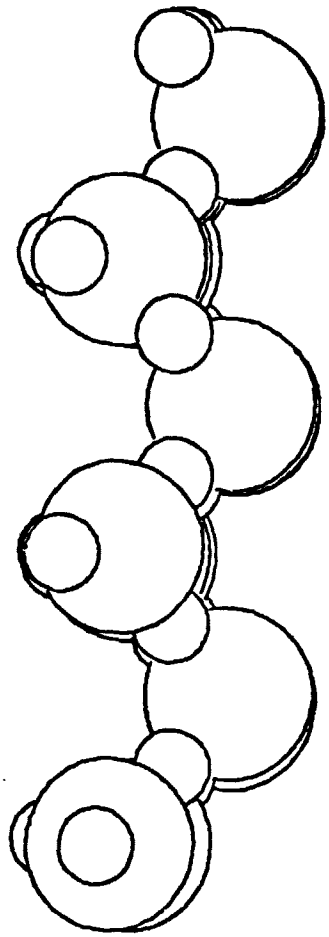

TOTAL NUMBER OF CENTERS-54

VIEW DIRECTION = [100]

TX 111 , CY 1

Fig. 17b

Final

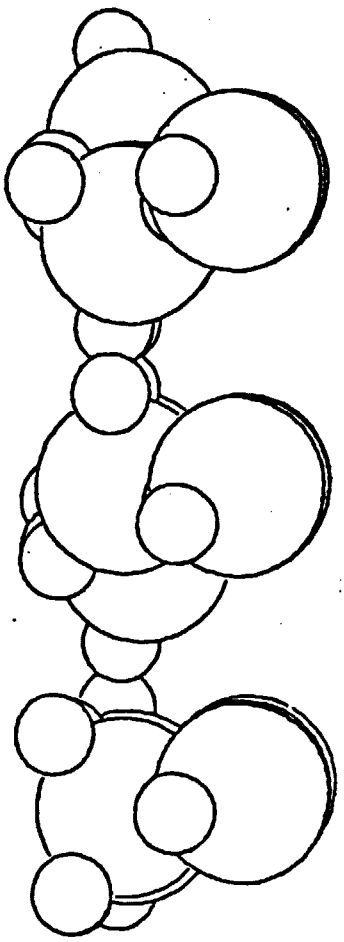

TOTAL NUMBER OF CENTERS=54

VIEW DIRECTION =[010]

TX 111 , CY 1

Fig. 17c

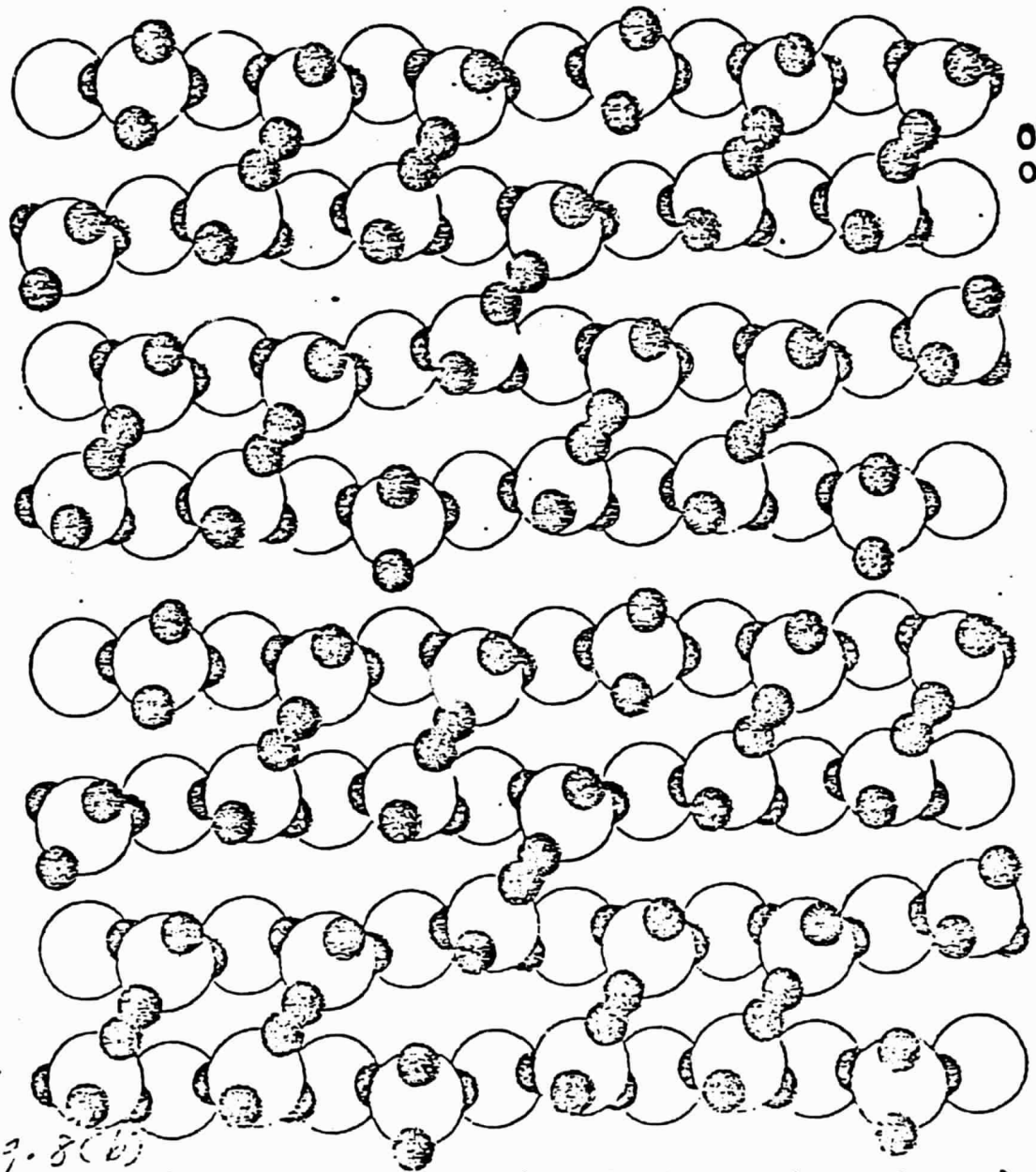

ORIGINAL PAGE IS
OF POOR QUALITY

Fig. 8(b)
(100) surface of α-quartz (after relaxation)

Fig. 17 d

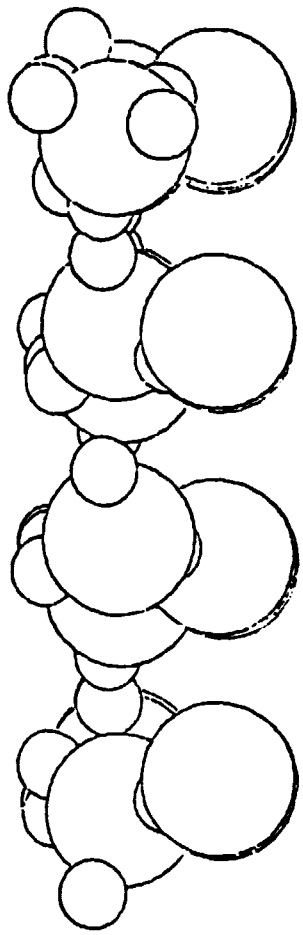

TOTAL NUMBER OF CENTERS=72
α-quartz after relaxation
view direction = [100]

Fig. 17e

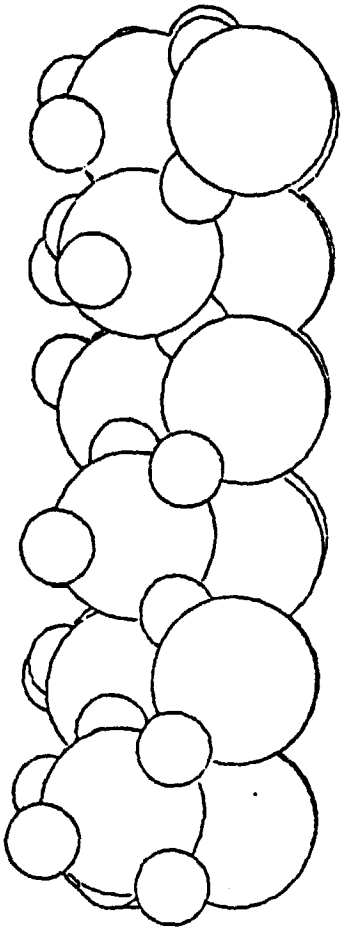

TOTAL NUMBER OF CENTERS=72
α-quartz after relaxation
View direction =[010]

Fig. 17f

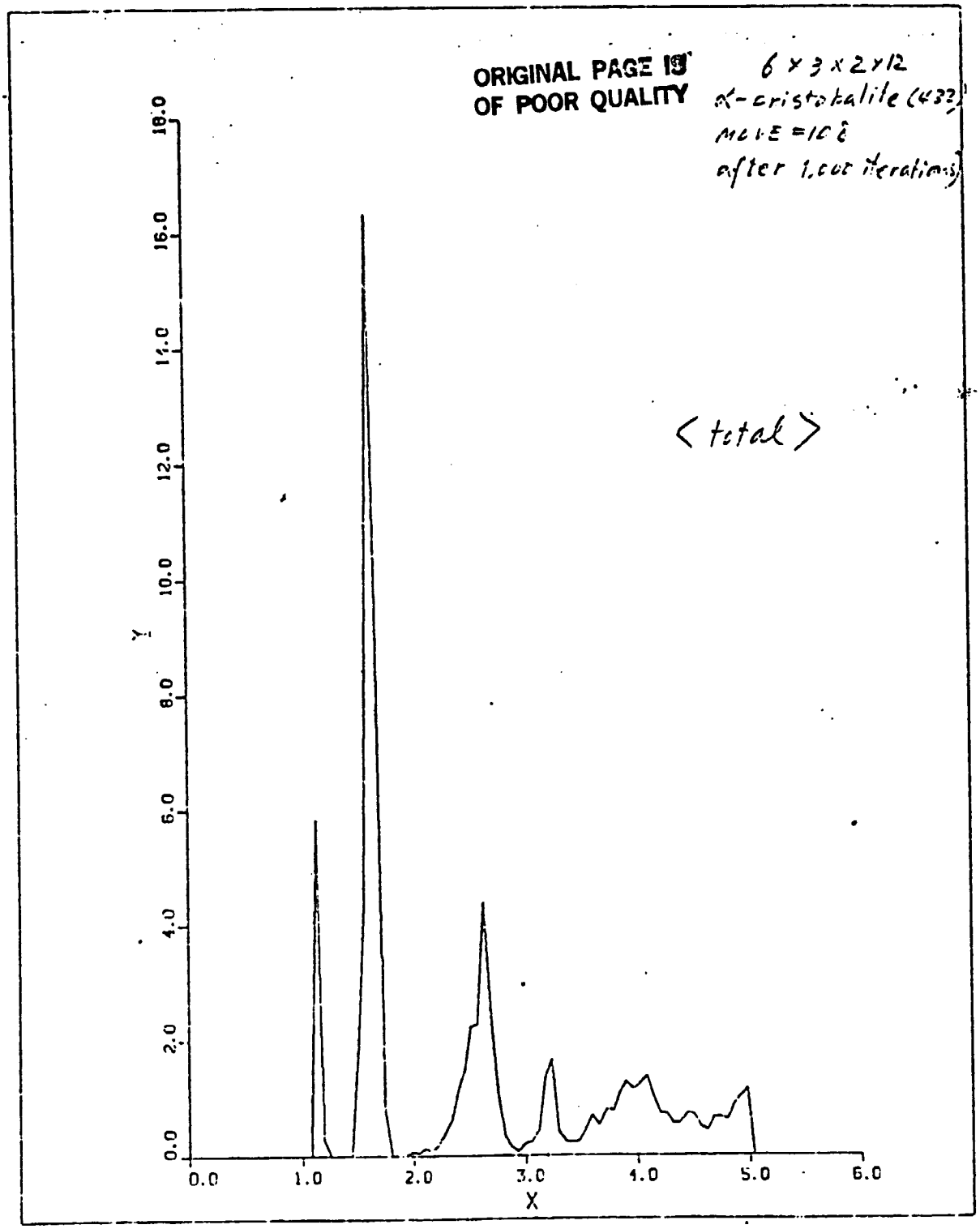

Fig. 18

II. DIFFUSION OF ATOMS AND MICROSTRUCTURES AT SUBSTRATE SURFACES

In many areas related to nucleation, surface reconstruction, surface transport, adsorption and desorption, the detailed mechanism associated with the migration of clusters is highly desired. Several models based on experiments of dimer and trimers motions have been reported [1-3]. Detailed quantitative data for cluster motion on substrate surfaces are limited to W(211) and W(110) surfaces. On these surfaces much of the work on clusters has been concerned with their structural stability [3,4]. Trends in the dependence of cluster structure as well as dimer binding-energy on chemical identity are emerging, but the data are still limited. No computer simulation study has been yet reported for an atomic level analysis of the mechanism associated with the motion of clusters at substrate surfaces.

In this part of the study the diffusion process for dimers (such as Pt_2 and Au_2) on a Pt(110) substrate surface was simulated employing a molecular dynamics technique based on Lennard-Jones type two-body interactions. Because of the stability problems caused by this potential energy function, here, we considered a Pt(110) surface as a substrate whose atomic arrangement is similar to a W(211) surface. Calculations were carried out at $T^*_{Pt} = 0.3$; where, T^*_{Pt} denotes the reduced temperature of Pt. For gold this reduced temperature corresponds to $T^*_{Au} = 0.46$. The reduced time step was taken as $dt^* \leq 0.01$. (in real units the time step is on the order of 10^{-15} second). The reduced lattice constant, a^*, of the substrate was calculated in two ways. (i) Using the density and the thermal expansivity of Pt. These were taken from the literature as $d_{20} = 21.45$ gm/cc and $\alpha_\ell = 8.9 \times 10^{-6}$/deg [5], respectively. The melting point of Pt (2045°K) was also used to scale the temperature of the system to give $T^*_{melting} = 0.7$ which is the case for Lennard-Jones systems. Considering the Lennard-Jones parameters for Pt(ε_{Pt}

= 7910°K and σ_{Pt} = 2.542 Å [6]) we calculated the a^* as 1.5518, at T^* = 0.3. (ii) Using the atomic volumes of rare gas solids, at t^* = 0.3 the reported values for the molar volumes of Ar and Xe are 22.93 and 35.834 cm^3/mole, respectively [7]. Accordingly, the reduced lattice constants were obtained for Ar as 1.5706 and for Xe as 1.5570. These were calculated employing the Lennard-Jones parameters reported in reference [8]. The value of a^* obtained from the Pt data produced a somewhat compressed substrate structure, and the a^* obtained from the Ar data produced a dilation that was monitored by negative and positive virial values during the molecular dynamics run. In the study of a Pt/Pt(110) system even a slight compression of the substrate (i.e., a smaller a^*) was found to have considerable effect on the exchange process. Compression encourages the cross-channel diffusion while a dilation favors channel diffusion. In the rest of this study we employed a^* = 1.559 which is an averaged value for the reduced lattice constant calculated from Pt, Ar and Xe data.

To simulate the substrate, a rectangular slab of atoms was generated with periodic boundary conditions in the x and y directions with the (110) surface normal to the z direction. The dimers (Au_2 and Pt_2) were positioned on the (110) surface. For both cases, the atoms were placed on the adjacent channels to study the dimer motion. For the dynamic calculations only the upper 192 substrate atoms and two adatoms were mobile. The rest of the system; i.e., the lower 192 substrate atoms were kept immobile at their lattice positions. However, these fixed atoms were taken into account in the total energy and force calculations. Velocities of the mobile atoms were initialized with a Maxwellian distribution to the temperature of the run. For equilibration, velocities were rescaled every tenth step for 500 steps. An additional 3000

or more steps were used to observe diffusive behavior of the surface atoms. Figure 1 displays the trajectories for the Au dimer and the top layer of the Pt substrate atoms for 3400 steps. Circles are centered on the final atomic positions. These trajectories indicate that the dimer has been associated on the Pt(110) surface. One of the Au atoms moved two lattice sites apart while the other Au remained localized. In a different run for the Au_2/Pt case, one of the Au atoms formed a split interstitial and a temporary exchange which is similar to the single Au atom diffusion case [9].

Figure 2 displays the trajectories for the Pt dimer along with the top Pt atoms of the substrate. In this case, the motion of the dimer remained quite localized up to 10,000 time steps. Only 0-state or 1-state configurations were observed [1-2]. In another run for Pt_2/Pt(110), considering a slightly smaller a^* (1.5518), it was found that one of the Pt adatoms experienced an exchange with the wall atom (cross-channel diffusion). From this investigation it appears that the exchange process is quite sensitive to the value of a^*. This is an important outcome and has never been investigated before.

Two important factors may contribute to the dissociation of the Au dimer. (i) The reduced temperature, T^*, of Au is higher than the T^* of Pt, and (ii) the Pt-Pt interaction is considerably stronger than the the Au-Au interaction. In this study, no many-body effects were taken into account. However, in the dimer dissociation process, many-body interactions may play an important role. The effect of three-body interactions along with the effect of T^* on the dissociation process of dimers on substrates remain to be investigated.

REFERENCES

1. G.Ehrlich and K. Stolt, Ann. Rev. Phys. Chem. 31, 603 (1980).

2. W.R. Graham and G. Ehrlich, J. Phys. F, 4, L212 (1974).

3. T.T. Tsong, Phys. Rev. B, 6, 417 (1972).

4. D.W. Bassett, Surf. Scie., 53, 74 (1975); and Surf. Scie., 40, 499 (1973).

5. "Handbook of Materials Science," (Ed: C.T. Lynch, CRC Press, 1980) Vol I.

6. T. Halicioglu and G.M. Pound. Phys Stat. Sol. (a) 30, 619 (1975).

7. "Argon, Helium and the Rare Gases" (Ed.: G.A. cook, Interscience Publ., New York, 1961) Vol. I.

8. C. Kittel. "Introduction to Solid State Physics," (Third Edition, 1967) Chapter 3.

9. S.H. Garofalini and T. Halicioglu, Surf. Sci., 104, 199 (1981).

FIGURE CAPTIONS

1. Trajectories for a Au dimer and the top layer of Pt substrate atoms.

2. Trajectories for a Pt dimer and the top layer of Pt substrate atoms.

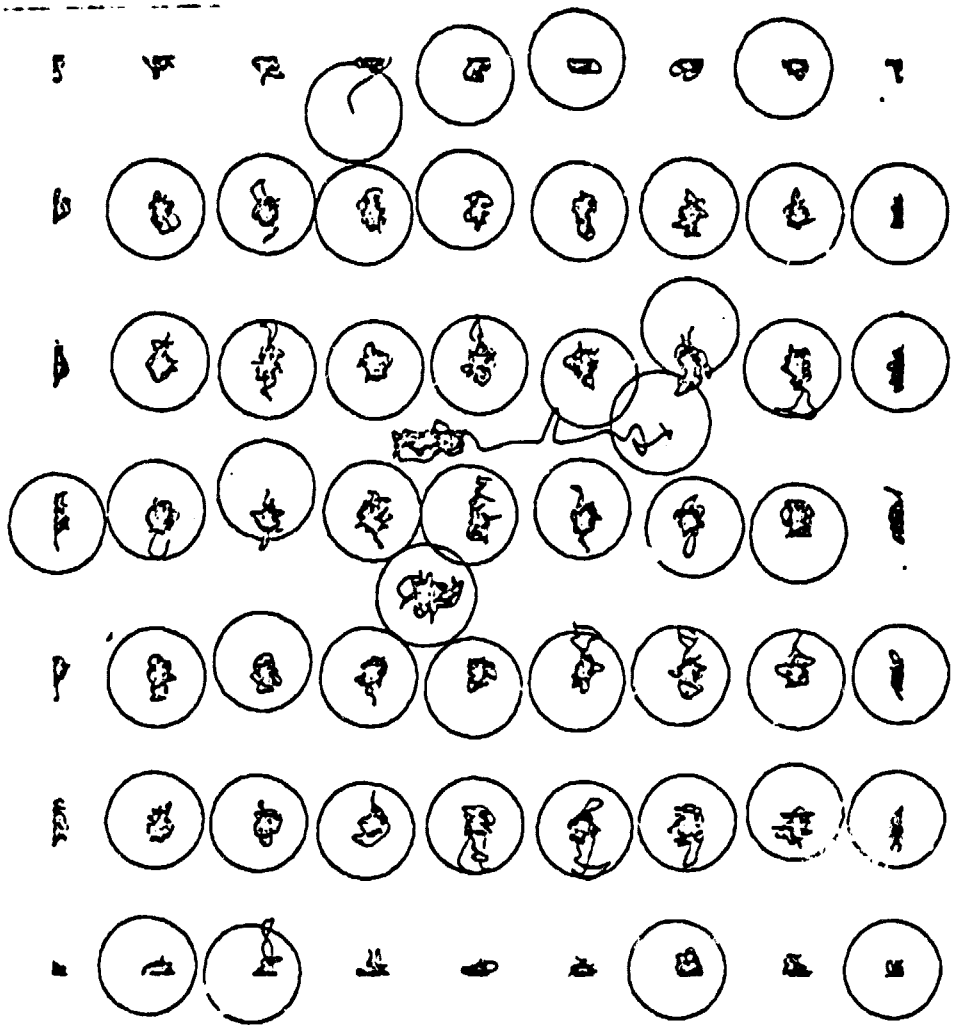

** CALCULATION FOR AU2/PT(110) **

TRAJECTORY PLOT FOR RESULTS CALCULATED ON:

DATE : 09/12/81

TIME : 00.29.23

Fig 1

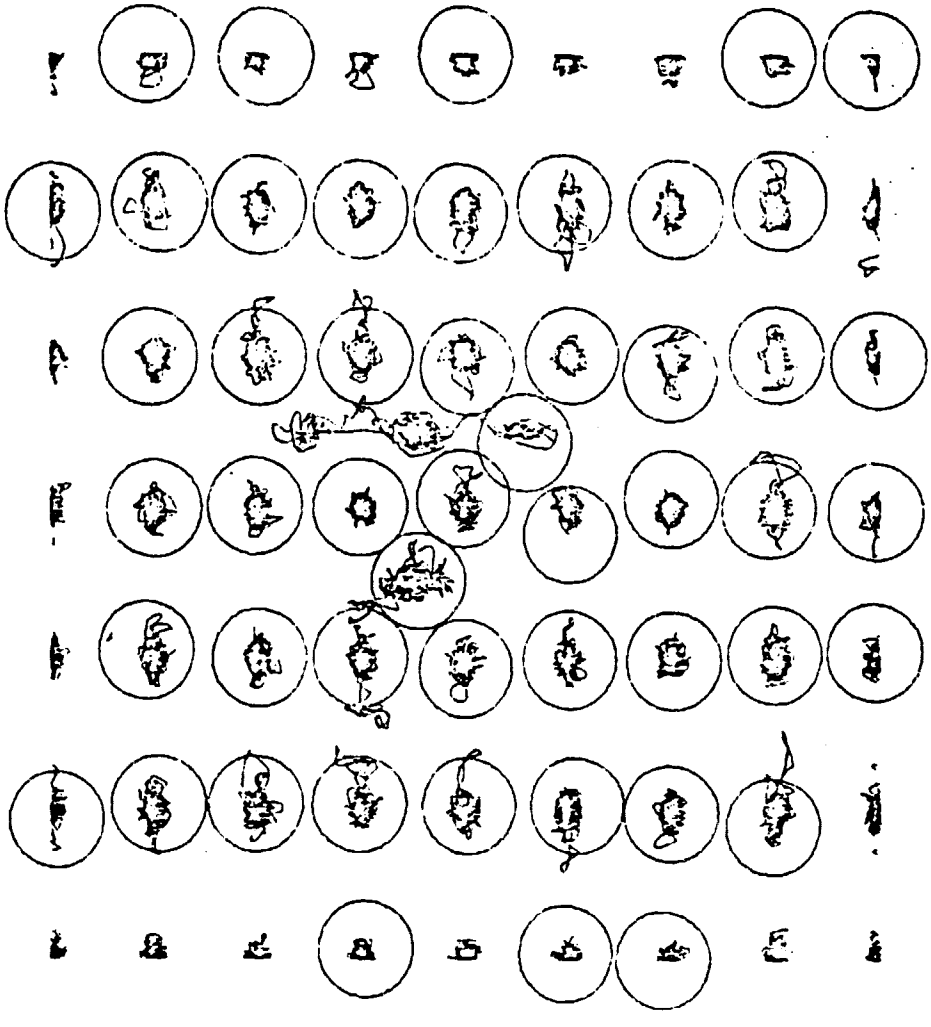

** CALCULATION FOR PT2/PT(110) .. WITH NSBSV-10.. **

TRAJECTORY PLOT FOR RESULTS CALCULATED ON:

DATE : 07/28/82

TIME : 20.43.47

Fig. 2

III. CRACK FORMATION AND PROPAGATION PHENOMENA

A. Introduction:

The mechanical behavior of materials can be specified by macroscopic theories on the basis of a few material constants which provide an accurate description for the responses of materials to forces. However, these theories don't provide a microscopic level of understanding of these basic mechanisms, such as those underlying plastic deformation. In general, the theories for strength of materials, elasticity and plasticity lose much of their power when the structure of a material becomes an important consideration and the material can no longer be considered a homogeneous medium [1].

It is well recognized that the relationship between mechanical behavior and microscopic structure of materials is very important. When mechanical behavior is understood in terms of microscopic processes, it is often possible to improve the mechanical properties of a material. A microscopic description of materials, as opposed to macroscopic theories, cannot be achieved by properly defining a few material constants. Instead, the system must be described in terms of interatomic forces and the coordinates of the particles which constitute the material.

Several studies based on the computer simulation of the mechanical behavior of materials exist. These studies have provided a better understanding of various mechanisms [2,3], such as diffusion, crack propagation, dislocation motion, plastic flow, etc., at the atomistic level.

Material failure is generally caused by fracture which follows yielding or plastic deformation. Slip is the simplest and most common example of plastic flow encountered prior to the ductile frature of materials. In this investigation, the effect of a uniaxial load exerted on a two-dimensional

microscopic slab was analyzed by a computer simulation technique. Even though the discrete nature of the model has limited the size of the sample, the study has produced illuminating results which agree well with the macroscopic theories and provide an atomistic level of understanding of slip and the early stages of crack formation.

B. Computational Model and Procedure

The model consisted of a two-dimensional triangular lattice which contained 400 or more particles. Each particle was treated discretely. The particles were assumed to be interacting via a Lennard-Jones type two-body potential function which is given by:

$$U(r_{ij}) = \varepsilon\left[\left(\frac{r_o}{r_{ij}}\right)^{12} - 2\left(\frac{r_o}{r_{ij}}\right)^{6}\right] \qquad (1)$$

where $U(r_{ij})$ is the pair potential energy between particles i and j separated by r_{ij}. The equilibrium distance is denoted by r_o and ε is the interaction energy at $r_{ij} = r_o$. Many-body interactions were neglected in this investigation. All particle neighbors up to 3.5 r_o were included in the energy force calculations. This procedure insures that all neighbors up to the fifth-nearest neighbor will be included in the calculations. In the calculation procedure, periodic boundary conditions were not employed. This allowed us to examine the surface reconstruction and the formation of edge dislocations during the elongation process.

Initially, the system was generated in a rectangular shape in its equilibrium configuration. Then, the system was elongated in a stepwise fashion by imposing a uniaxial load via small increments. After each

incremental elongation, the system was allowed to fully equilibrate during a relaxation period. All of the mobile particles (defined below) were fully equilibrated after every incremental elongation. A force minimization technique was employed to do this. The force acting on each particle was calculated; then, the particle was moved in the force direction until the resulting force acting on it became virtually zero. This procedure was repeated sequentially for every moving particle up to the complete equilibration state.

The crystal contained two types of particle: (i) Mobile particles: the majority of the particles were treated as mobile particle. These particles were located in the central portion of the lattice as illustrated in Fig. 1. During the elongation procedure, their positions were displaced uniformly in the load direction according to a prescribed incremental elongation. All mobile particles were fully equilibrated during the subsequent relaxation procedure. (ii) Fixed particles: these particles constituted the rigid edges and were held immobile during the relaxation period, i.e., the relative positions of the fixed particles with respect to each other remained unchanged within each particular rigid edge. However, these particles were permitted to interact with the mobile particles, and therefore, contributed to the total energy as well as to the force calculations.

C. Results

1. Two Dimensional Perfect Triangular Lattice

A perfect triangular lattice (i.e., the basal plane of an hcp crystal [4] under a tensile load was studied. The tensile load was applied to three different orientations of the lattice. In the first case, the load was

applied in the $[\bar{1}\bar{1}2]$ directions; in the second case in the $[01\bar{1}]$ direction; and in the third case, the load was imposed in the $[\bar{5}14]$ direction (see Fig. 2). In all three cases, the two dimensional slab, because of the rigid edges, experienced a tensile deformation with a "constraint" [1].

Small incremental elongations* were imposed on the system which resulted in a progressive increase in the total energy until the first slip event occurred when, as shown on Figs. 3(a)-(c), the energy decreased dramatically. Continued elongation of the lattice resulted in additional occurrences of slip. Each slip was accompanied by a rapid decrease in the total energy as shown in Fig. 3(a), for the $[\bar{1}12]$ case. Up to the occurrence of the first slip event, the symmetry of the lattice was well maintained. i.e., only a small amount of lateral contraction was detected at larger elongations. However, no attempt was made to estimate the corresponding Poisson's ratios.

In each case, slip always occurred in the close-packed directions as predicted by macroscopic theories. Since close-packed directions were differently oriented with respect to the tensile axis, slip initiated at different elongations. From the variation of the calculated total potential energy (as a function of elongation), the "average" uniaxial stress and the resolved shear stresses were calculated as described below, and tabulated in Table 1.

---

*The incremental elongation which was used (around the slip formation) corresponded to an imposed fractional strain of 0.001. The magnitude of the incremental elongation had some effect on the results. A test study indicated that results were virtually unchanged for incremental elongations up to $\Delta e = 0.1$. However, larger Δe values caused the system to undergo a sudden brittle-type fracture.

The resolved shear stress, τ_R, along the slip plane was estimated [1] from;

$$\tau_R = \frac{F}{A} \cdot m \qquad (2)$$

where F/A denotes the average uniaxial stress; F is the uniaxial load, and A is the cross-sectional area. The variable m is the Schmid factor and is given by:

$$m = \cos\phi \cdot \cos\lambda \qquad (3)$$

where, ϕ is the angle between the "normal" to the slip plane and the tensile axis and λ is the angle which the slip direction makes with the tensile axis as illustrated in Fig. 4.

The value of F was calculated by numerically differentiating the total potential energy, E, of the system with respect to the elongation:

$$F = \frac{dE}{dL} \qquad (4)$$

where L represents the length. As an example, Fig. 5 demonstrates for the [$\bar{1}$12] case, the stress-strain curve, which is the variation of F/A as a function of $(L-L_o)/L_o$, where L_o is the initial length. In Table 1, the values of F/A were calculated using the values of E and L just before the occurrence of slip. In the present model, A is simply the width of the crystal. Throughout this investigation, the units of F and A were normalized with respect to ϵ and r_o of the Lennard-Jones potential, (i.e. F is given in

units of ϵ/r_o). Table 1 also contains the values for the tensile stresses, σ_T, normal to the slip plane which were calculated as:

$$\sigma_T = \frac{F}{A} \cdot (\cos \phi)^2 . \qquad (5)$$

The values of τ_R, calculated from Eq. (2) and listed in Table 1 for three different load directions are relatively close to each other. Obviously, the magnitude of the stress acting normal to the slip plane has an effect on the process of slip in the present two-dimensional model. For example, for elongations in the close-packed $[\bar{1}12]$ direction, the relatively low resolved shear stress is associated with a higher tensile stress (normal to the slip plane) which tends to separate the neighboring close-packed rows facilitating the slip.

Formation of slip events associated with the elongation process are demonstrated in Figs. 6(a) to 6(e) for strain applied in the close-packed $[\bar{1}\bar{1}2]$ direction, in Figs. 7(a) to 7(e) for the perpendicular $[01\bar{1}]$ direction and in Figs 8(a) to 8(b) for the $[\bar{5}41]$ direction. In all three cases, slip occurred along the most densely packed rows as anticipated from the macroscopic theories. The triangular lattice considered here has three close-packed rows indicated by axes a_1, a_2 and a_3 in Fig. 2.

For strain applied in the $[\bar{1}\bar{1}2]$ direction (i.e., along the a_3 axis) the other two close-packed rows (i.e., a_1 and a_2) form a 60° angle with the tensile axis. Figures 6(a) and 6(b) represent the fully equilibrated system with an average linear strain, e, of 0.0455 and 0.0974 respectively. Figures 6(c) and d demonstrate the initiation and the completion of the first slip

(which is in the $[\bar{1}2\bar{1}]$ direction) after an incremental elongation corresponding to e = 0.0989. Figure 6(c) is not fully equilibrated energy wise, but it shows the initiation of the slip via an edge dislocation type process. Figure 6(e) represents the system with e = 0.1499 after several slip events have occurred. Because of the rigid edges, the system was not permitted to deform freely by uniform glide. Therefore, the slip planes rotated toward the tensile axis. This behavior is consistent with experiments [1]. Results of similar calculations indicated that slip along either a_1 or a_2 occur with the same probability.

For the load applied in the $[01\bar{1}]$ direction, one of the close-packed rows (i.e., the a_1 axis) is perpendicular to the load direction. In this case, the other two close-packed rows, namely, a_2 and a_3 both form 30° angles with the tensile axis. Figure 7(a) shows this system under a tensile load in the $[01\bar{1}]$ direction with e = 0.1270. This was the last elongation-relaxation step for the system before slip occurred. The next incremental elongation (e = 0.1291) caused several concurrent slips to occur and the total energy of the system was lowered about 0.25 ϵ. Figure 7(e) shows the system after it has fully relaxed. Figures 7(b), 7(c) and 7(d) represent intermediate states during the relaxation procedure. They demonstrate clearly the formation and the motion of edge dislocations associated with slip and vacancy formation [1,2]. Figure 7(d) shows a dipole where dislocations have arrested each other. Further elongation caused the system to break in two parts where the vacancy was formed (indicated by an arrow in Fig. 7(e).

In the case of the tensile load applied in the $[\bar{5}41]$ direction, the three close-packed rows, a_1, a_2, and a_3, make 19°, 41° and 79° angles with the tensile axis, respectively. Figure 8(a) demonstrates the system with an

average linear strain of 0.0786 before the slip. Further elongation corresponding to e = 0.810 caused the slip to occur along the a_2 axis that is shown in Fig. 8(b). The results indicate that the probability of occurrence of a slip event increases as the angle formed between the close-packed row and the tensile axis approaches 45°. This is consistent with experimental findings [1].

The results of this study indicate that perfect lattice structures exhibit relatively high resistance to slip and deformation. Because of the two-dimensional character of the model and the neglect of the kinetic energy (i.e., temperature effects), the present results should only be used for qualitative comparisons with experimental data. However, the absolute values of the theoretical results necessary to produce slip are in reasonable agreement with the yield strains obtained from experimental tests on whiskers [6].

In the tensile strength experiments (which are believed to be nearly perfect crystals) a large variety of materials are found to have quite high yield strains [5,6]; in fact, comparable to those obtained in this study. The strongest whiskers are the smallest in size. As the diameter and length is increased, the strength of the whiskers decreases considerably. It is postulated that this decrease in strength is due to defects which are formed accidentally during the growth of the whiskers [5]. In the following section the influence of points defects will be investigated.

2. Two-Dimensional Lattice with Defects

The effect of placing a point defect near one of the surfaces in the two-dimensional model is shown in Fig. 9. As illustrated, the tensile load is applied in the $[\bar{1}\bar{1}2]$ direction. Figure 9(a) shows the model at equilibrium

before the load is applied (e = 0.00). The point defect remains in its original position until the strain reaches approximately 0.066 when, as shown in Fig. 9(b), the defect moves from the interior of the lattice to the surface as expected [7]. The vacancy remains fixed on the surface as the strain is increased until slip occurs at e = 0.077 (Fig. 9(c)). The slip in the [1?1] direction was initiated by the vacancy. Additional simulations in which the defect position was varied while maintaining the distance between the defect and the surface show results similar to those shown in Fig. 9. In each of these tests, the defect remains in its original position until the strain is approximately 0.066 when the defect moves to the surface creating a vacancy there. The vacancy remains on the surface until slip occurs. The onset of slip always occurred at e = 0.077, however, in some of the tests, the slip occurred in the $[2\bar{1}\bar{1}]$ direction. This is to be expected since slip along both directions are equally probable. The strain (e = 0.77) at which slip initially occurred is less than the strain of 0.098 at which the "perfect" crystal showed slip. This reduction in strain, necessary to produce slip, is indicative of the role that defects have in weakening materials.

Figures 10(a) - 10(c) show the results of another simulation in which the point defect is placed near one of the surfaces. The tensile load in this test is applied in the $[01\bar{1}]$ direction. The results are similar to those described above. In this test, the defect moves to the surface when the strain reaches approximately 0.047 (see Figs. 10(a) and 10(b)). This is expected because in this configuration, the particle separation which prevents the defect from being filled is parallel to the tensile direction. Slip, however, does not occur until the strain reaches 0.1107 (Fig. 10(c)). As previously discussed, these results were very repeatable with slip occurring

along both of the equally probable close-packed planes (i.e., [$\bar{1}\bar{1}$2] and [$\bar{1}$2$\bar{1}$] directions).

It is not clear from observing Fig. 10(c) that the vacancy initiated the slip. However, Figs. 11(a)-11(d), which represent intermediate states during the relaxation procedure, show how the vacancy is related to the occurrence of slip. The slip which occurs in the [$\bar{1}$2$\bar{1}$] direction is triggered by the vacancy and progresses via a dislocation motion which is clearly visible in Figs. 11(a)-(d). Near completion of the slip process (Fig. 11(d)) however, the slip direction changes to [$\bar{1}\bar{1}$2]. The completed slip process is shown in Fig. 10(c).

Figures 12(a)-(c) show the results of a test to determine the effect of placing the point defect deeper in the lattice. Figure 12(a) represents the model with e = 0.0. In contrast to the results in which the defect is placed near the surface, the vacancy does not move to the surface as the load is applied. Instead, the defect remains at its original position until slip occurs (Fig. 12(c)). In the tests performed, slip always occurred along a plane adjacent to that containing the void. An intermediate state (Fig. 12(b)) shows that the defect moves as the slip process takes place. Slip was detected at a strain of 0.077 which is identical to that observed when the defect was initially placed closer to the surface.

D. Conclusions:

The discrete model used in this investigation produced results that are consistent with those from macroscopic theory [1]. The results described herein indicate that slip events, which are known to be the simplest type of plastic deformation in crystalline bodies, occur predominantly on rows with

higher density atoms (i.e. along the close-packed rows). In addition the calculations for perfect 2-dimensional triangular crystals with uniaxial loads imposed in the $[00\bar{1}]$, $[\bar{1}\bar{1}2]$, and $[\bar{5}14]$ directions showed that the rule of maximum resolved shear was observed [1]. These simulation results also clearly illustrate the involvement of dislocations in the slip formation process as anticipated from macroscopic theories.

The results of tests to determine the impact of varying the incremental elongation ratio showed that the general characteristics of ductile-type slip formation are not affected by the magnitude of small incremental elongations corresponding to fractional strains smaller than 0.01. However, larger increments in elongation cause the material to undergo a sudden brittle-type fracture. These tests also showed that, as the single crystal deforms under the uniaxial tension, the slip planes tend to rotate toward the tensile axis. This is due to the rigid edges which force the grips to remain in line.

In all cases studied, the systems with point defects experienced slip formation at smaller strains than the corresponding perfect crystals. Vacancies located near the surface move to the surface before the slip occurred. However, vacancies in the interior regions move to the surface only during the slip process.

The present investigation based on energy minimization has limited applicability. It is used here chiefly to test the model, however, the results were quite illuminating in providing atomistic level understanding of various phenomena related to plastic flow. Furthermore, caution should also be used in interpreting these results due to the two-dimensional character of the model. Further studies are in progress, in these laboratories, on 3D systems and employing a molecular dynamics technique to analyze the

analyze the temperature and time dependent behaviors of the various processes which are closely related to slip as well as crack initiation phenomena.

TABLE 1

	Uniaxial Load Direction		
	$[\bar{1}\bar{1}2]$	$[01\bar{1}]$	$[\bar{5}41]$
Angle between the slip plane and the load direction, λ (in degrees)	60	30	41
Total number of particles in the system	400	414	420
Number of moving particles	320	324	340
Incremental elongation imposed during the slip formation (percent)	0.1%	0.1%	0.1%
Initial cross section, A, (in units of r_o) Because of the two-dimensional nature of the model A represents the width	7.8	8.5	8.9
Total linear strain at the first slip event (dimensionless)	0.098	0.128	0.080
Uniaxial averaged stress before the first slip, F/A (in units of ϵ/r_o^2)	0.354	0.457	0.336
Critical resolved shear stress, τ_A (in units of ϵ/r_o^2)	0.153	0.198	0.166
Tensile stress normal to the slip plane, σ_T (in units of ϵ/r_o^2)	0.265	0.115	0.145

REFERENCES

1. G.E. Dieter, "Mechanical Metallurgy," (McGraw-Hill. 1976).

2. A. Paskkin, A. Gohar and G.J. Jones, "Computer Simulation of Crack Propagation," Phys. Rev. Letters 44, No. 14 (1980).

3. W.G. Hoover, A.J.C. Ladd, and N.E. Hoover," Plastic Dislocation Motion via nonequilibrium Molecular and Continuum Dynamics," in "Interatomic Potentials and Crystalline Defects" edited by Jing K. Lee.

4. "Introduction to Dislocations," D. Hull (Pergamon Press, 1975).

5. S.S. Brenner, J. Appl. Phys. 27, 1484 (1956).

6. S.S. Brenner, "Fiber Composite Materials" (American Soceity for Metals, Ohio, 1964), Chapter 2).

7. F.A. McClintock and A.S. Argon, Mechanical Behavior of Materials (Addison Wesley, Mass. 1966).

FIGURE CAPTIONS

1. Schematic representation of the two-dimensional model

2. Direction indices in a basal plane of an hexagonal crystal (see Ref. 4).

3. Variation in total potential energy as a function of the elongation. The length is given by L/L_o, where L is the length at any elongation and L_o is the initial length. Tensile load applied in (a) $[11\bar{2}]$ direction, (b) $[01\bar{1}]$ direction, and (c) $[\bar{5}41]$ direction.

4. Illustration of the geometry of slip. F and τ_R represent the tensile force and the resolved shear stress, respectively. ϕ is the angle between the "normal" to the slip plane and the tensile axis, and λ is the angle which the slip direction makes with the tensile axis.

5. Stress-strain curve for the $[11\bar{2}]$ case. The points were calculated by numerical differentiation of the energy E with respect to $L-L_o)/L_o$. (Stress is given in units of ε/r_o^2.)

6. Perfect triangular lattice under a uniaxial load in the $[11\bar{2}]$ direction.
   (a) strain = 0.0455; system fully equilibrated.
   (b) strain = 0.0974; system fully equilibrated before the slip.
   (c) strain = 0.0989; system partially equilibrated. Initiation of the slip is clearly visible.
   (d) strain = 0.989; system fully equilibrated.
   (e) strain = 0.1499; system fully equilibrated. This shows the lattice after several slip events have occurred.

7. Perfect triangular lattice under a uniaxial load in the $[01\bar{1}]$ direction.
   (a) strain = 0.1270; system fully equilibrated just prior to the occurrence of slip.

(b), (c), (d) - strain = 0.1291; these partial degrees of equilibration show the progression of the formation of slip via dislocation type motions for three different sequences of the relaxation process.
(e) strain = 0.1291; system fully equilibrated. Further elongation causes the lattice to break. The lattice failed where the vacancy, indicated by an arrow, has formed.

8. Perfect triangular lattice under a uniaxial load in $[\bar{5}41]$ direction.
(a) strain = 0.0786; system fully equilibrated prior to slip.
(b) strain = 0.0810; system fully equilibrated after the first slip event occurred.

9. Triangular lattice with defect (near the surface) under a uniaxial load in the $[11\bar{2}]$ direction.
(a) strain = 0.00; system fully equilibrated.
(b) strain = 0.0644; system fully equilibrated.
(c) strain = 0.0770; system fully equilibrated.

10. Triangular lattice with defect (near the surface) under a uniaxial load in the $[01\bar{1}]$ direction.
(a) strain = 0.00; system fully equilibrated.
(b) strain = 0.0473; system fully equilibrated.
(c) strain = 0.1107; system fully equilibrated.

11. Intermediate steps in the equilibration process of a triangular lattice with a defect (near the surface) under a uniaxial load in the $[01\bar{1}]$ direction. The equilibration process required approximately 300 iteration steps to reach equilibrium (Fig. 10(c)).
(a) Step 163
[b) Step 180
(c) Step 198
(d) Step 218

12. triangular lattice with defect under a uniaxial load in the [$\bar{1}$12] direction.

(a) strain = 0.00; system fully equilibrated.

(b) strain = 0.0770; system partially equilibrated.

(c) strain = 0.0770; system fully equilibrated.

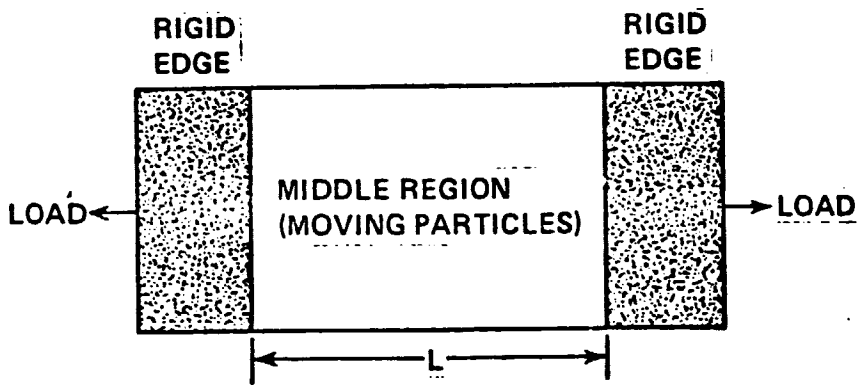

Fig. 1

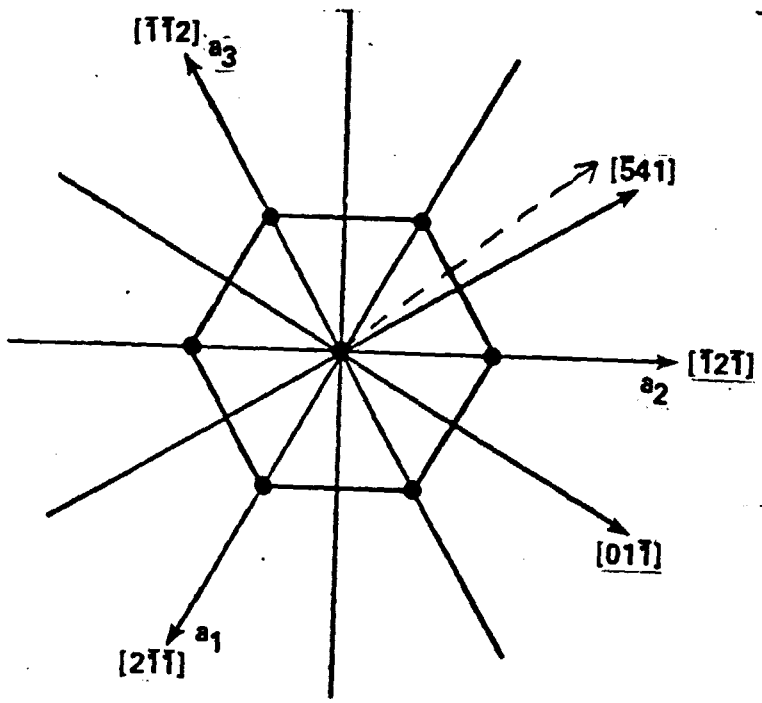

Fig. 2

ENERGY VS. ELONGATION

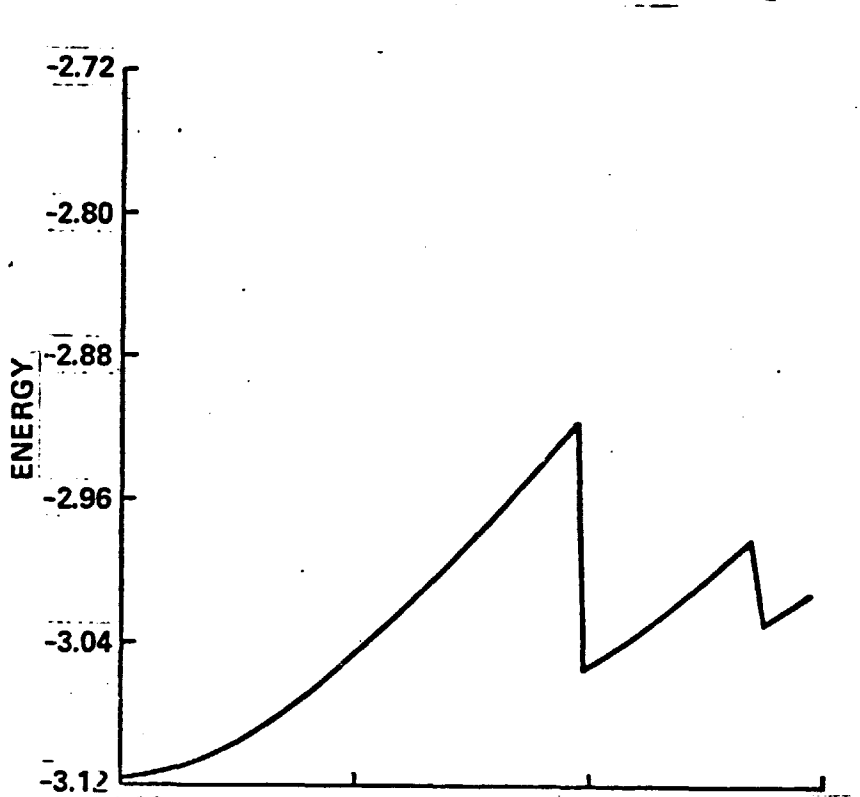

Fig. 3a

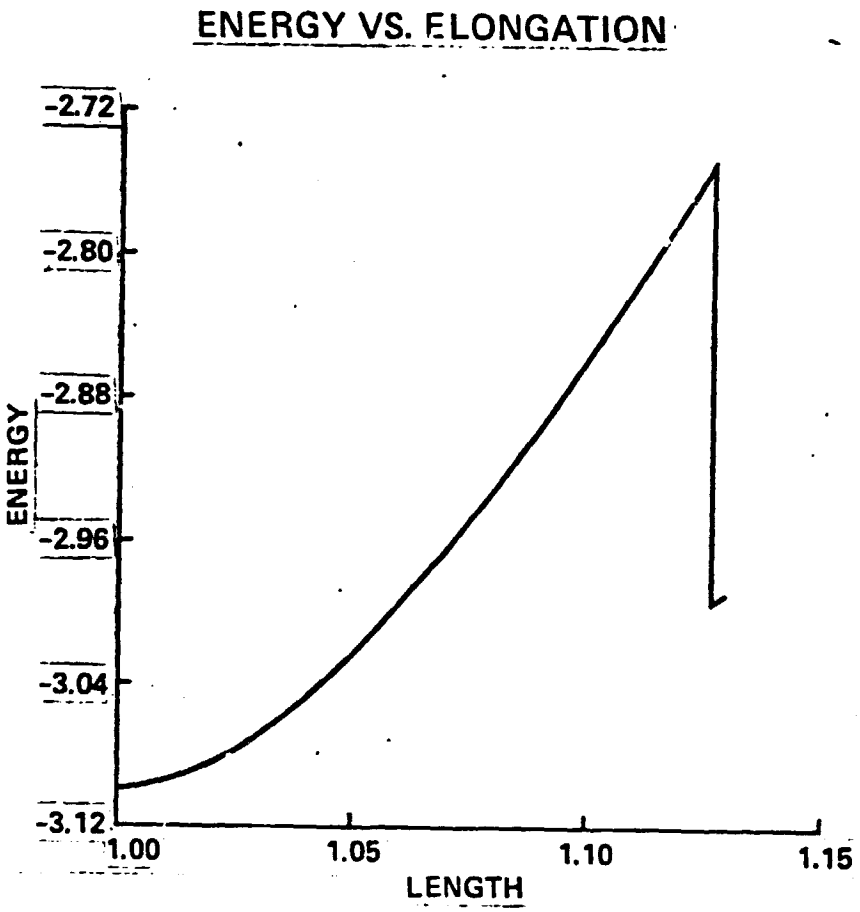

Fig. 36

ENERGY VS. ELONGATION

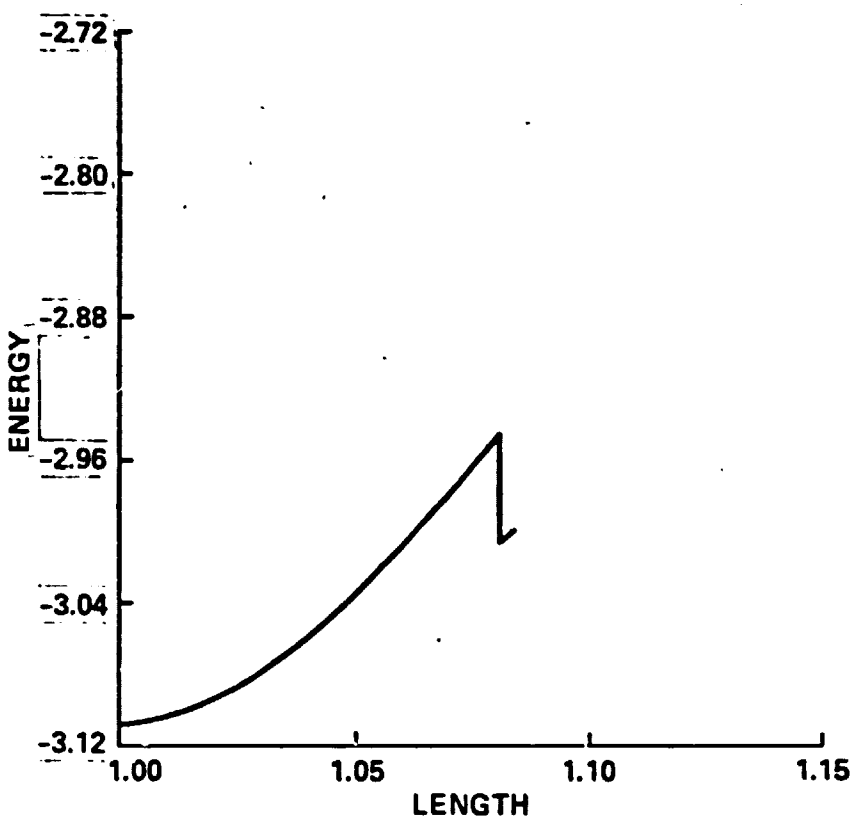

Fig. 3c

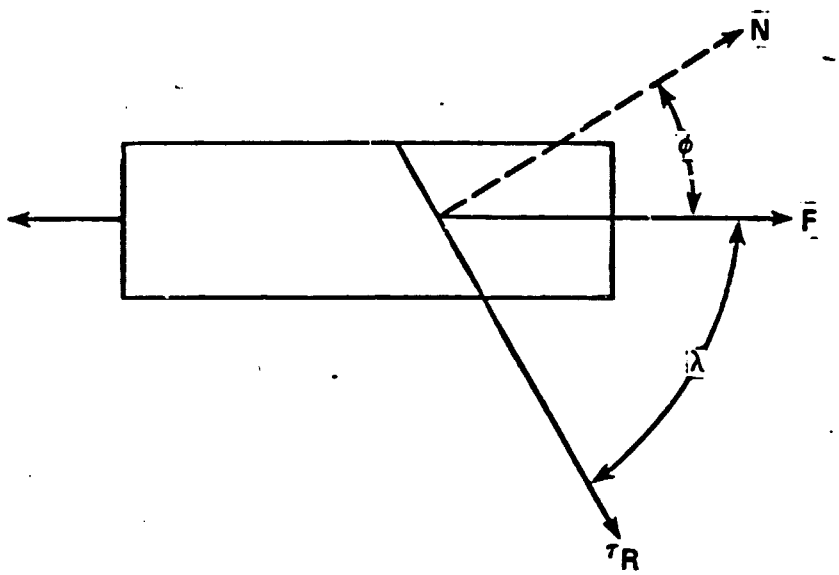

Fig. 4

STRESS VS. STRAIN

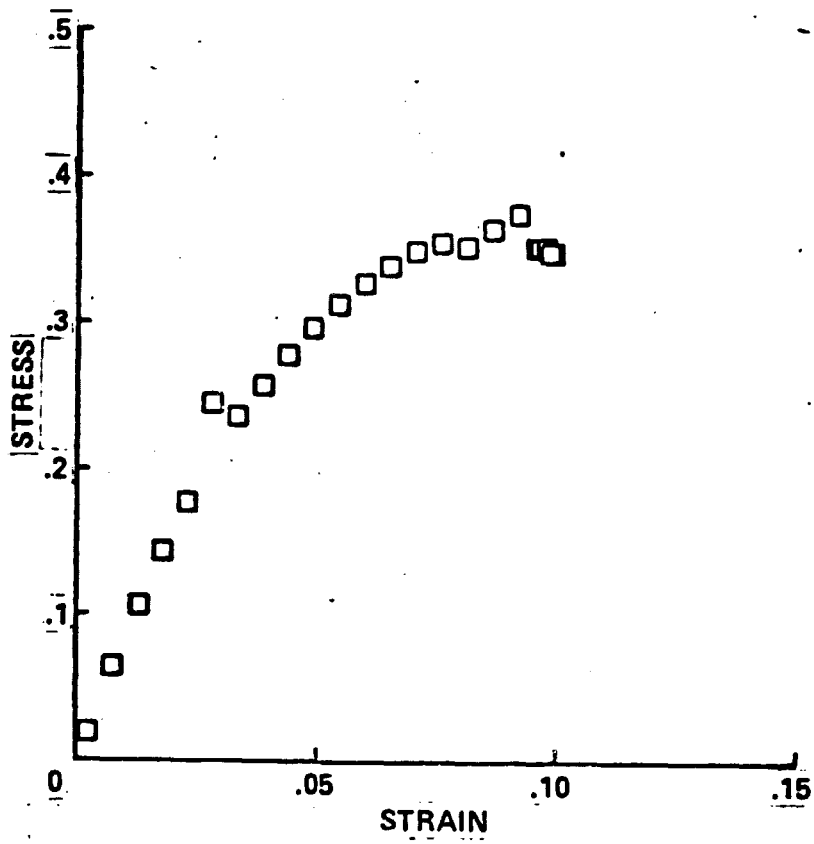

Fig. 5

a

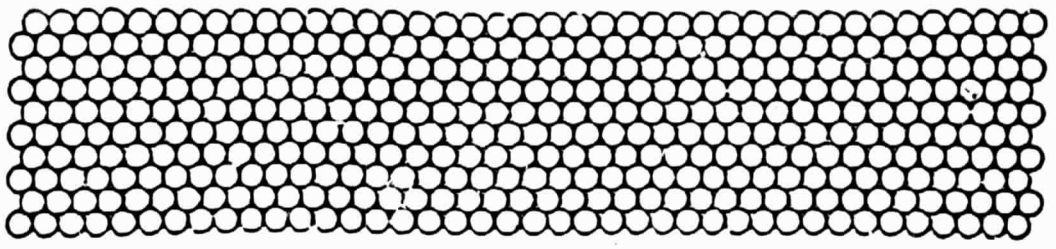

b

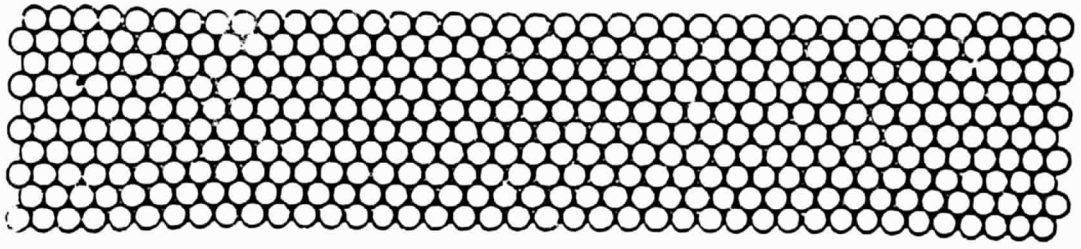

c

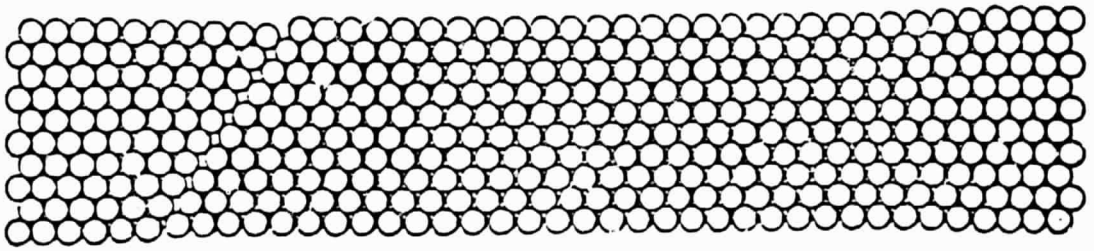

d

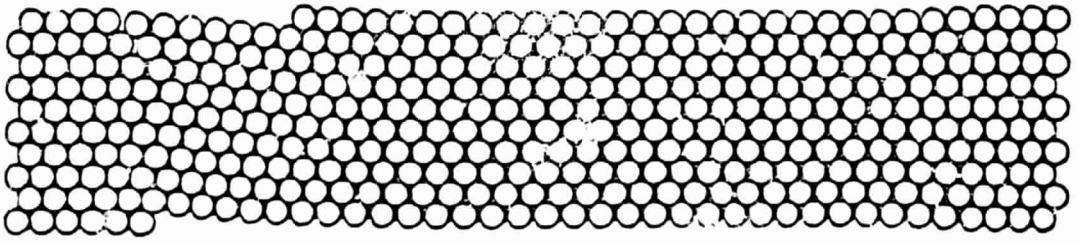

e

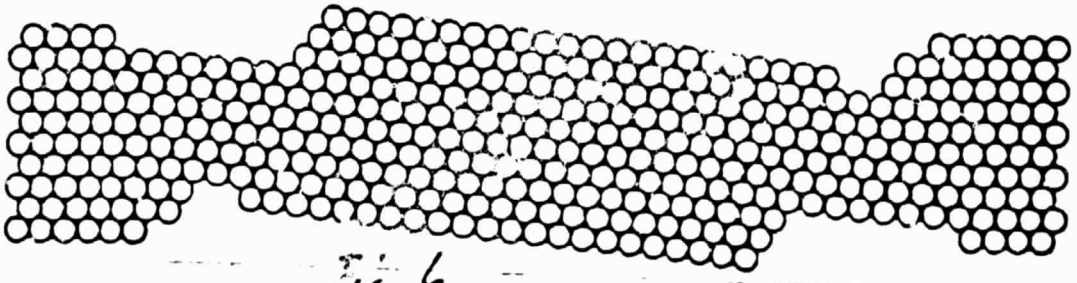

Fig. 6

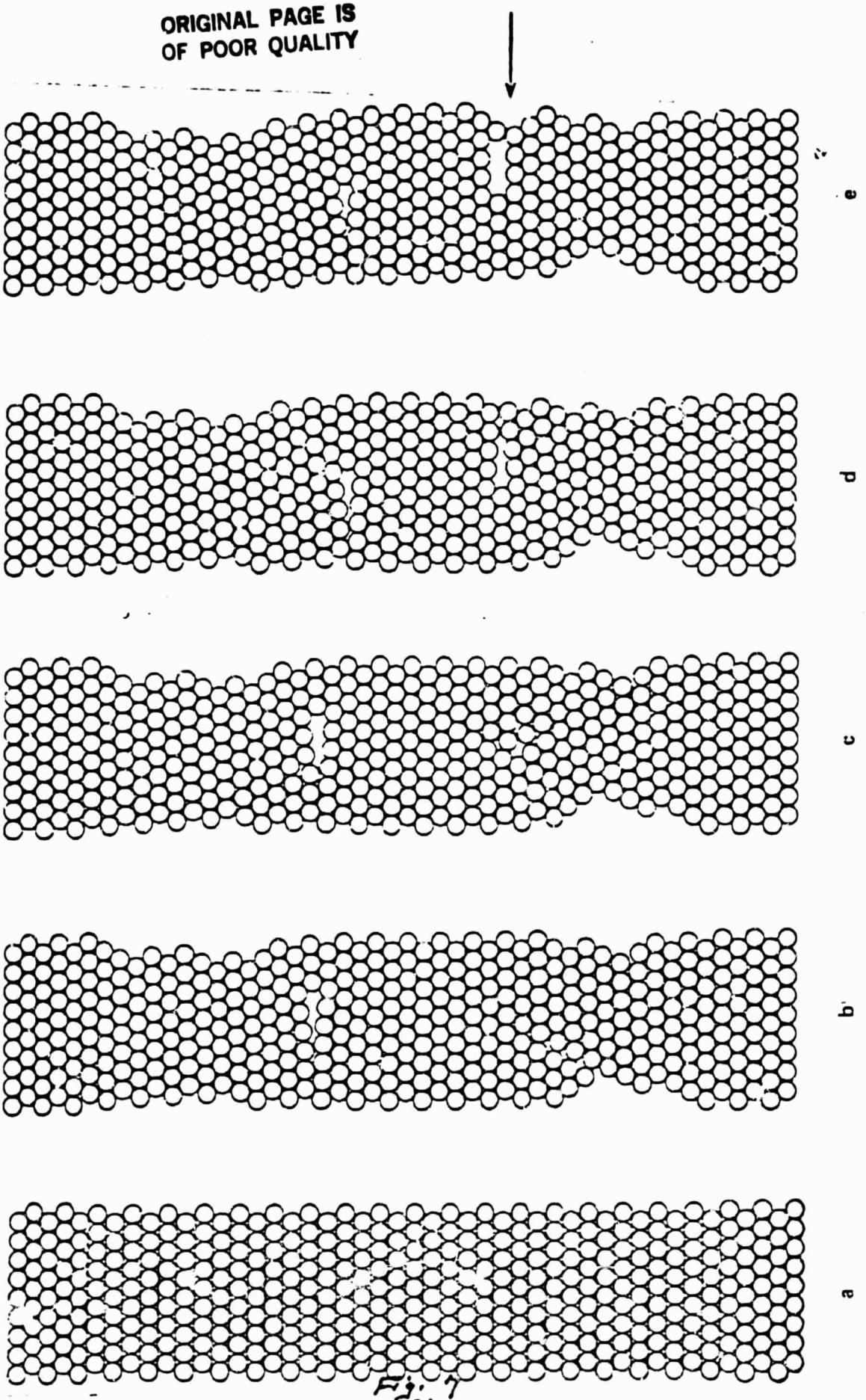

Fig. 7

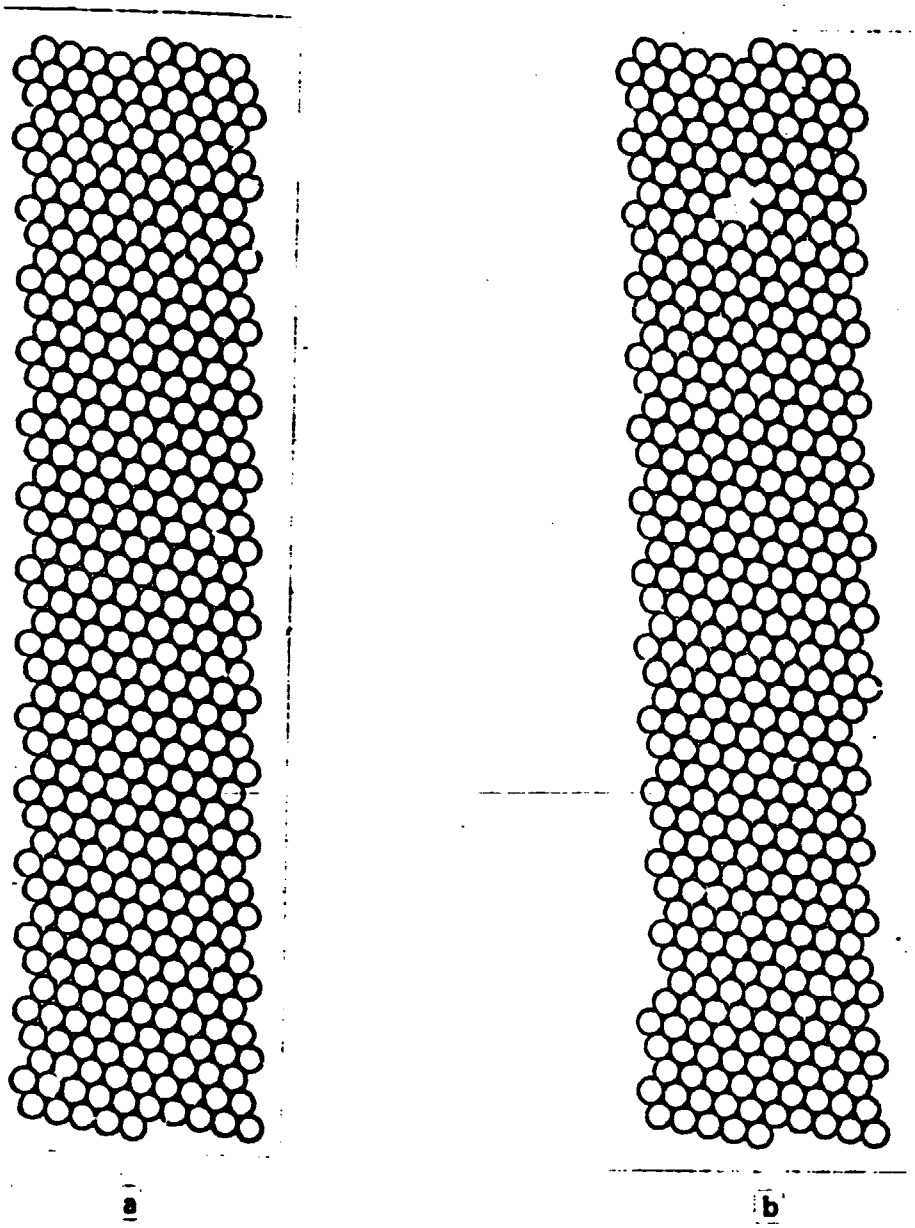

C-2

Fig. 8

ORIGINAL PAGE IS
OF POOR QUALITY

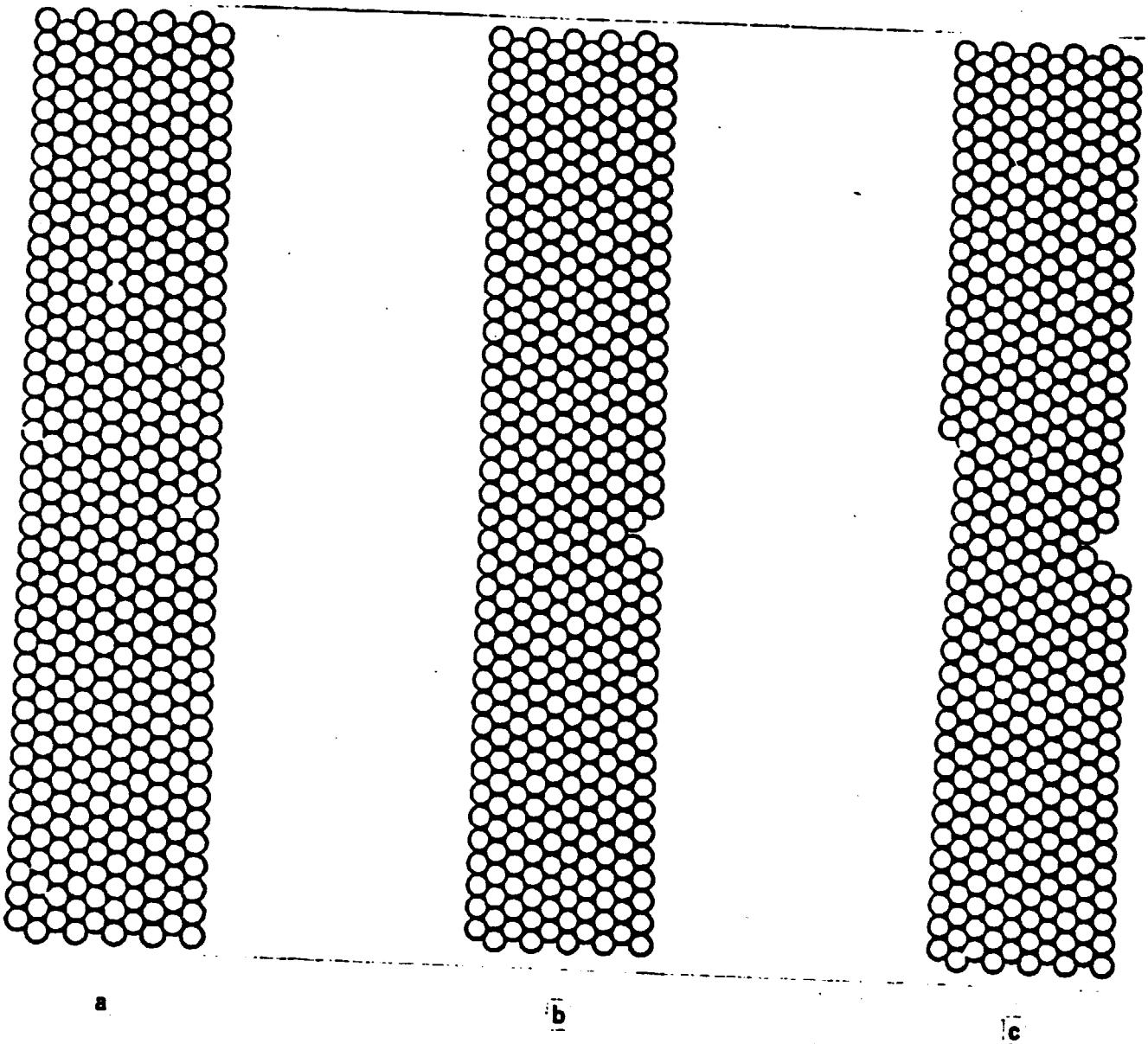

Fig. 9

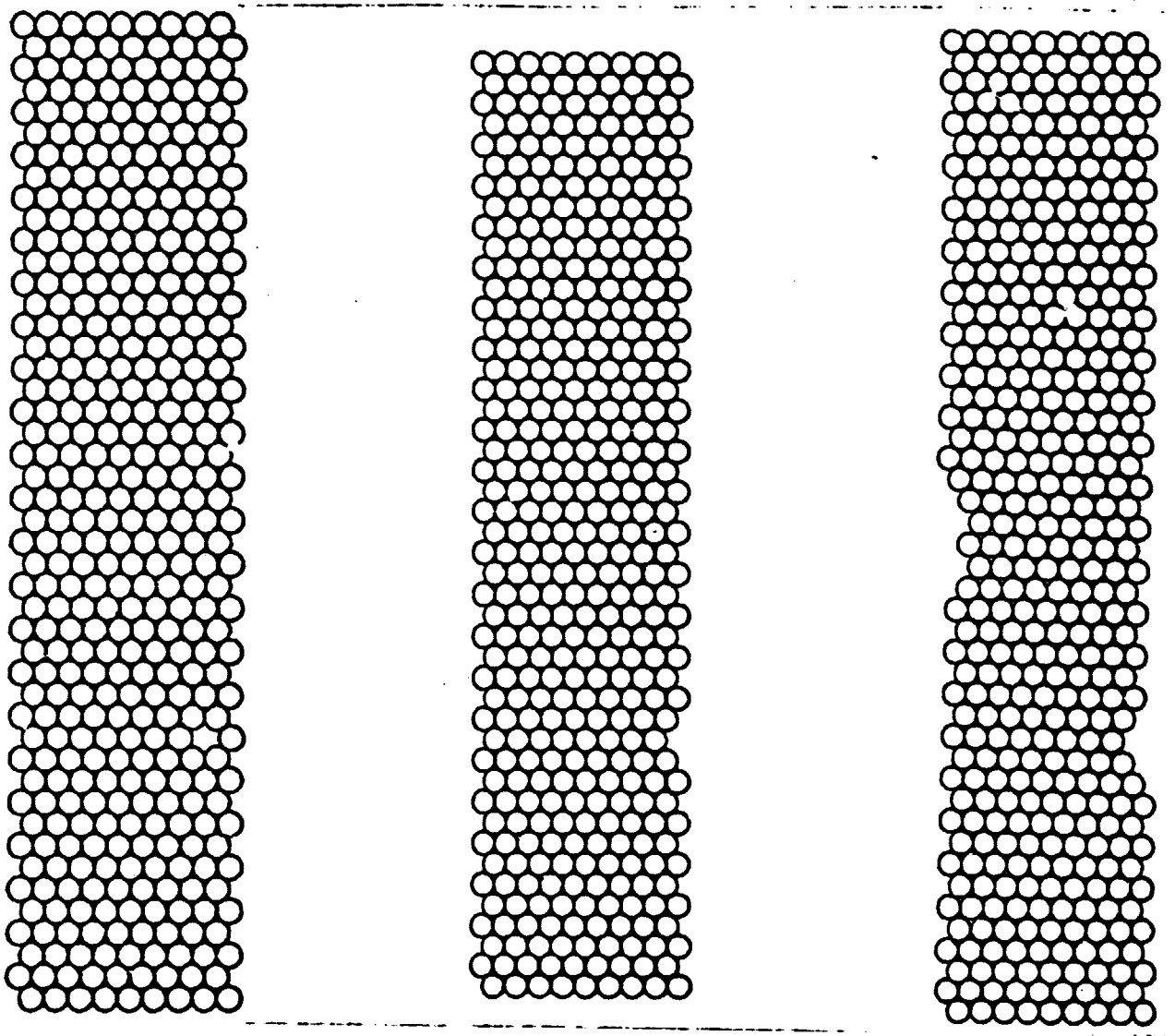

Fig. 10

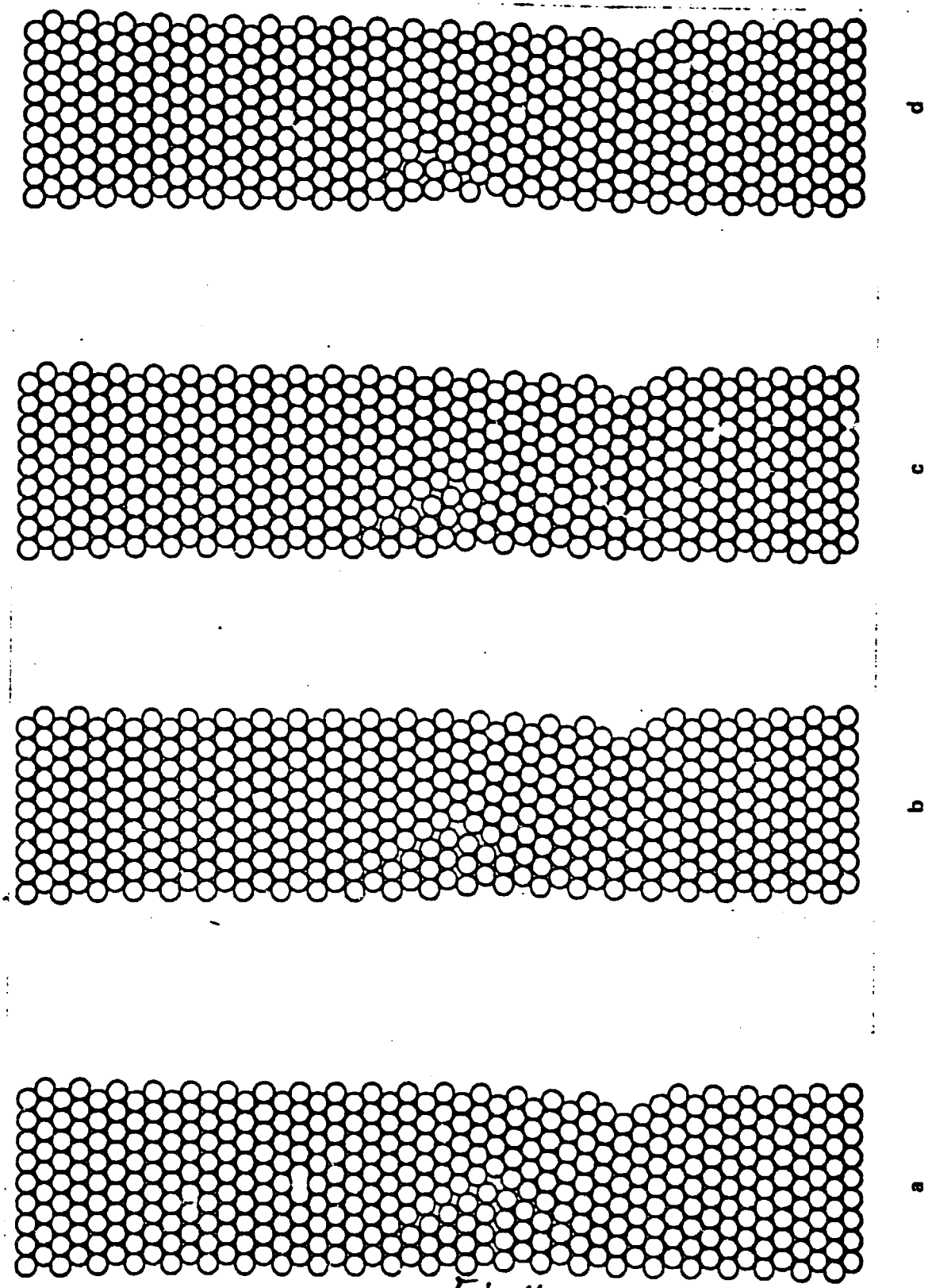

Fig. 11

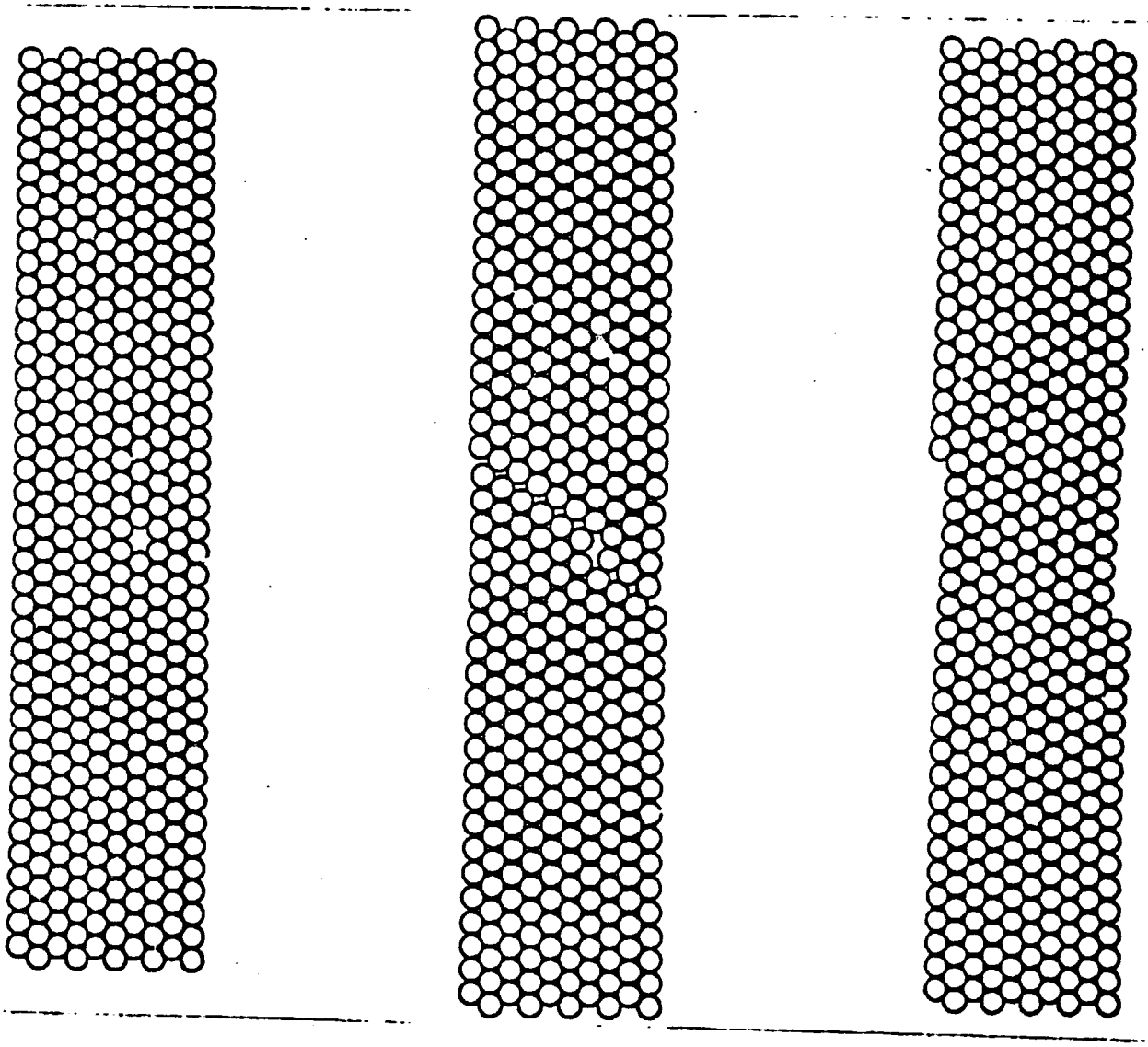

Fig. 12